Computationally Efficient Conical Horn Antenna Design

A theoretical design approach

Tworit Kumar Dash

Technische Universiteit Delft

TU Delft

Computationally Efficient Conical Horn Antenna Design

A theoretical design approach

by

Tworit Kumar Dash

to obtain the degree of Master of Science

at the Delft University of Technology

Student number: 4816315

Project duration: November 11, 2019 – August 27, 2020

Thesis committee:

Prof. DSc. A. Yarovoy,	TU Delft, Professor, Chairman Microwave Sensing, Signals and Systems
dr. ir. B.J. Kooij,	Associate Professor, TU Delft, Microwave Sensing, Signals and Systems
dr. M. Spirito,	Associate Professor, TU Delft, Department of Microelectronics
dr. D. Prinsloo,	ASTRON

TU Delft

Abstract

In this thesis, a computationally efficient model is proposed to determine different performance parameters of a conical horn antenna of arbitrary profile numerically over a wide range of frequencies. The model is developed using mode matching technique that solves the waveguide junction problem and an integral equation technique that solves the waveguide aperture free-space transition. It has functions to evaluate the S parameters, near-fields and far-fields of the antenna. Rigorous testing of the proposed novel technique has been done using MATLAB and the results have been verified by comparing them with the results obtained from commercial tools like FEKO and CST. This technique is capable of finding the performance parameters of the antennas faster than the available solvers in commercial tools like FEKO and CST. Furthermore, various goal functions are proposed for the optimization of some of the performance parameters such as the S parameters, the cross-polarization levels, and the aperture efficiency. These goal functions can be used to find optimum horn antenna feed profiles for radio astronomy applications.

Preface

Tworit Kumar Dash
Delft, July 2020

> "If one is working from the point of view of getting beauty into one's equation, ... one is on a sure line of progress." – Paul A.M. Dirac

I would like to express my sincere gratitude to the people who helped me through the entire thesis period.

Firstly, I would like to thank Prof. Alexander Yarovoy. Thank you for giving me the opportunity to work on a summer research project and as well as this thesis project. Thank you for guiding me as my mentor at every stage of the thesis and addressing all my questions. Thank you for all the fundamental courses on electromagnegtics, radars, antenna systems and UWB. I feel very happy to have you as my mentor.

I would like to thank Dr. David Prinsloo From ASTRON. Thank you for your constant help and support. Thank you for all the encouragement and for believing in me at every stage of the thesis. I thank Prof. Petrie Meyer of Stellenbosch University for all the advice on the mode matching technique. I thank MSc. Yanki Aslan for guiding me towards the last stage of the thesis.

I thank the following Ms3 group members:

Dr. Oleg Krasnov, thank you for the courses on propagation and scattering and radars. Thank you for the summer research project. I enjoyed a lot working with you.

Dr. Faruk Uysal, thank you for the concepts regarding automotive radars and micro-Doppler signatures. I enjoyed the courses a lot.

Dr. Jianping Wang, thank you for all the insights during my fifth quarter at the university, on using tools like FEKO. Thank you for the insights on the signal processing techniques from the course UWB. I still use them in some way or the other.

ing. F. van der Zwan, thank you for helping me with the work station issues. P.J. Aubry, thank you for the insights on MATLAB during several courses in my first year of masters. And the secretary of Ms3, Esther de Klerk, thank you for all the fun activities.

I thank all my friends in Ms3:

Merel Verhoef, ir.Max Schöpe, MSc. Utku Kumbul, MSc. Shengzhi Xu, MSc. Saravanan Nagesh, thank you all for all the discussions and fun activities.

I thank ing. A.P. Frehe:

Thank you for helping with the servers at Ms3 and sorry for all the inconvenience caused due to my rough usage of severs. Thank you for not giving up on me till the end of the thesis.

I thank my friends outside Ms3 group:

Antonios Pelekanidis, thank you for being there always from the beginning of our master studies. Without you, all the courses wouldn't have been that exciting. Ashish Panda, thank you for all the

emotional support and thank you for being my friend for the last eight years. We made it this far. Ashish Dhiman, thank you for all the time we spent together discussing things about courses, food and life. I thank all my housemates (Agney, Soham, Nikhil, Gaurav, Hrishi, Rishi), who are directly or indirectly related to TU Delft, for all the exciting inter-disciplinary discussions and food.

I thank my family:

First of all, I thank my mother Smt. Sasmita Tripathy, without who I wouldn't have been here. She is my first teacher, mentor and life support. Without her sacrifices in the beginning of my career, I wouldn't have become the person I am today. I thank my father Dr. Gobinda Ch. Dash, for all the support and encouragement. I thank my brother Tadit Dash for all the life advice and encouragement. I thank my grand mother, aunties, uncles and all the relatives who directly or indirectly influenced my life. Last, but not the least, I thank my late grand father Ganeshwar Tripathy who inspired me in many ways. As a student of science, I believe, I am here because of the combined effort and encouragement of my family and relatives in many ways.

Contents

List of Figures

List of Tables

1 Introduction

1.1. Research problems and objectives

At present, a global effort is underway within the radio astronomy instrumentation community to realize wideband single-pixel feeds (WBSPFs) for reflector antenna based radio telescopes. Their aim is to achieve high aperture efficiency over frequency bandwidths exceeding three octaves. Currently, there are several different kinds of feeds being developed for the different frequency bands of operation for the ”SKA-mid”. It has five single pixel feeds to cover five different frequency bands (350–1050 MHz (Band 1), 950–1760 MHz (Band 2), 1.65–3.05 GHz (Band 3), 2.8–5.18 GHz (Band 4) and 4.6–13.8 GHz (Band 5)). For the WBSPF, there are two bands of frequencies defined. The lower band (Band A) has the frequencies from 0.35 till 2.6 GHz. The desired upper band (Band B) frequency range approaches an 8:1 bandwidth [24], but that to date desired performance have only been demonstrated for just over a 4:1 bandwidth [36].

However, there has been an increased development of wide band antenna feeds for the radio astronomy application. These feeds operate with 10:1 bandwidth ratio [4]. They are being developed to meet demanding requirements such as stable input impedance, lower losses and good polarimetric properties over the entire bandwidth of operation. Various types of WBSPFs are explained in detail in [4]. Some designs like the QSC (quasi-self-complementary) antennas from Cornell university [8] and the conical-shaped sinuous antenna from the University of Virginia [11] have good match below -9 dB over a decade of bandwidth. From 1.6 Ghz to 14 GHz, the Chalmer’s antenna group have shown that their WBSPF design has matching less than -6 dB and 78 % of the band, it is below -10 dB [35]. The antenna at the Allen Telescope Array achieves an input match of −14 dB over a 20:1 bandwidth (0.5 to 10 GHz) [34]. The design of such antennas are very difficult and for some antennas, designing the feed system at higher frequencies is also a big challenge. These wide band feeds achieve almost 50 % or more aperture efficiency [4]. Till date, no wide band feed has achieved all the challenging requirements from the SKA.

To date, the majority of WBSPF horn antennas are designed by means of numerous parameter sweeps in commercial computational electromagnetic simulation software packages. A process that demands vast amounts of computational time and resources.

Therefore, the main goal of this thesis is to develop a computationally efficient technique to compute the reflection coefficient, radiation patterns and polarimetric properties of the radiated field for a conical horn with arbitrary profile. This computational technique will be used later (the follow up work) to numerically optimize the horn profile to achieve desirable matching and radiation performance over very large frequency band combined with physical compactness of the feed.

To check the validity of the implemented methods, optimization techniques are implemented on top

of the theoretical solver to predict different horn geometries to achieve some requirements. The requirements are based on the applications for radio astronomy and presented by ASTRON (The Netherlands Institute for Radio Astronomy). The output parameters, which are addressed for optimization in this thesis are the return loss inside the conical horn, the cross polar electric far-field level and the aperture efficiency in case of a smooth-walled conical horn-reflector problem.

So far for WBSPF, the bandwidth that is typically achieved is 10:1 [4]. The quad-ridged flared horn (QRFH) is capable of achieving a bandwidth of 6:1 over a large degree of freedom when it comes to beamwidths (35 to 115 degrees). The matching at the aperture is less than -15 dB for lower frequencies and -10 dB for higher frequencies.

The relative cross polarization (XP) generally should be below -15 dB over the HPBW (Half Power beamwidth).

$$XP = 20\log_{10}\left|\left(\frac{E^{xp}}{E^{co}_{max}}\right)\right| \tag{1.1}$$

For WBSPFs the aperture efficiencies achievable were more than 50%. It doesn't go more than that because at higher frequencies, the beamwidth is very narrow and for that the taper efficiency drops and the overall aperture efficiency drops. Therefore, having a stable aperture efficiency over a large bandwidth is very difficult. These basic requirements are taken from the analysis present in [4] and used as optimization goals in the goal functions for smooth-walled horn antennas. The goal functions are based on the hybrid method developed in the thesis (Mode Matching and the aperture-free space transition and analytical far-field expressions). These requirements are first set as goals at one frequency and then, with the optimized horn profile, the goal function values are analyzed over a wide band of frequencies to observe if it is stable. The frequencies which are taken into consideration are the frequencies present in the fundamental mode excitation for the throat waveguide of the conical horn antenna. This is because that is the maximum frequency bandwidth which can be achieved without altering the field patterns on the aperture of the flared horn. This is because as the aperture size in the device increases over the axis of propagation, it excites higher order waveguide modes and because of that the far-field symmetry is affected. However, as the antenna under test should only be excited with the fundamental mode for application purposes, the frequency range for testing can further be expanded (At lest till due to the flare of the horn, another mode with the same azimuthal variation is excited, in this case the mode TE_{12}). As this is a smooth-walled horn, the design and manufacture process isn't that expensive.

The optimization requirements are used from a configuration of an offset Gregorian dual reflector system for SKA 1 baseline design (shown in figure 1.1 and figure 1.2). The main paraboloidal reflector has a diameter about (D_m) 15 [m]. The ellipsoidal sub-reflector diameters (D_s) are 4, 5 or 6 meters. Therefore, the system parameter of focal length to diameter ratio is now an effective focal length to diameter ratio of the dual reflector system. It is generally 0.45, 0.5 or 0.55. The effective focal length to the diameter ratio (f/D) is a measure of the subtended half angle of the feed-reflector system. The subtended half angles for these ratios mentioned above are respectively 58, 53 and 49 degree [4]. In the optimization of the aperture efficiency, the effective ratio of f/D used is 0.5. Effective f/D of a dual reflector system is equivalent to the f/D ratio of a system where the two reflectors are replaced by a single reflector.

1.2. Literature Review and chosen approaches

The problem of horn antenna parameters computation is widely considered in the literature. The following approaches/methods for the horn antenna simulation have been found.

- Finite Element Method (FEM)
- Method of Moments (MoM)

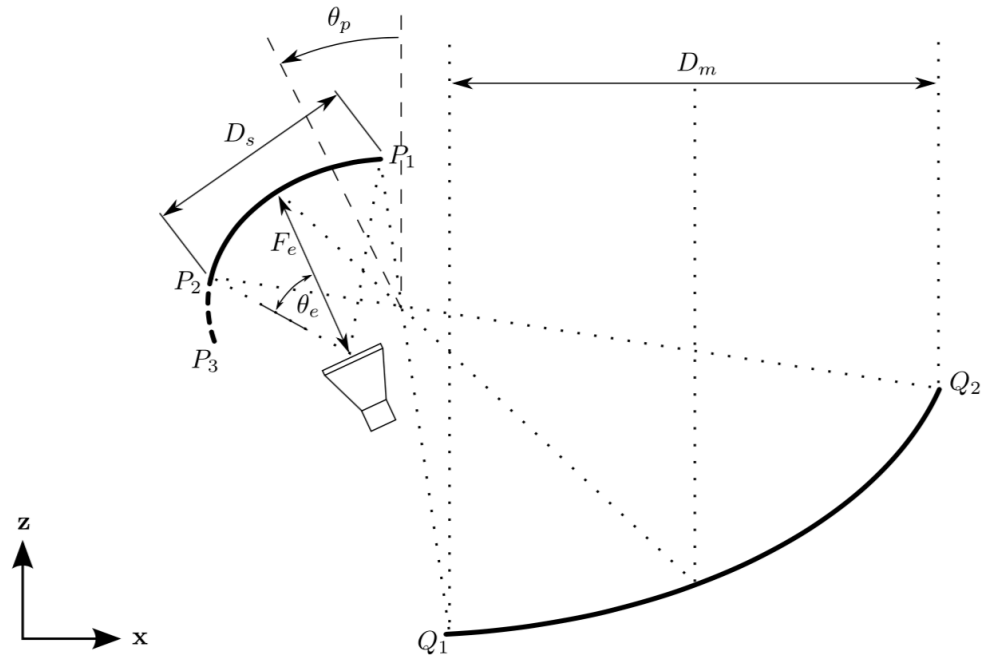

Figure 1.1: Offset Gregorian dual reflector system. Taken from [4]

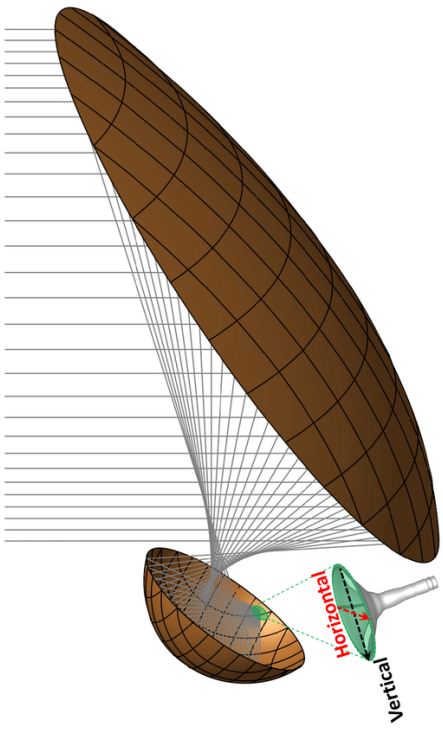

Figure 1.2: Offset Gregorian dual reflector system. Taken from [9]

- Finite Difference Time Domain solver (FDTD)

- Mode Matching theoretical numerical solver

The solvers like FEM, MoM and FDTD full wave simulation techniques are already used in commercial tools like FEKO and CST. These techniques use Maxwell equations to solve an approximate version of the actual antenna by discretizing it into finer mesh. Therefore, these solvers use more computational time and resources to solve different performance parameters of the antenna (especially when the antenna dimensions are electrically large and the output parameters are sensitive to the geometry). From the transmission line point of view, the horn antenna can be considered as a combination of the cascaded waveguide transition and a waveguide to free-space transition. An effective way to compute waveguide transition is mode matching technique, which was widely used previously for waveguide filters and transition analysis. Below the state of the art in the mode matching technique and free-space transition technique are described.

1.2.1. Literature review Mode Matching Technique (MMT) and changes made in MMT for the challenges in the thesis

Mode Matching technique is a very versatile method for waveguide junction problems. It is also used to find the scattering parameters for filters, transformers, couplers, etc. It uses a General Scattering Matrix (GSM) approach to solve waveguide junction problems. If the structure of the complex problem can be divided into a number of waveguide junction problems, the GSM approach can be very accurate. The GSM approach deals with energy conservation laws of classical electromagnetics. Several research papers have been published with MM technique to solve different kinds of problems. For example, a numerical surface integral form for GSM can be found in [13], [21] and [28].

Convergence criteria based on the number of waveguide modes at each side of the junction problem is addressed in papers like [13], [21] and [28]. The convergence criterion suggests that there should be different number of modes included in the analysis of the junction problem based on the aspect ratio between the 2 waveguides before and after the junction. The bigger the dimension of a structure with respect to the wavelength, the more the number of waveguide modes should be included in the analysis. For example, if a waveguide junction problem involves 2 circular waveguides with a radius ratio 2:1, the bigger waveguide should have modes roughly 4 times as that of the smaller waveguide (aspect ratio here is the ratio of areas ($\frac{A_{big}}{A_{small}} = (\frac{r_{big}}{r_{small}})^2 = 4$)). However, for a cascaded structure with elements having a varying range of dimensions, for simplicity of implementation, the same number of modes is used in all waveguides in the problem. This can be found in [28] and [31]. The number of modes is decided by the element having the biggest dimension. With this approach to solve cascaded waveguide problems, unnecessary time and computation resources are used because of the fact that not all the waveguide elements in the problem have all those modes propagating for a particular frequency. Therefore, this project also addresses some convergence criteria based on the aspect ratio as well as the number of propagating modes on each waveguide element. Therefore, by the use of different number of modes on each waveguide section in a cascaded waveguide problem, considerable amount of computation time is saved.

However, the approach mentioned is very general to any waveguide junction problem and therefore the GSM is not simplified for different types of waveguide junction problems. Analytical formulation of the GSM can be found in papers such as [23] and [33]. However, after careful analysis, it is found that some of the expressions are incomplete. Furthermore, in [33], the analytical formulation is done for a rectangular to circular cross section waveguide junction problem. Therefore, the field expressions are changed to a Cartesian coordinate system for the circular cross-section waveguide. As the aim of the thesis is to determine the GSM for a circular to circular cross section waveguide, using that procedure to find the GSM wouldn't be elegant. Therefore, this project also carefully examines the integrals for a circular to circular cross section waveguide junction problem to find elegant solutions for the GSM. This is done by using the properties of Bessel functions and Lommel integrals [2] [5] .

Furthermore, the physics behind the coupling between different modes is also explained in detail with the analytical expressions. it also focuses on differences found between the MM technique and different other solvers used in commercial tools like FEKO/CST.

1.2.2. Literature review of the aperture to free space transition in open waveguides and choice of one of the many techniques for the thesis

Using the two port MM technique to solve various parameters of the conical horn antenna has one limitation when it comes to designing a radiating antenna. For a radiating aperture antenna, the discontinuity at the aperture-free space transition needs to be considered. Therefore, some literature study was done to model the aperture-freespace transition. The methods are discussed in detail in chapter 5. There are several ways to address this problem.

One candidate for this problem is known as the Boundary Contour Mode Matching Technique (BCMM). In this method, the free space is considered as the summation of several spherical TE (Transverse Electric) and TM (Transverse Magnetic) modes. This implementation can be found in [26] [27]. This method requires a common origin for the co-ordinate systems considered for both the waveguide and free space. This is difficult to determine as inside the conical waveguide the waves are cylindrical in nature and outside the waveguide they are spherical in nature. This method is too involved as it consists of many numerical integrals which need to be defined on a single frame of reference for both the waveguide and free space.

The second technique is called the Gaussian Mode Beam Analysis (GBMA). This method is discussed in [10] and [32]. In this method, the fields on the aperture is approximated as scalar fields. Therefore, these methods are accurate for electrically very large objects (a few orders of wavelengths). Therefore, this is also not implemented in the thesis.

The third technique is based on Fredholm integral equations. This is based on energy conservation law and in this case the far-field of an equivalent current distribution is approximated as cylindrical waves. This is done by using Green's functions of free space in the cylindrical co-ordinate system. This method is elaborated in [7], [6] and [19]. The integrals mentioned in [19] are referred as Mishustin integrals in this thesis. These integrals are inspired from [15]. The limitation of this method is that for simplicity, it doesn't include higher order modes excitation at the aperture-free space transition and only calculates the reflection coefficient of the fundamental mode with itself. This is implemented in chapter 5. The results are compared with the fourth method mentioned below.

The fourth method that was explored is a spectral domain energy balance method which is based on Rumsey's reaction concept. The implementation of this can be found in [22] for rectangular waveguide to free space transition. This method is based on energy conservation at the aperture with electric and magnetic field continuity boundary conditions. This is used in the thesis in chapter 5. As it is a spectral domain method, it doesn't require to have a common reference frame to compute the fields. In addition to that, it also considers higher order modes excitation at the aperture boundary. In [22], this is developed for only rectangular waveguides, the fundamental mode of which is always linearly polarized in one direction only. This makes the computation easier. In this thesis, this method is used for cylindrical waveguides, where there exists both the polarizations even for the fundamental mode (radial and azimuthal variation). Using the integrals developed for the reflection at the aperture-free space transition for a cylindrical waveguide (Usually mentioned as K space integrals in the thesis), the reflection coefficients are determined. Analytical expressions are also obtained to calculate the far-fields of from a cylindrical waveguide using the aperture current distribution for the modes of type $TE_{1,n}$.

1.2.3. Chosen approaches

The mode matching technique was used for cylindrical to cylindrical waveguide junction problems and the cascaded model to approximate a conical horn. This method is made purely analytical in the thesis.

This method is a quicker way to find properties as the S parameters, the near-fields and the far-fields of the conical horn antenna when it is perfectly matched (Theoretically for an infinite length waveguide horn).

The Rumsey's reaction concept (K space integrals) is further developed to determine the reflection coefficients of modes (of the same azimuthal order as the fundamental mode) present in the aperture and possible higher order mode excitation due to the discontinuity at the aperture of an open waveguide problem.

Therefore, the entire software is a hybrid technique incorporating the MM and the K space integrals to determine the S parameters, the near-fields and the far-fields of the finite length open waveguide horn antenna.

1.3. The contributions made in this thesis project

There are several contributions made in the course of the thesis project. The following list covers them.

- Development of reflection at the aperture-free space transition using Rumsey's method (with K space integrals).
- A novel hybrid technique using both the MM software and the K space integrals to accurately formulate the diffraction free near-fields on the aperture of the conical horn antenna and, far-fields radiated due to the near-fields on the aperture.
- Analytical Mode Matching Software for cylindrical waveguide cascade model.
- Efficient and faster (improved CPU time and run time of simulation as compared to commercial tools) coding techniques for the calculation of different properties of the horn antenna using MATLAB.
- Goal functions for various output parameters of the horn like the return loss, the relative cross polarization and aperture efficiency.

1.4. Structure of the document

Chapter 2 is dedicated to the electromagnetic modes propagating in a cylindrical waveguide and the electric and magnetic field patterns on the aperture of a fully matched cylindrical waveguide. A comparison with the commercial tool called FEKO is also shown for the field patterns.

Chapter 3 introduces of MM technique with one waveguide junction (2 waveguide problem). This chapter also includes analytical derivations for the General Scattering Matrix (GSM) for the 2 waveguide problem. FEKO/CST simulations are also compared with the MM results from MATLAB for the scattering parameters. Explanations to the comparison with FEKO/CST, convergence criteria and modal analysis is also included for this problem.

Chapter 4 deals with the calculation of GSM when there are 3 or more than 3 cascaded cylindrical waveguide elements. FEKO/CST comparison, convergence and modal analysis is also shown in this chapter for a 3 waveguide, 5 waveguide and an approximate conical waveguide problem with different number of cylindrical cascaded waveguide elements.

Chapter 5 introduces the aperture near-field distribution of a cascaded waveguide problem and for an approximate conical waveguide problem. Comparisons with FEKO is also there in this chapter. These simulations are done when a perfectly absorbing port is present at the far end of the waveguide, or theoretically, the waveguide at the far end is infinite in length. Therefore, chapter 5 addresses the free space-aperture transition of cylindrical waveguides as well.

Chapter 6 deals with the explanations for the optimization routines and the goal functions to achieve various requirements for the antenna design.

In chapter 7, the results are shown with commercial tool equivalent models as well. Chapter 8 consists of the conclusions drawn from the thesis project and future recommendations.

2

Circular Cross-Section Waveguides: Near Field Patterns

2.1. Problem formulation

Let us consider circular waveguide formed by a closed perfectly electrically conducting (PEC) surface with circular cross-section. The axis of this surface coincides with z-axis of the cylindrical coordinate system. Two types of waveguide modes can propagate in such waveguide: TE (Transverse Electric) and TM(Transverse Magnetic) modes. These modes are considered in details in the following sections. This is done by a text book approach of [3].

2.2. TE^z modes:

The TE modes can be derived from the vector potentials A (Electric field potential) and F (Magnetic field potential).

$$A = 0 \tag{2.1}$$

$$F = \hat{z}F_z(\rho, \phi, z) \tag{2.2}$$

A cylindrical coordinate system is preferred in this case because of the ease of analysis of a cylindrical domain. The vector potential F should satisfy the following Helmholtz equation:

$$\nabla^2 F_z((\rho, \phi, z)) + \beta^2 F_z(\rho, \phi, z) = 0 \tag{2.3}$$

This reduces down to:

$$\frac{\partial^2 F_z}{\partial \rho^2} + \frac{1}{\rho}\frac{\partial F_z}{\partial \rho} + \frac{1}{\rho^2}\frac{\partial^2 F_z}{\partial \phi^2} + \frac{\partial^2 F_z}{\partial z^2} = -\beta^2 F_z \tag{2.4}$$

If we assume a solution with three independent functions of ρ, ϕ and z, we have:

$$F_Z(\rho, \phi, z) = f(\rho)g(\phi)h(z) \tag{2.5}$$

Using this on equation 2.4, we have:

$$gh\frac{\partial^2 f}{\partial \rho^2} + gh\frac{1}{\rho}\frac{\partial f}{\partial \rho} + fh\frac{1}{\rho^2}\frac{\partial^2 g}{\partial \phi^2} + fg\frac{\partial^2 h}{\partial z^2} = -\beta^2 fgh \tag{2.6}$$

Dividing both sides by fgh, we have:

$$\frac{1}{f}\frac{\partial^2 f}{\partial \rho^2} + \frac{1}{f}\frac{1}{\rho}\frac{\partial f}{\partial \rho} + \frac{1}{g}\frac{1}{\rho^2}\frac{\partial^2 g}{\partial \phi^2} + \frac{1}{h}\frac{\partial^2 h}{\partial z^2} = -\beta^2 \tag{2.7}$$

As the z dependence is only on the phase as it is a travelling wave along z, we can write:

$$\frac{\partial^2 h}{\partial z^2} = -\beta_z^2 h \tag{2.8}$$

Where, β_z is the wavenumber along the z direction.

Substituting this on equation 2.7 and multiplying ρ^2 we have:

$$\frac{\rho^2}{f}\frac{\partial^2 f}{\partial \rho^2} + \frac{\rho}{f}\frac{\partial f}{\partial \rho} + \frac{1}{g}\frac{\partial^2 g}{\partial \phi^2} + \rho^2(\beta^2 - \beta_z^2) = 0 \tag{2.9}$$

We can replace the term $\frac{1}{g}\frac{\partial^2 g}{\partial \phi^2}$ as a constant as g only depends on ϕ, therefore,

$$\frac{1}{g}\frac{\partial^2 g}{\partial \phi^2} = -m^2 \tag{2.10}$$

$\Rightarrow$

$$\frac{\partial^2 g}{\partial \phi^2} = -m^2 g \tag{2.11}$$

As we know that the wavenumber's ρ component can be found as $\beta_\rho^2 = \beta^2 - \beta_z^2$, we can reduce the equation 2.9 as follows:

$$\rho^2\frac{\partial^2 f}{\partial \rho^2} + \rho\frac{\partial f}{\partial \rho} + [(\beta_\rho \rho)^2 - m^2]f = 0 \tag{2.12}$$

This resembles Bessel's differential equation. The solutions are of the form:

$$F_z(\rho, \phi, z) = f(\rho)g(\phi)h(z) = [A_1 J_m(\beta_\rho \rho) + B_1 Y_m(\beta_\rho \rho)][C_2 \cos(m\phi) + D_2 \sin(m\phi)][A_3 e^{-j\beta_z z} + B_3 e^{j\beta_z z}] \tag{2.13}$$

These solutions for f, g and h were chosen because for this cylindrical waveguide it is more practical to think of standing waves along the ϕ direction, standing waves along the ρ direction and travelling waves on the z direction. Here J_m and Y_m are the Bessel functions of first and second kind.

To find out the constants, the boundary conditions have to be applied:

The boundary conditions (BCs) are (where a is the radius of the cross section of the waveguide):

- $E_\phi(\rho = a, \phi, z) = 0$
- The fields must be finite everywhere
- The field must repeat after 2π radian in ϕ.

Following the second BC, we have $B_1 = 0$ as $Y_m(\rho = 0) = \infty$. According to the third BC of DEeriodicity over ϕ, we can conclude that $m = 0, 1, 2, 3....$ If we consider no reflection from the other boundary of the waveguide ($B_3 = 0$), we can rewrite the equation 2.13 as:

$$F_z(\rho, \phi, z) = A_{mn} J_m(\beta_\rho \rho)[C_2 \cos(m\phi) + D_2 \sin(m\phi)]e^{-j\beta_z z} \tag{2.14}$$

Therefore, for this completely matched (No reflection) waveguide, the ϕ component of the electric field is:

$$E_\phi(\rho, \phi, z) = \frac{1}{\epsilon}\frac{\partial F_z}{\partial \rho} = A_{mn}\frac{\beta_\rho}{\epsilon} J_m'(\beta_\rho \rho)[C_2 \cos(m\phi) + D_2 \sin(m\phi)]e^{-j\beta_z z} \tag{2.15}$$

Using the first BC, we have:

$$E_\phi(\rho = a, \phi, z) = A_{mn}\frac{\beta_\rho}{\epsilon} J_m'(\beta_\rho a)[C_2 \cos(m\phi) + D_2 \sin(m\phi)]e^{-j\beta_z z} \tag{2.16}$$

This can only be true if:

$$J_{mn}'(\beta_\rho a) = 0 \tag{2.17}$$

$\Rightarrow$

$$\beta_\rho = \frac{\chi_{mn}'}{a} \tag{2.18}$$

Where, χ_{mn}' is the nth zero of the derivative of the Bessel's function J_m of the first kind of the order m (0, 1, 2, 3,...).

The β_z of the TE_{mn} mode can be written as:

$$(\beta_z)_{mn} = -j\sqrt{-(\beta^2 - \beta_\rho^2)} \tag{2.19}$$

This way of representing makes it easier to visualise that $(\beta_z)_{mn}$ is purely real when $\beta > \beta_\rho$, purely imaginary when $\beta < \beta_\rho$ and 0 when $\beta = \beta_\rho$. Therefore, cut-off is determined by:

$$(\beta_z)_{mn} = 0 \tag{2.20}$$

$\Rightarrow$

$$\beta_c = \omega_c\sqrt{\mu\epsilon} = \beta_\rho \tag{2.21}$$

$\Rightarrow$

$$(f_c)_{mn} = \frac{\chi'_{mn}}{2\pi a\sqrt{\mu\epsilon}} \tag{2.22}$$

The electric field equations for a perfectly matched cylindrical waveguide are:

$$E_\rho = -\frac{1}{\epsilon\rho}\frac{\partial F_z}{\partial \phi} = -A_{mn}\frac{m}{\epsilon\rho}J_m(\beta_\rho\rho)[-C_2\sin(m\phi) + D_2\cos(m\phi)]e^{-j\beta_z z} \tag{2.23}$$

$$E_\phi = \frac{1}{\epsilon}\frac{\partial F_z}{\partial \rho} = A_{mn}\frac{\beta_\rho}{\epsilon}J'_m(\beta_\rho\rho)[C_2\cos(m\phi) + D_2\sin(m\phi)]e^{-j\beta_z z} \tag{2.24}$$

$$E_z = 0 \tag{2.25}$$

The magnetic field equations for a perfectly matched cylindrical waveguide are:

$$H_\rho = -j\frac{1}{\omega\mu\epsilon}\frac{\partial^2 F_z}{\partial\rho\partial z} = -A_{mn}\frac{\beta_\rho\beta_z}{\omega\mu\epsilon}J'_m(\beta_\rho\rho)[C_2\cos(m\phi) + D_2\sin(m\phi)]e^{-j\beta_z z} \tag{2.26}$$

$$H_\phi = -j\frac{1}{\omega\mu\epsilon}\frac{1}{\rho}\frac{\partial^2 F_z}{\partial\phi\partial z} = -A_{mn}\frac{m\beta_z}{\omega\mu\epsilon}\frac{1}{\rho}J_m(\beta_\rho\rho)[-C_2\sin(m\phi) + D_2\cos(m\phi)]e^{-j\beta_z z} \tag{2.27}$$

$$H_z = -j\frac{1}{\omega\mu\epsilon}(\frac{\partial^2}{\partial z^2} + \beta^2)F_z = -jA_{mn}\frac{\beta_\rho^2}{\omega\mu\epsilon}J_m(\beta_\rho\rho)[C_2\cos(m\phi) + D_2\sin(m\phi)]e^{-j\beta_z z} \tag{2.28}$$

The impedance of the wave for TE modes, hence, can be determined as:

$$(Z_w)^{TE}_{mn} = \frac{E_\rho}{H_\phi} = \frac{-E_\phi}{H_\rho} = \frac{\omega\mu}{(\beta_z)_{mn}} \tag{2.29}$$

Therefore, impedance of the wave is real above cut-off and imaginary below the cut-off and inductive. Below cut-off, it stores energy. Exactly at cut-off the impedance is very high (∞).

2.3. TM^z modes:

The same analysis can be done for the TM mode with the electric potential function.

$$F = 0 \tag{2.30}$$

$$A = \hat{z}A_z(\rho, \phi, z) \tag{2.31}$$

And the boundary conditions are:

- $E_\phi(\rho = a, \phi, z) = 0$

- $E_z(\rho = a, \phi, z) = 0$
- The fields must be finite everywhere
- The field must repeat after 2π radians in ϕ.

Using these, the solution to the partial differential equation (PDE) for a perfectly matched waveguide (No reflection) can be written as:

$$A_z(\rho, \phi, z) = B_{mn} J_m(\beta_\rho \rho)[C_2 \cos(m\phi) + D_2 \sin(m\phi)]e^{-j\beta_z z} \tag{2.32}$$

Using the second BC, it can be shown that,

$$J_m(\beta_\rho a) = 0 \tag{2.33}$$

$\Rightarrow$

$$\beta_\rho = \frac{\chi_{mn}}{a} \tag{2.34}$$

Where, χ_{mn} is the nth zero of the Bessel's function J_m of the first kind of the order m (0, 1, 2, 3,...).

cut-off frequency can be given as:

$$(f_c)_{mn} = \frac{\chi_{mn}}{2\pi a\sqrt{\mu\epsilon}} \tag{2.35}$$

The magnetic field equations for a perfectly matched cylindrical waveguide are:

$$H_\rho = \frac{1}{\mu\rho}\frac{\partial A_z}{\partial \phi} = B_{mn}\frac{m}{\mu\rho} J_m(\beta_\rho \rho)[-C_2 \sin(m\phi) + D_2 \cos(m\phi)]e^{-j\beta_z z} \tag{2.36}$$

$$H_\phi = \frac{1}{\mu}\frac{\partial A_z}{\partial \rho} = -B_{mn}\frac{\beta_\rho}{\mu} J'_m(\beta_\rho \rho)[C_2 \cos(m\phi) + D_2 \sin(m\phi)]e^{-j\beta_z z} \tag{2.37}$$

$$H_z = 0 \tag{2.38}$$

The electric field equations for a perfectly matched cylindrical waveguide are:

$$E_\rho = -j\frac{1}{\omega\mu\epsilon}\frac{\partial^2 A_z}{\partial\rho\partial z} = -B_{mn}\frac{\beta_\rho\beta_z}{\omega\mu\epsilon} J'_m(\beta_\rho \rho)[C_2 \cos(m\phi) + D_2 \sin(m\phi)]e^{-j\beta_z z} \tag{2.39}$$

$$E_\phi = -j\frac{1}{\omega\mu\epsilon}\frac{1}{\rho}\frac{\partial^2 A_z}{\partial\phi\partial z} = -B_{mn}\frac{m\beta_z}{\omega\mu\epsilon}\frac{1}{\rho} J_m(\beta_\rho \rho)[-C_2 \sin(m\phi) + D_2 \cos(m\phi)]e^{-j\beta_z z} \tag{2.40}$$

$$E_z = -j\frac{1}{\omega\mu\epsilon}\left(\frac{\partial^2}{\partial z^2} + \beta^2\right)A_z = -jB_{mn}\frac{\beta_\rho^2}{\omega\mu\epsilon} J_m(\beta_\rho \rho)[C_2 \cos(m\phi) + D_2 \sin(m\phi)]e^{-j\beta_z z} \tag{2.41}$$

The impedance of the wave for TM modes, hence, can be determined as:

$$(Z_w)_{mn}^{TM} = \frac{E_\rho}{H_\phi} = \frac{-E_\phi}{H_\rho} = \frac{(\beta_z)_{mn}}{\omega\epsilon} \tag{2.42}$$

2.4. Results: Near field or the field distribution on the aperture

The above equations for near field pattern were plotted in MATLAB. For the plots, I have taken the constant $C_2 = 1$ and $D_2 = 0$. The plot is at a particular cross-section (z = 0).

The TE modes are shown in figure 2.1. For TE modes, the surface plot is the Electric field and the quiver plots (field lines) are for the magnetic field. The TM modes are shown in figure 2.2. For TM modes, the surface plots are magnetic field and the quiver plots (field lines) are for the electric field.

In all these MATLAB simulations, the frequency was chosen to be a little bit higher than the cut-off frequency of the respective modes.

Some results from Feko simulation are shown in figure 2.3. The patterns exactly match the analytical solution plotted in MATLAB. The solver in Feko was Method of Moments (MoM). The source for this cylindrical structure was chosen to be a waveguide source which allows a certain mode. The cylinder is shown in figure 2.4. It is a cylinder of which one of the sides is absorbing (waveguide port with no excitation) and the other side is excited by a waveguide source.

2.5. Conclusions

In this chapter, TE and TM propagating modes of a circular cross section (cylindrical) waveguide have been studied. Analytical expressions for the near fields have been derived. The analytical expressions have been implemented on MATLAB and have been compared with direct full wave numerical solutions of Maxwell's equation in FEKO commercial tool with Method of Moments (MoM) solver. A good agreement has been observed between the two implementations which verifies the correctness of the MATLAB routines built with the analytical solutions.

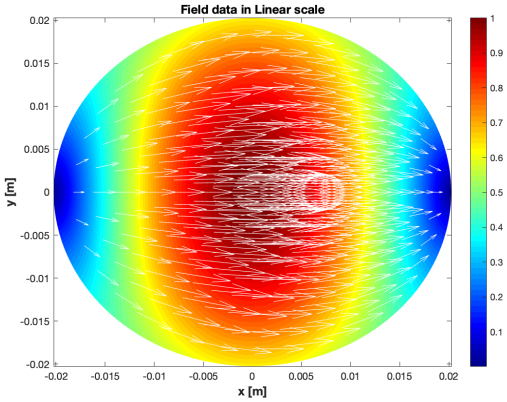

(a) TE_{11}

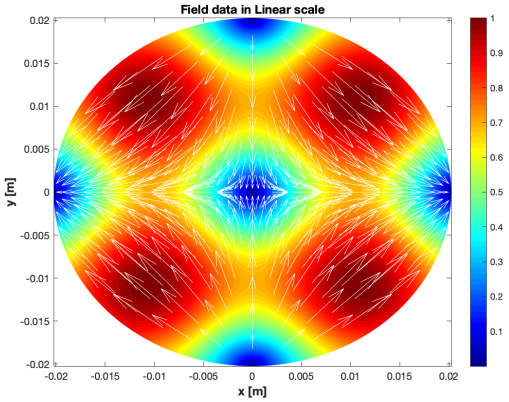

(b) TE_{21}

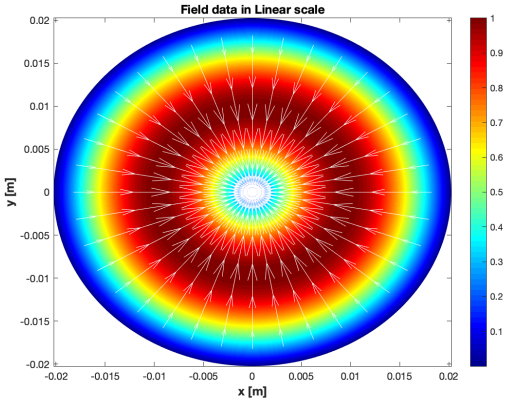

(c) TE_{01}

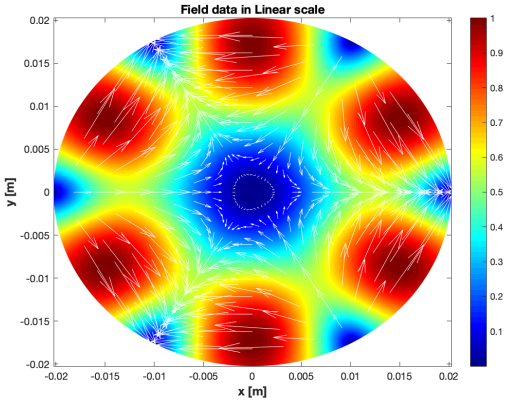

(d) TE_{31}

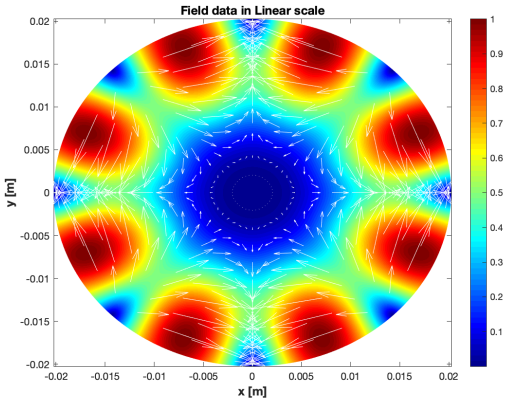

(e) TE_{41}

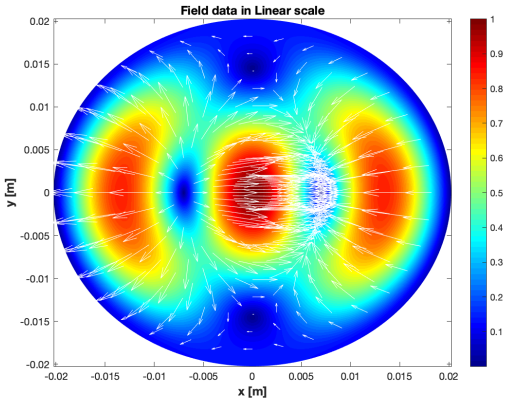

(f) TE_{12}

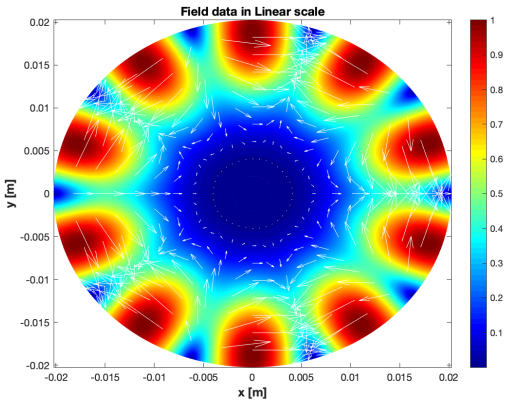

(g) TE_{51}

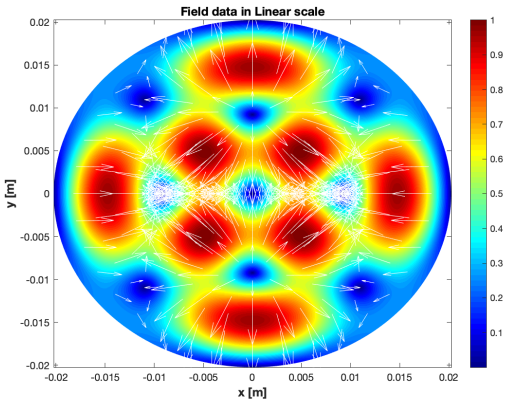

(h) TE_{22}

Figure 2.1: E and H fields of TE mode. E field surface plot. H field quiver plot.

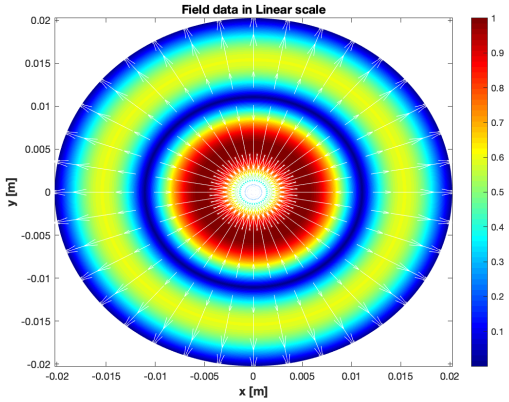

(i) TE_{02}

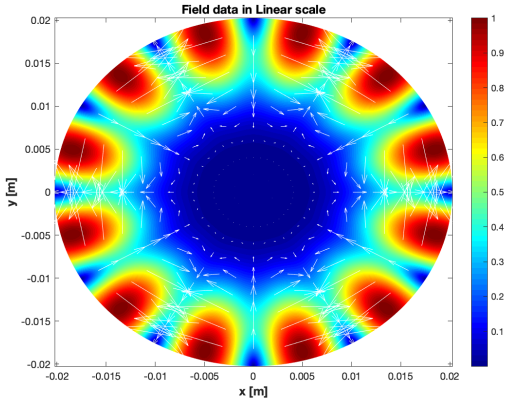

(j) TE_{61}

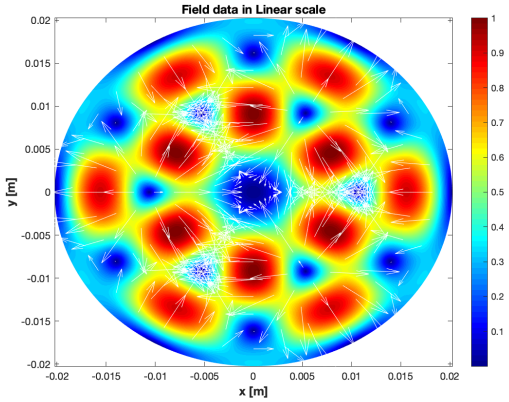

(k) TE_{32}

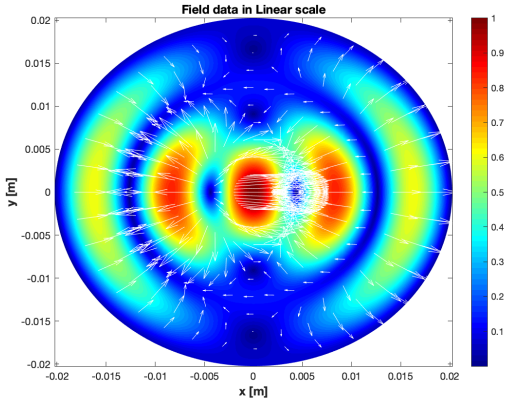

(l) TE_{13}

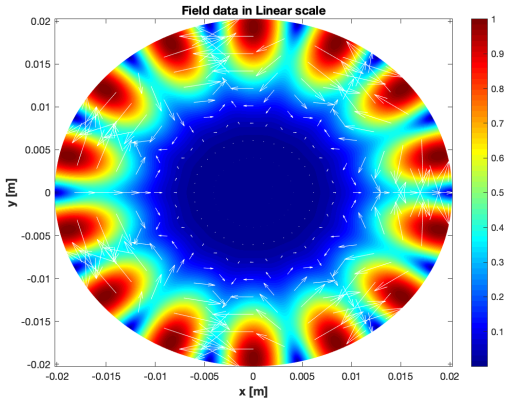

(m) TE_{71}

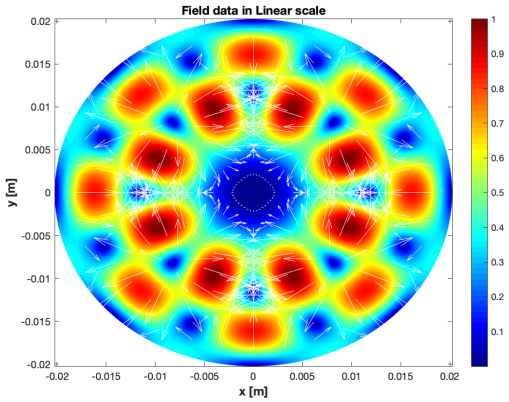

(n) TE_{42}

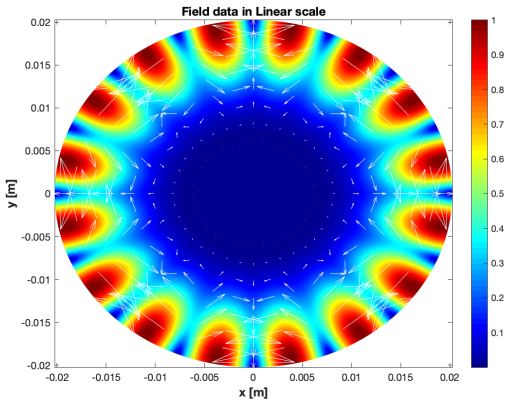

(o) TE_{81}

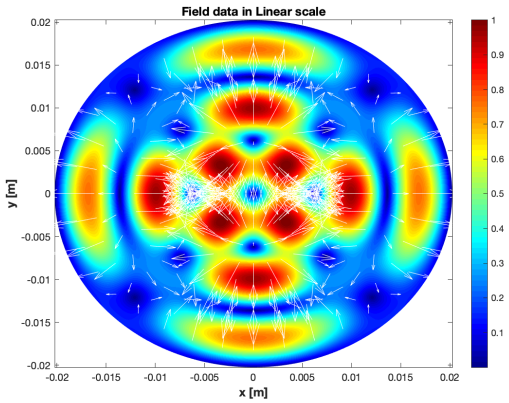

(p) TE_{23}

Figure 2.1: E and H fields of TE mode. E field surface plot. H field quiver plot.(cont.)

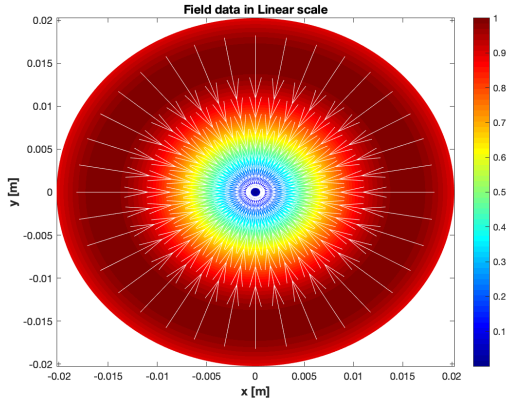

(a) TM_{01}

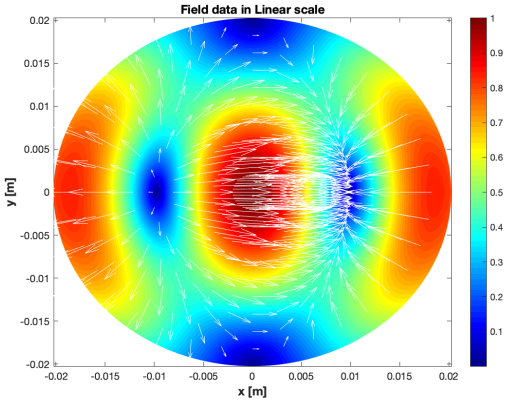

(b) TM_{11}

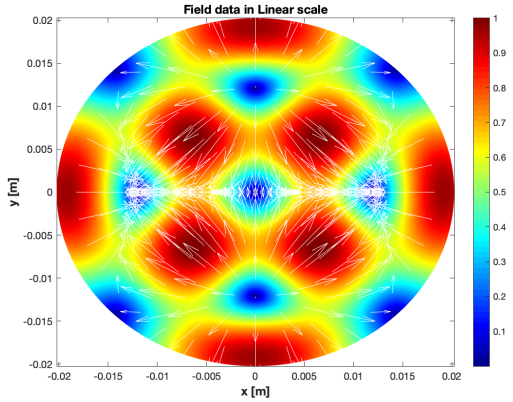

(c) TM_{21}

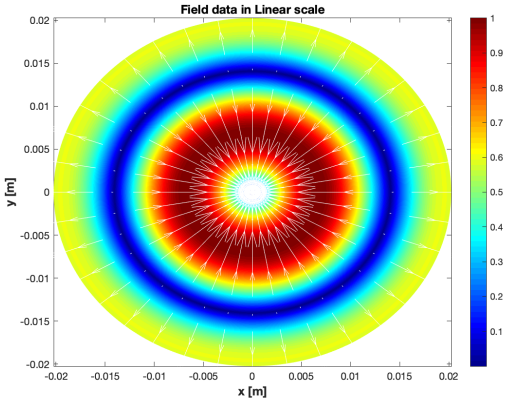

(d) TM_{02}

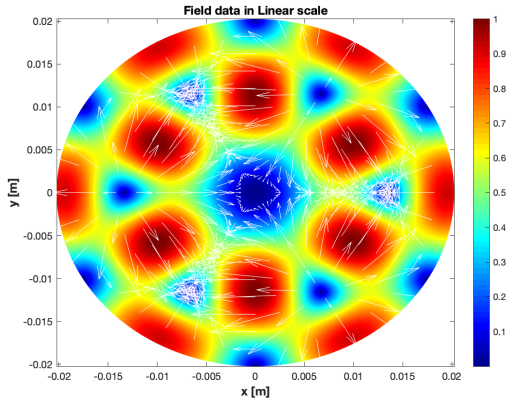

(e) TE_{31}

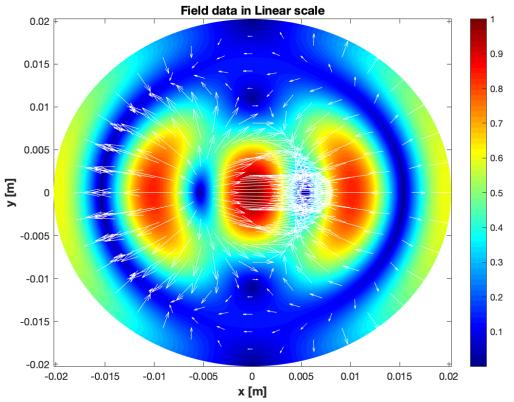

(f) TM_{12}

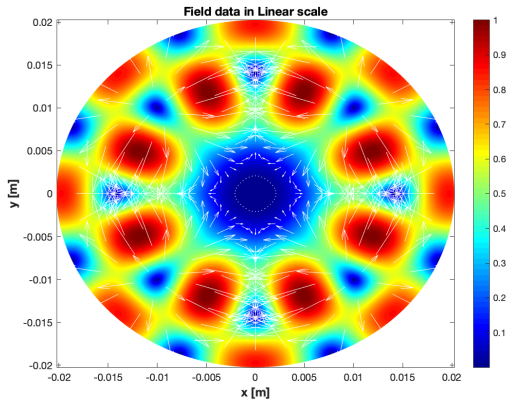

(g) TM_{41}

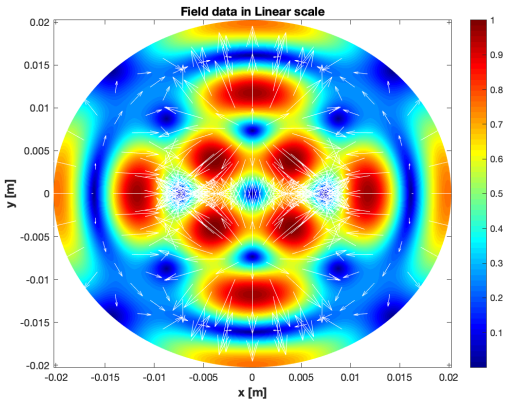

(h) TM_{22}

Figure 2.2: E and H fields of TM mode. H field surface plot. E field quiver plot.

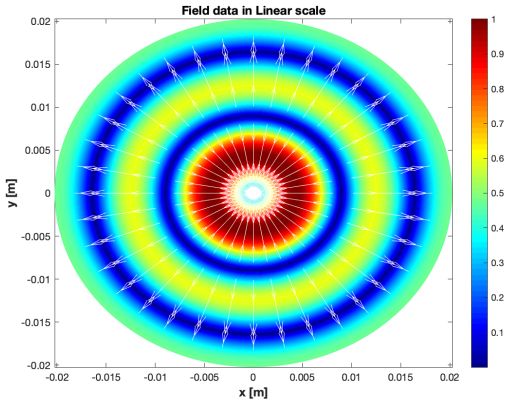

(i) TM_{03}

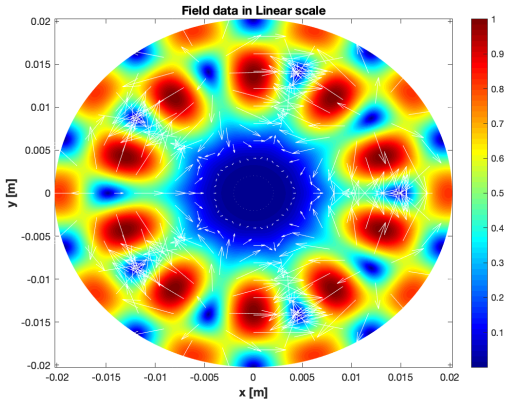

(j) TM_{51}

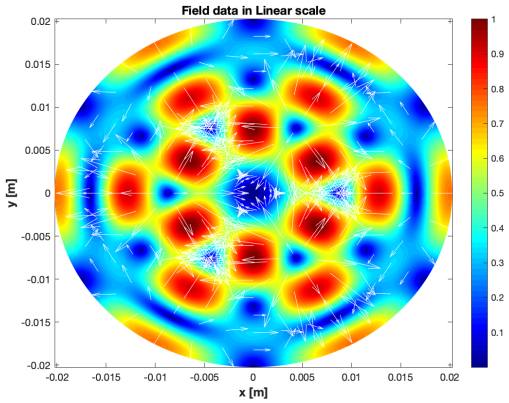

(k) TM_{32}

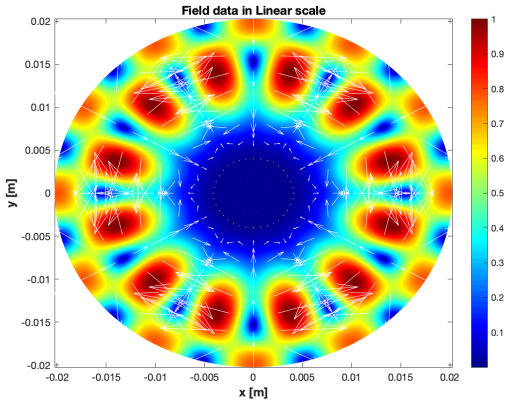

(l) TM_{61}

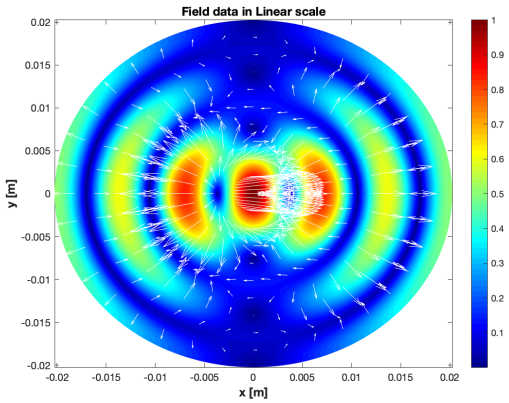

(m) TM_{13}

Figure 2.2: E and H fields of TM mode. H field surface plot. E field quiver plot. (Cont.)

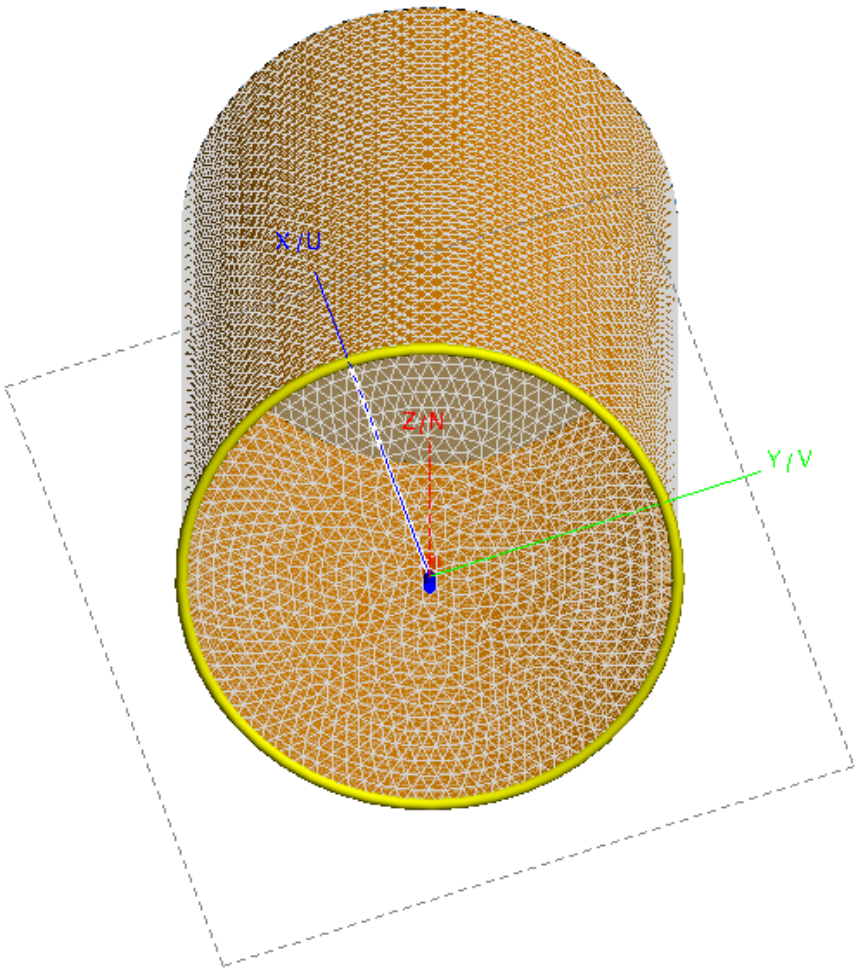

Figure 2.3: Feko Cylinder structure.

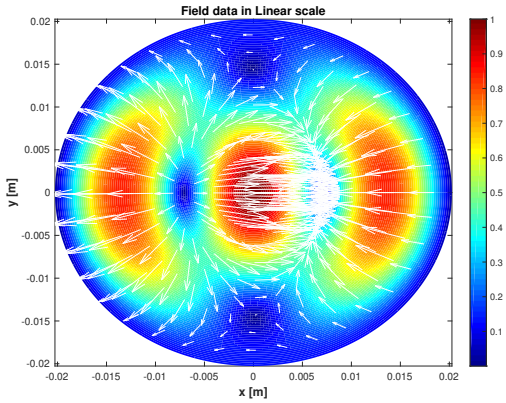

(a) E field TE_{12}

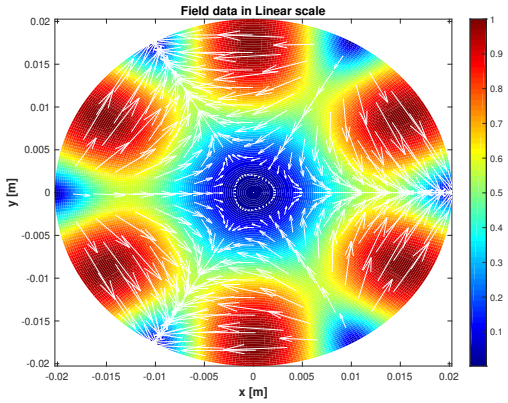

(b) E field TE_{31}

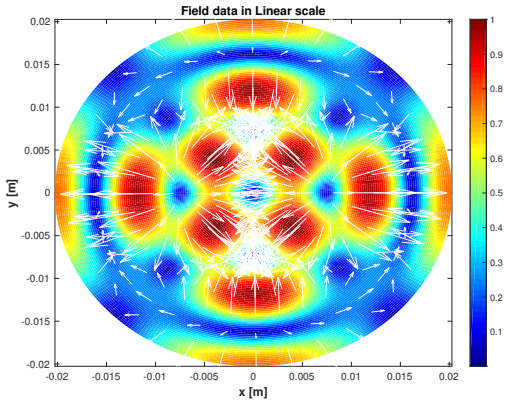

(c) H field TM_{22}

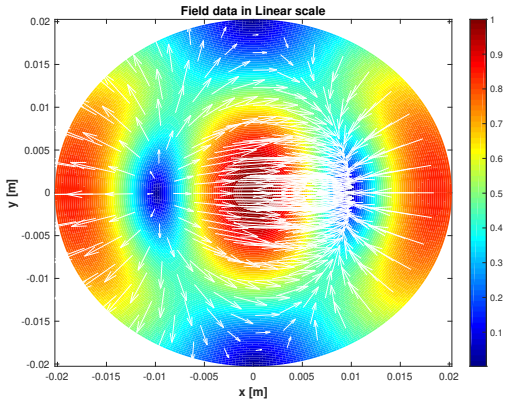

(d) H field TM_{11}

Figure 2.4: E- and H-fields in Feko for some TE and TM modes.

3

Two Circular Cross-Section Waveguides with Mode Matching Technique

3.1. Problem formulation

In this chapter, two circular cross-section waveguides are studied. They are connected to each other at $z = 0$.The problem is shown in figure 3.1. The junction problem is studied with the mode matching technique (MM).

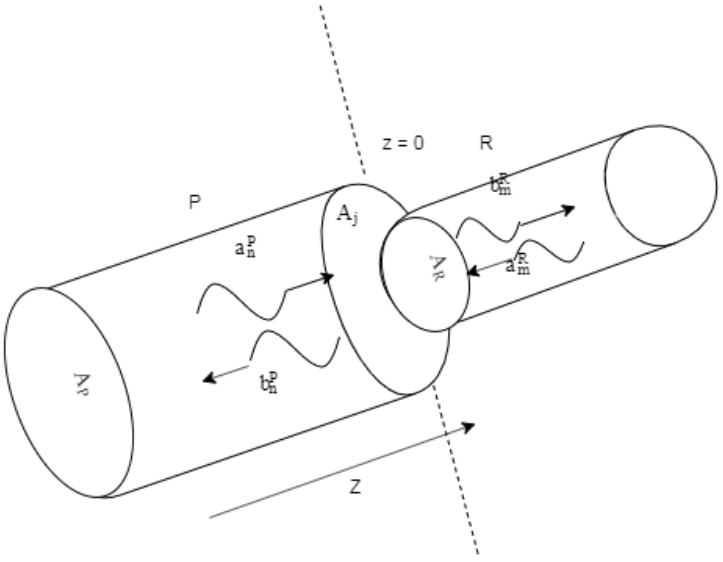

Figure 3.1: Two circular waveguides of different radii connected at z = 0.

3.2. Field Expressions for Circular Cross Section Waveguide

This problem can be solved by determining the GSM (General Scattering Matrix). Here, the two sections at the junctions can be thought as two ports and the characteristic of the reflection and transmission coefficients can be determined using the GSM. From previous chapter we already know the field equations for the two waveguides. For the waveguide P, the total electric field can be written simply as,

$$\vec{E}_t^P|_{A_P,z=0^-} = \sum_{n=1}^{N_P} (a_n^P + b_n^P)\vec{E}_n^P \tag{3.1}$$

$$\vec{H}_t^P|_{A_P,z=0^-} = \sum_{n=1}^{N_P} (a_n^P - b_n^P)\vec{H}_n^P \tag{3.2}$$

Similarly for the waveguide R, it can be written as,

$$\vec{E}_t^R|_{A_R,z=0^+} = \sum_{m=1}^{N_R} (a_m^R + b_m^R)\vec{E}_n^R \tag{3.3}$$

$$\vec{H}_t^R|_{A_R,z=0^+} = \sum_{m=1}^{N_R} (b_m^R - a_m^R)\vec{H}_n^R \tag{3.4}$$

Here, N_P and N_R are the number of modes considered in waveguide P and R respectively. Every mode is orthogonal.

3.3. Mode Matching Technique (The MM analytical software)

3.3.1. Formulation of the Normalization Constant Q for each Mode and its Numerical solution

Normalization constant for a waveguide is necessary in the mode matching software because the model is based on energy conservation or balance between two different waveguides for a junction problem. The normalization makes sure that the energy is noramlized on both sides of the junction in a similar way.

An arbitrary normalization coefficient for each mode in the waveguides can be calculated by the following relation.

$$\int\int_{A_{area}} (\vec{E}_n^{area} \times \vec{H}_m^{area}).\hat{z}dS = Q_n^{area}\delta_{nm} \tag{3.5}$$

Here $area$ can be both P and R. The δ function is 1, when $m = n$ and 0 otherwise. This explains that the modes are orthogonal.

This quantity shows how many modes are propagating and how many are evanescent. It is slightly different from the Poynting vector which is given as:

$$\int\int_{A_{area}} (\vec{E}_n^{area} \times \vec{H}^{*\,area}_m).\hat{z}dS = Y_m^* \int\int_{A_{area}} (\vec{E}_n^{area}.\vec{E}^{*\,area}_m)dS = Z_n \int\int_{A_{area}} (\vec{H}_n^{area}.\vec{H}^{*\,area}_m)dS = P_n^{area}\delta_{nm} \tag{3.6}$$

Therefore, the normalization constant Q is related to the Poynting vector P as the following:

$$P_n = \frac{\sqrt{Z_n}}{\sqrt{Z_n^*}}|Q_n| \tag{3.7}$$

For verification, the normalization constant Q was plotted at a certain frequency for a number of modes in both TE and TM. The plot is shown in figure 3.2. The double integral is done on the cross-section surface of the waveguide. In this case the double integral looks like $\int_0^a \int_0^{2\pi}$ to specify the circle in cylindrical coordinates.

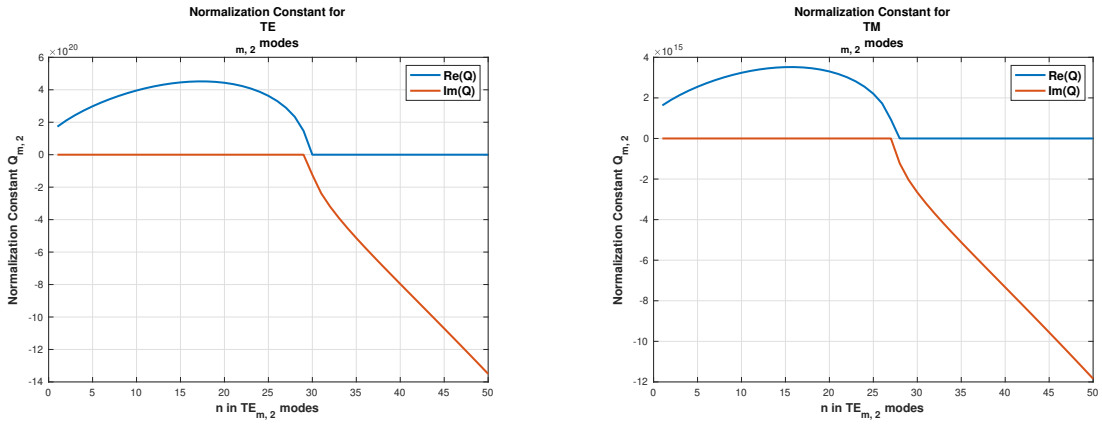

(a) Q_m vs m in $TE_{m,2}$ modes

(b) Q_m vs m in $TM_{m,2}$ modes

Figure 3.2: Normalization constant for the modes both in TE and TM

The radius of the waveguide for this simulation was kept as $r = 2.03[cm]$ and the frequency of operation was 90 GHz. It can be seen from the figure that for the TE modes, at $TE_{30,2}$, the normalization becomes purely imaginary. And before that from $TE_{2,1}$ to $TE_{29,2}$, the nornalization was purely real suggesting that there is no real power after $TE_{29,2}$ mode for 90 GHz. It was found that the cut-off for $TE_{29,2}$ is 88.414 GHz and the cut-off for $TE_{30,2}$ is 90.963 GHz. As the operational frequency was 90 GHz, it couldn't excite modes after $TE_{30,2}$. Similarly for TM mode, at $TE_{28,2}$ mode, the normalization becomes purely imaginary because the cut-off at $TM_{27,2}$ is 88.949 GHz and the cut-off at $TM_{28,2}$ is 91.553 GHz.

3.3.2. An analytical approach for Solving for Normalization Constant Q

Using equation (3.5) we have at $z = 0$:

$$Q_n^{area}\delta_{nm} = \int\int_{A_{area}} (\vec{E}_n^{area} \times \vec{H}_m^{area}).\hat{z}dS = \int\int_{A_{area}} [\vec{E}_{\rho n}^{area}\vec{H}_{\phi m}^{area} - \vec{E}_{\phi n}^{area}\vec{H}_{\rho m}^{area}]\rho d\rho d\phi \tag{3.8}$$

Using equations from chapter 2 (2.23, 2.24, 2.26 and 2.27) for TE modes, we get:

$$Q_n^{area}\delta_{nm} = \int\int_{A_{area}} K_{mnTE}\left[\frac{m^2}{\rho^2}J_m^2(\beta_{\rho(m,n)}\rho)\sin^2(m\phi) + \beta_{\rho(m,n)}^2 J_m'^2(\beta_{\rho(m,n)}\rho)\cos^2(m\phi)\right]\rho d\rho d\phi \tag{3.9}$$

Where K_{mnTE} is defined as:

$$K_{mnTE} = \frac{A_{mn}^2\beta_{z,mn}C_2^2}{\omega\mu\epsilon^2} \tag{3.10}$$

From properties of Bessel's function of the first kind, we know that,

$$J_\nu'(Z) = \frac{J_{\nu-1}(Z) - J_{\nu+1}(Z)}{2} \tag{3.11}$$

And,

$$\frac{2\nu J_\nu(Z)}{Z} = J_{\nu-1}(Z) + J_{\nu+1}(Z) \tag{3.12}$$

Using these properties the integral can be re-written as:

$$Q_n^{area}\delta_{nm} = K_{mnTE}\frac{\beta_{\rho(m,n)}^2}{4}\left[(I_A + I_C)(I_{sin} + I_{cos}) + 2I_B(I_{sin} - I_{cos})\right] \tag{3.13}$$

The terms in the above equation (3.13) are defined as:

$$I_{sin} = \int_0^{2\pi} sin^2(m\phi)d\phi = \pi \tag{3.14}$$

$$I_{cos} = \int_0^{2\pi} cos^2(m\phi)d\phi = \pi \tag{3.15}$$

$$I_A = \int_0^r J_{m-1}^2(\beta_{\rho(m,n)}\rho)\rho d\rho \tag{3.16}$$

$$I_B = \int_0^r J_{m-1}(\beta_{\rho(m,n)}\rho)J_{m+1}(\beta_{\rho(m,n)}\rho)\rho d\rho \tag{3.17}$$

$$I_C = \int_0^r J_{m+1}^2(\beta_{\rho(m,n)}\rho)\rho d\rho \tag{3.18}$$

Here, the surface integral is divided into two parts; one dependent on ρ and the other one dependent on ϕ. This was possible because it was assumed in chapter 2 that the field solutions to a cylindrical (circular cross-section) waveguides are a multiplication of independent functions.

I_A and I_C can be solved analytically by using Lommel's integrals [2] and [5] (Equation 3.19).

$$\int_0^r J_\nu^2(\beta_{\rho(m,n)}\rho)\rho d\rho = \frac{1}{2}a^2(J_\nu(\beta_{\rho(m,n)}a)^2 - J_{\nu-1}(\beta_{\rho(m,n)}a)J_{\nu+1}(\beta_{\rho(m,n)}a)) \tag{3.19}$$

Finding out B is difficult and involves hyper-geometric functions as it has Bessel functions of different orders. However, using equation (3.14) and (3.15) ($I_{sin} = I_{cos} = \pi$), the final integral of equation (3.13) becomes:

$$Q_{nTE}^{area}\delta_{nm} = K_{mnTE}\frac{\beta_{\rho(m,n)}^2}{4}\left[(I_A + I_C)(I_{sin} + I_{cos})\right] \tag{3.20}$$

Therefore, the expression with B vanishes.

For TM mode also the solution is identical except the constant K_{mnTM} which is given as:

$$K_{mnTM} = \frac{B_{mn}^2 \beta_{z,mn} C_2^2}{\omega \mu^2 \epsilon} \tag{3.21}$$

Therefore, the solution is:

$$Q_{nTM}^{area} \delta_{nm} = K_{mnTM} \frac{\beta_{\rho(m,n)}^2}{4} \left[(I_A + I_C)(I_{sin} + I_{cos}) \right] \tag{3.22}$$

The plots with both numerical and the analytical solution is given in figure 3.3 with m = 1 and n varying from 1 to 50 at 200 GHz frequency. The analytical result matches the numerical result perfectly. For the numerical result, discretization in ρ dimension was taken as $\frac{r}{1000}$ and in ϕ dimension it was $\frac{\pi}{2000}$.

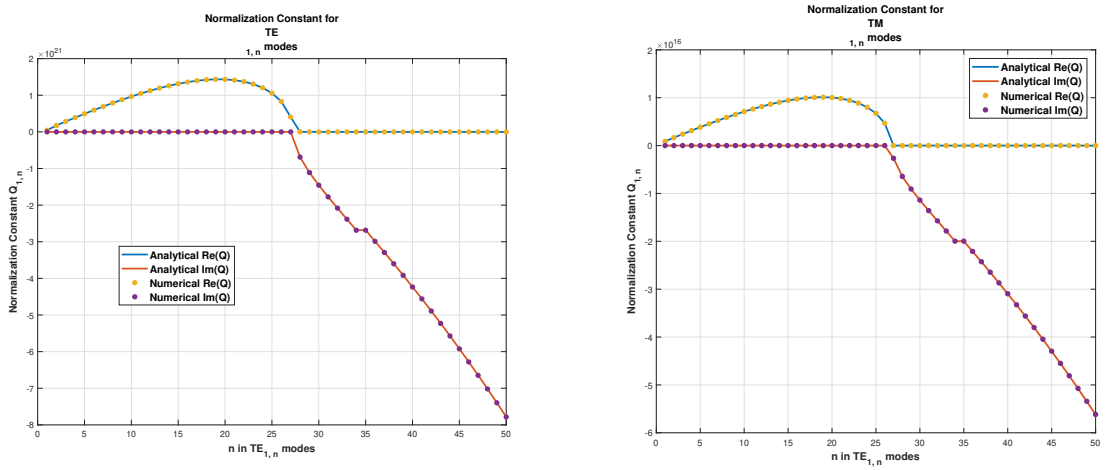

(a) Q_n vs n in $TE_{1,n}$ modes

(b) Q_n vs n in $TM_{1,n}$ modes

Figure 3.3: Normalization constant for the modes both in TE and TM

3.3.3. Mode Matching Technique

Here, A_R is a subset of A_P ($A_P = A_R + A_j$) and A_j is the excess area which is not connected to the waveguide R. The E- and H-field boundary conditions must be satisfied at the boundary of the two waveguides where they are connected.

- For E field:
  - $$\hat{z} \times \vec{E}^P = 0, \quad in \quad A_j, z = 0 \tag{3.23}$$
  - $$\hat{z} \times \vec{E}^P = \hat{z} \times \vec{E}^R, \quad in \quad A_R, z = 0 \tag{3.24}$$
- For H field:
  - $$\hat{z} \times \vec{H}^P = \hat{z} \times \vec{H}^R, \quad in \quad A_R, z = 0 \tag{3.25}$$

For boundary condition of electric field, we can project it to a magnetic field of all modes in the P waveguide. Therefore,

$$\int\int_{A_P}(\hat{z}\times\vec{E}^P).\vec{H}^P_{mode}\hat{z}dS=\sum_{n=1}^{N_P}(a_n^P+b_n^P)\int\int_{A_P}(\hat{z}\times\vec{E_n}^P).\vec{H}^P_{mode}\hat{z}dS \tag{3.26}$$

Where $mode$ refers to any waveguide mode.

As the modes are orthogonal to each other this can be rewritten as:

$$\int\int_{A_P}(\hat{z}\times\vec{E}^P).\vec{H}^P_{mode}\hat{z}dS=(a^P_{mode}+b^P_{mode})Q^P_{mode} \tag{3.27}$$

The left hand side of equation (3.26) can be calculated by dividing it into two sections (one over A_R and one over A_j).

$$\int\int_{A_P}(\hat{z}\times\vec{E}^P).\vec{H}^P_{mode}\hat{z}dS=\int\int_{A_R}(\hat{z}\times\vec{E}^P).\vec{H}^P_{mode}\hat{z}dS+\int\int_{A_j}(\hat{z}\times\vec{E}^P).\vec{H}^P_{mode}\hat{z}dS \tag{3.28}$$

From first boundary condition of electric field, we know that the second term in the right hand side of the equation (3.28) is 0. Therefore also using the second boundary condition,

$$\int\int_{A_P}(\hat{z}\times\vec{E}^P).\vec{H}^P_{mode}\hat{z}dS=\int\int_{A_R}(\hat{z}\times\vec{E}^R).\vec{H}^P_{mode}\hat{z}dS=\sum_{m=1}^{N_R}(a_m^R+b_m^R)\int\int_{A_R}\vec{E_m}^R\times\vec{H}^P_{mode}.\hat{z}dS \tag{3.29}$$

The term $\int\int_{A_R}\vec{E_m}^R\times\vec{H}^P_{mode}.\hat{z}dS$ is called the ***inner cross product*** and it includes the fields in the two waveguides at one integral. Therefore, the above relation can be rewritten as:

$$(a^P_{mode}+b^P_{mode})Q^P_{mode}=\sum_{m=1}^{N_R}X_{m,mode}(a_m^R+b_m^R) \tag{3.30}$$

Where $X_{m,mode}$ is the ***inner cross product*** of between the mode m of waveguide P and the mode $mode$ of the waveguide R.

This can be calculated for all the modes $mode=1,2,\ldots N_P$.

Similarly using the magnetic field boundary conditions, we have:

$$\int\int_{A_R}(\hat{z}\times\vec{H}^P).\vec{E}^R_{mode}\hat{z}dS=\int\int_{A_R}(\hat{z}\times\vec{H}^R).\vec{E}^R_{mode}\hat{z}dS=Q^R_{mode}(b^R_{mode}-a^R_{mode}) \tag{3.31}$$

$\Rightarrow$

$$\sum_{n=1}^{N_P}X_{mode,n}(a_n^P-b_n^P)=Q^R_{mode}(b^R_{mode}-a^R_{mode}) \tag{3.32}$$

This can be done for all modes $mode = 1, 2, \ldots N_R$.

In matrix form, equations can be written as:

$$Q_P(a_P + b_P) = X^t(a_R + b_R) \tag{3.33}$$

$$Q_R(b_R - a_R) = X(a_P - b_P) \tag{3.34}$$

The superscript t denotes transverse component of the fields. Where, Q_P and Q_R are diagonal matrices of order $N_P \times N_P$ and $N_R \times N_R$ respectively. From definition of the inner cross product X, we know that the dimensions for X should be $N_R \times N_P$. From the coefficients a_P and a_R, b_P and b_R can be calculated using the Generalised Scattering Matrix (GSM).

$$\begin{bmatrix} b_p \\ b_s \end{bmatrix} = \begin{bmatrix} S_{PP} & S_{PR} \\ S_{RP} & S_{RR} \end{bmatrix} \begin{bmatrix} a_p \\ a_s \end{bmatrix} \tag{3.35}$$

The entries of the GSM matrix can be found by the following,

$$GSM = \begin{bmatrix} Q_P^{-1}X^tFX - I_P & Q_P^{-1}X^tFQ_R \\ FX & FQ_R - I_R \end{bmatrix} \tag{3.36}$$

Here I_P and I_R are identity matrices of order $N_P \times N_P$ and $N_R \times N_R$ respectively and F is given by:

$$F = 2(Q_R + XQ_P^{-1}X^t)^{-1} \tag{3.37}$$

Note: The projections here mentioned are Galerkin's projections. A Galerkin's projection is made with the same type of quantity. Therefore, for boundary condition of electric field, for $\hat{z} \times E$, a magnetic field is projected and for boundary condition of magnetic field, for $\hat{z} \times H$, an electric field is projected.

3.3.4. Formulation of the Inner Cross-Product X

First of all the transverse (without the phase term dependent on z) fields can be written as:

TE:

$$\vec{E}_n = K_{mnTE}^{\frac{1}{2}} Z_{mnTE}^{\frac{1}{2}} \vec{\Phi}_{En} = K_{mnTE}^{\frac{1}{2}} Z_{mnTE}^{\frac{1}{2}} \nabla_t \Phi_n \times \hat{z} \tag{3.38}$$

$$\vec{H}_n = K_{mnTE}^{\frac{1}{2}} Y_{mnTE}^{\frac{1}{2}} \vec{\Phi}_{Hn} = K_{mnTE}^{\frac{1}{2}} Y_{mnTE}^{\frac{1}{2}} \nabla_t \Phi_n \tag{3.39}$$

$$\vec{E}_{zn} = 0\hat{z} \tag{3.40}$$

$$\vec{H}_{zn} = -K_{mnTE}^{\frac{1}{2}} Y_{mnTE}^{\frac{1}{2}} \frac{\beta_c^2}{\beta_z} \Phi_n \hat{z} \tag{3.41}$$

Here, Φ_n is a scalar function like the potential function described in chapter 2 without the phase term containing z. The Φ_ns are the solution to the differential equations of the form $\Delta_t \Phi_n + \beta_c^2 \Phi_n = 0$.

The expression for the scalar Φ function is given as:

$$\Phi_{TE} = J_m(\beta_\rho \rho)\cos(m\phi) \tag{3.42}$$

TM:

$$\vec{H}_n = K_{mnTM}^{\frac{1}{2}} Y_{mnTM}^{\frac{1}{2}} \vec{\Phi}_{Hn} = K_{mnTM}^{\frac{1}{2}} Y_{mnTM}^{\frac{1}{2}} \nabla_t \Phi_n \times \hat{z} \tag{3.43}$$

$$\vec{E}_n = K_{mnTM}^{\frac{1}{2}} Z_{mnTM}^{\frac{1}{2}} \vec{\Phi}_{En} = K_{mnTM}^{\frac{1}{2}} Z_{mnTM}^{\frac{1}{2}} \nabla_t \Phi_n \tag{3.44}$$

$$\vec{H}_{zn} = 0\hat{z} \tag{3.45}$$

$$\vec{E}_{zn} = -K_{mnTM}^{\frac{1}{2}} Z_{mnTM}^{\frac{1}{2}} \frac{\beta_c^2}{\beta_z} \Phi_n \hat{z} \tag{3.46}$$

The expression for the scalar Φ function is given as:

$$\Phi_{TM} = J_m(\beta_\rho \rho)\cos(m\phi) \tag{3.47}$$

The Z and Y are different for TE and TM (Expressions are given in chapter 2).

Using these expressions for the inner cross product, we have:

$$X = \int\int_{A_R} (\vec{E}_{rm,rn}^R \times \vec{H}_{pm,pn}^P).\hat{z}dS = (K_{rm,rn}^R)^{\frac{1}{2}} (Z_{rm,rn}^R)^{\frac{1}{2}} \bar{X}_{(rm,rn)->(pm,pn)} (Y_{pm,pn}^P)^{\frac{1}{2}} (K_{pm,pn}^P)^{\frac{1}{2}} \tag{3.48}$$

Where $\bar{X}$ is defined as:

$$\bar{X} = \int\int_{A_R} (\vec{\Phi}_{Em}^R \times \vec{\Phi}_{Hn}^P).\hat{z}dS = \int\int_{A_R} (\vec{\Phi}_{Em}^R.\vec{\Phi}_{En}^P)dS = \int\int_{A_R} (\vec{\Phi}_{Hm}^R.\vec{\Phi}_{Hn}^P)dS \tag{3.49}$$

Therefore, the matrix $\bar{X}$ is frequency independent. It can be solved with surface integrals over the domain A_R. The simplifications to this integral can be found by the following formulae:

TE mode in P and TE mode in R Following equations (3.39) and (3.49)

$$\bar{X} = \int\int_{A_R} (\vec{\Phi}^R_{Hm}.\vec{\Phi}^P_{Hn})dS = \int\int_{A_R} \nabla_t \Phi_R.\nabla_t \Phi_P dS \tag{3.50}$$

TE mode in P and TM mode in R Following equations (3.39), (3.43) and (3.49)

$$\bar{X} = \int\int_{A_R} (\vec{\Phi}^R_{Em} \times \vec{\Phi}^P_{Hn}).\hat{z}dS = \int\int_{A_R} (\nabla_t \Phi_R \times \nabla_t \Phi_P).\hat{z}dS \tag{3.51}$$

TM mode in P and TE mode in R Following equations (3.38), (3.44) and (3.49)

$$\bar{X} = \int\int_{A_R} (\vec{\Phi}^R_{Em} \times \vec{\Phi}^P_{Hn}).\hat{z}dS = \int\int_{A_R} (\nabla_t \Phi_P \times \nabla_t \Phi_R).\hat{z}dS \tag{3.52}$$

TM mode in P and TM mode in R

Following equations (3.44) and (3.30)

$$\bar{X} = \int\int_{A_R} (\vec{\Phi}^R_{Em}.\vec{\Phi}^P_{En})dS = \int\int_{A_R} \nabla_t \Phi_R.\nabla_t \Phi_P dS \tag{3.53}$$

3.3.5. Formulation of Inner Cross Product using Normalized Field Equations

The potential function used in the previous formulation wasn't normalized. There is another way to visualise the problem with normalized field equations where the potentials can be written as:

$$\Psi = (N_{TE/TM}) J_m(\beta_\rho \rho)\cos(m\phi) \tag{3.54}$$

The potential function is a solution to the differential equation $\Delta_t \Psi_n + \beta_\rho^2 \Psi_n = 0$ with the boundary condition that:

$$\int\int_S |\nabla_t \Psi_n|^2 dS = 1 \tag{3.55}$$

Applying the boundary condition of orthogonality, we can find the normalization factor. The above equation 3.55 can be rewritten as:

$$(N_{TE/TM})^2 \int\int_{A_{area}} \left[\frac{m^2}{\rho^2} J_m^2(\beta_{\rho(m,n)}\rho)\sin^2(m\phi) + \beta^2_{\rho(m,n)} J'^2_m(\beta_{\rho(m,n)}\rho)\cos^2(m\phi)\right]\rho d\rho d\phi = 1 \tag{3.56}$$

Here, the integral exactly looks like the integral that appeared in the normalization factor Q in section 3.2.1 equation (3.9). Therefore, the solution as per equation (3.20) is:

$$\int\int_S |\nabla_t \Psi_n|^2 dS = (N_{TE/TM})^2 \frac{\beta^2_{\rho(m,n)}}{4}(I_A + I_C)2\pi \tag{3.57}$$

I_A and I_C are given in the equations 3.16 and 3.18. Using Lommel's integral of equation 3.19, we can further simplify the term $I_A + I_C$ as,

For TE

We know that for TE,

$$J'_m(\beta_\rho r) = 0 \tag{3.58}$$

$\Rightarrow$

Using the Bessel's function properties,

$$J_{m-1}(\beta_\rho r) = J_{m+1}(\beta_\rho r) \tag{3.59}$$

$$J_{m-1}(\beta_\rho r) = \frac{m}{\beta_\rho r} J_m(\beta_\rho r) \tag{3.60}$$

Using these properties, it is found that,

$$I_A + I_C = \frac{1}{2} r^2 \frac{J^2_m(\beta_\rho r)}{(\beta_\rho r)^2} 2((\beta_\rho r)^2 - m^2) = \frac{J^2_m(\beta_\rho r)}{(\beta_\rho)^2}((\beta_\rho r)^2 - m^2) \tag{3.61}$$

Using this on equation 3.57, we have,

$$\int\int_S |\nabla_t \Psi_n|^2 dS = (N_{TE})^2 \frac{\beta^2_{\rho(m,n)}}{4}(I_A + I_C)2\pi = (N_{TE})^2 \frac{\pi}{2} J^2_m(\beta_\rho r)((\beta_\rho r)^2 - m^2) = 1 \tag{3.62}$$

$\Rightarrow$

$$N_{TE} = \frac{\sqrt{\frac{2}{\pi}}}{J_m(\beta_{\rho(m,n)} r)\sqrt{((\beta_{\rho(m,n)} r)^2 - m^2)}} \tag{3.63}$$

The term $\beta_{\rho(m,n)} r$ is just the nth root of the derivative of the mth order Bessel function which is written in chapter 2 as (χ'_{mn})

$$N_{TE} = \frac{\sqrt{\frac{2}{\pi}}}{J_m(\chi'_{mn})\sqrt{(\chi'^2_{mn} - m^2)}} \tag{3.64}$$

For TM

For TM using the property that $J_m(\beta_\rho r) = 0$ and the boundary condition of the normalized power (3.55), it is found that,

$$N_{TM} = \frac{\sqrt{\frac{2}{\pi}}}{J'_m(\chi_{mn})\chi_{mn}} \tag{3.65}$$

The term $\beta_{\rho(m,n)}r$ for TM is just the nth root of the mth order Bessel function which is written in chapter 2 as (χ_{mn})

Using this normalized potential scalar function Ψ, the equations from 3.38 to 3.47 can be rewritten as,

TE:

$$\vec{E}_n = Q^{\frac{1}{2}}_{mnTE} Z^{\frac{1}{2}}_{mnTE} \vec{\Psi}_{En} = Q^{\frac{1}{2}}_{mnTE} Z^{\frac{1}{2}}_{mnTE} \nabla_t \Psi_n \times \hat{z} \tag{3.66}$$

$$\vec{H}_n = Q^{\frac{1}{2}}_{mnTE} Y^{\frac{1}{2}}_{mnTE} \vec{\Psi}_{Hn} = Q^{\frac{1}{2}}_{mnTE} Y^{\frac{1}{2}}_{mnTE} \nabla_t \Psi_n \tag{3.67}$$

$$\vec{E}_{zn} = 0\hat{z} \tag{3.68}$$

$$\vec{H}_{zn} = -Q^{\frac{1}{2}}_{mnTE} Y^{\frac{1}{2}}_{mnTE} \frac{\beta_c^2}{\beta_z} \Psi_n \hat{z} \tag{3.69}$$

The expression for the scalar Ψ function is given as: (As listed in the Appendix of [28])

$$\Psi_{TE} = (N_{TE}) J_m(\beta_\rho \rho) \cos(m\phi) \tag{3.70}$$

TM:

$$\vec{H}_n = Q^{\frac{1}{2}}_{mnTM} Y^{\frac{1}{2}}_{mnTM} \vec{\Psi}_{Hn} = Q^{\frac{1}{2}}_{mnTM} Y^{\frac{1}{2}}_{mnTM} \nabla_t \Psi_n \times \hat{z} \tag{3.71}$$

$$\vec{E}_n = Q_{mnTM}^{\frac{1}{2}} Z_{mnTM}^{\frac{1}{2}} \vec{\Psi}_{En} = Q_{mnTM}^{\frac{1}{2}} Z_{mnTM}^{\frac{1}{2}} \nabla_t \Psi_n \tag{3.72}$$

$$\vec{H}_{zn} = 0\hat{z} \tag{3.73}$$

$$\vec{E}_{zn} = -Q_{mnTM}^{\frac{1}{2}} Z_{mnTM}^{\frac{1}{2}} \frac{\beta_c^2}{\beta_z} \Psi_n \hat{z} \tag{3.74}$$

The expression for the scalar Ψ function is given as: (As listed in the Appendix of [28])

$$\Psi_{TM} = (N_{TM}) J_m(\beta_\rho \rho) \cos(m\phi) \tag{3.75}$$

The difference between equations 3.38 to 3.47 and 3.66 to 3.75 is that the K_{mn} terms are replaced by the normalization constant (conjugate power terms) Q_{mn} and Φ is replaced by Ψ. Here, the potential function Ψ is different for TE and TM.

Using this normalized potentials, the inner product is defined as:

$$X = \int\int_{A_R} (\vec{E}_{rm,rn}^R \times \vec{H}_{pm,pn}^P).\hat{z}dS = (Q_{rm,rn}^R)^{\frac{1}{2}} (Z_{rm,rn}^R)^{\frac{1}{2}} \bar{X_\Psi}_{(rm,rn)->(pm,pn)} (Y_{pm,pn}^P)^{\frac{1}{2}} (Q_{pm,pn}^P)^{\frac{1}{2}} \tag{3.76}$$

Where $\bar{X_\Psi}$ is defined as:

$$\bar{X_\Psi} = \int\int_{A_R} (\vec{\Psi}_{Em}^R \times \vec{\Psi}_{Hn}^P).\hat{z}dS = \int\int_{A_R} (\vec{\Psi}_{Em}^R.\vec{\Psi}_{En}^P)dS = \int\int_{A_R} (\vec{\Psi}_{Hm}^R.\vec{\Psi}_{Hn}^P)dS \tag{3.77}$$

3.3.6. Analytical Formulation of the Inner Cross Product for modes TE, TE and TM, TM combination

The analytical formulation can be done using the same principles mentioned for the normalization constant Q in the previous sub-section. Using equation (3.50), we have:

For TE and TE / For TM and TM

$$\bar{X} = \int\int_{A_R} \nabla_t \Phi_R . \nabla_t \Phi_P dS = \frac{\beta_{\rho(pm,pn)} \beta_{\rho(rm,rn)}}{4} \left[(I_A + I_D)(I_{cos} + I_{sin}) - (I_B + I_C)(I_{cos} - I_{sin}) \right] \tag{3.78}$$

Where pm and pn are the mode numbers for the waveguide P and rm and rn are the mode number for the waveguide R.

Here, to make it simple, pm and rm are kept the same. (In the plots $pm = rm = 1$) to have a simplified analytical solution for the inner cross product.

The integrals mentioned in the equation (3.78) are:

$$I_{sin} = \int_0^{2\pi} sin(pm\phi)sin(rm\phi)d\phi = \pi \quad (pm = rm), = 0, \quad (pm \neq rm) \tag{3.79}$$

$$I_{cos} = \int_0^{2\pi} cos(pm\phi)cos(rm\phi)d\phi = \pi, \quad (pm = rm), = 0, \quad (pm \neq rm) \tag{3.80}$$

$$I_A = \int_0^r J_{pm-1}(\beta_{\rho(pm,pn)}\rho)J_{rm-1}(\beta_{\rho(rm,rn)}\rho)\rho d\rho \tag{3.81}$$

$$I_B = \int_0^r J_{pm-1}(\beta_{\rho(pm,pn)}\rho)J_{rm+1}(\beta_{\rho(rm,rn)}\rho)\rho d\rho \tag{3.82}$$

$$I_C = \int_0^r J_{pm+1}(\beta_{\rho(pm,pn)}\rho)J_{rm-1}(\beta_{\rho(rm,rn)}\rho)\rho d\rho \tag{3.83}$$

$$I_D = \int_0^r J_{pm+1}(\beta_{\rho(pm,pn)}\rho)J_{rm+1}(\beta_{\rho(rm,rn)}\rho)\rho d\rho \tag{3.84}$$

I_A and I_D can be solved with Lommel's integrals [2] and [5].

$$\int_0^r J_\nu(\beta_\nu\rho)J_\nu(\beta_\mu\rho)\rho d\rho = \frac{r}{(\beta_\nu^2 - \beta_\mu^2)}\Big(- \beta_\nu J_{\nu-1}(\beta_\nu r)J_\nu(\beta_\mu r) + \beta_\mu J_\nu(\beta_\nu r)J_{\nu-1}(\beta_\nu r)\Big) \tag{3.85}$$

The Lommel's integral of (3.19) can be used when $pm = rm$ and also $\beta_{\rho(pm,pn)} = \beta_{\rho(rm,rn)}$ and the Lommel's integral of (3.85) can be used when $pm = rm$ but $\beta_{\rho(pm,pn)} \neq \beta_{\rho(rm,rn)}$.

I_B and I_C have complicated analytical solutions involving hyper-geometric functions. However, as when $pm = rm$, in the original expression of equation (3.76), the term with $I_B + I_C$ vanishes because $I_{sin} = I_{cos} = \pi$. Therefore, the inner cross product becomes:

$$\bar{X} = \int\int_{A_R} \nabla_t\Phi_R.\nabla_t\Phi_P dS = \frac{\beta_{\rho(pm,pn)}\beta_{\rho(rm,rn)}}{4}\Big[(I_A + I_D)(I_{cos} + I_{sin})\Big] \tag{3.86}$$

If $pm \neq rm$, both I_{sin} and I_{cos} are 0. Therefore, the inner cross product also becomes zero.

Therefore, for TE/TE and TM/TM combinations, the inner cross product is given by the table 3.1 .

conditions	sub conditions	$\bar{X}$
$pm = rm$	$\beta_{\rho(pm,pn)} = \beta_{\rho(rm,rn)}$	$\frac{\beta_{\rho(pm,pn)}\beta_{\rho(rm,rn)}}{4}\Big[(I_A + I_D)(I_{cos} + I_{sin})\Big]$, I_A, I_D from eq (3.19)
	$\beta_{\rho(pm,pn)} \neq \beta_{\rho(rm,rn)}$	$\frac{\beta_{\rho(pm,pn)}\beta_{\rho(rm,rn)}}{4}\Big[(I_A + I_D)(I_{cos} + I_{sin})\Big]$, I_A, I_D from eq (3.85)
$pm \neq rm$		0

Table 3.1: Inner Cross Product in case of TE/TE and TM/TM mode configuration.

It suggests that there is no coupling in case of $TE_{1,n}$, $TE_{2,n}$, $TE_{3,n}$ and so on. same holds for TM modes.

For TM in R(smaller waveguide) and TE (larger waveguide)

This is a combination where the smaller waveguide (R) and the larger waveguide (P) have a TM and a TE mode respectively. Then, the inner cross product can be found from appendix A, which is zero.

For TE in R(smaller waveguide) and TM (larger waveguide)

In this case, the inner cross product becomes,

$$\bar{X} = \int\int_{A_R} ((-\nabla_t \Phi_R \times \hat{z}) \times (\nabla_t \Phi_P \times \hat{z})).\hat{z}dS = \int\int_{A_R} (\nabla_t \Phi_P \times \nabla_t \Phi_R).\hat{z} \tag{3.87}$$

Which looks like the previous case (TM in R and TE in P) in appendix A. In this case also the I_{12} and I_{22} terms (These terms are defined in appendix A) are zero because of the integrals $\int_0^{2\pi} \cos(rm\phi)\sin(pm\phi)d\phi = 0$ and $\int_0^{2\pi} \cos(pm\phi)\sin(rm\phi)d\phi = 0$. However, as the integral is over A_R (Area of cross section for R or the smaller waveguide) and the waveguide having TM mode is the large waveguide, equation (2.32) doesn't hold. So, $J_{pm}(\beta_{\rho(pm,pn)}rr) \neq 0$. However, as only I_{12} and I_{22} are zero, the inner cross product is zero.

The difference between these two configurations (TM in R and TE in P/TE in R and TM in p) is that the radial integrals I_{11} and I_{21} are zero for the former because the integration domain is the smaller waveguide cross-section and for the same reason, these integrals are non-zero for the later case.

So, for both TM/TE and TE/TM modes, the inner cross product is zero.

3.4. Convergence of Mode Matching Technique

Convergence of the mode matching technique is studied by adding higher order modes on the input section keeping the ratio of the number of modes as the aspect ratio (in this case the ratio of the areas of the two different cross-sections for the two waveguides).

Example 1

The first test was done when the radii of waveguide P and R are almost the same. ($r_p = 2[cm], \quad r_r = 1.9[cm]$). As the radii are almost the same the convergence study was carried out by fixing the ratio of number of modes as one and increasing the number of modes. The results are shown in figure 3.4. The frequency was chosen to be a frequency with which all modes that are included are propagating modes on both waveguides. The plot shows the various S-parameters of the fundamental mode only.

The figure 3.4 suggests that the convergence of results occurs when we include higher order modes till 25 or more on both waveguides. The relative convergence criterion is explained in [13] and [21]. The relative convergence criterion is important in convergence study. Only increasing the number of modes doesn't help in increasing accuracy unless the ratio of number of modes on both the sides is appropriate.

Example 2

The same convergence study is carried out but with a different set of radii than in example 1. The radii were chosen to be $r_p = 2[cm]$ and $r_r = 1[cm]$. Therefore, the ratio of the areas become $\frac{\pi r_p^2}{\pi r_r^2} = 4$. The results are shown in figure 3.5. Here, the modes on the x axes are the modes represented by the modes in the smaller waveguide R. The larger waveguide P has four times more modes than the smaller waveguide R. It is seen that after 10 modes in R (40 modes in P), the S-parameter values are converging.

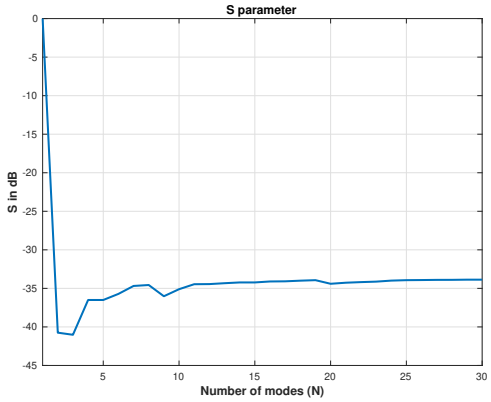

(a) S_{pp} of TE_{11} mode on each side with different number of modes on each waveguide

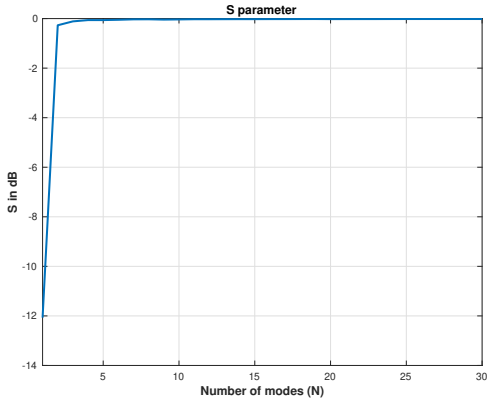

(b) S_{pr} of TE_{11} mode on each side with different number of modes on each waveguide

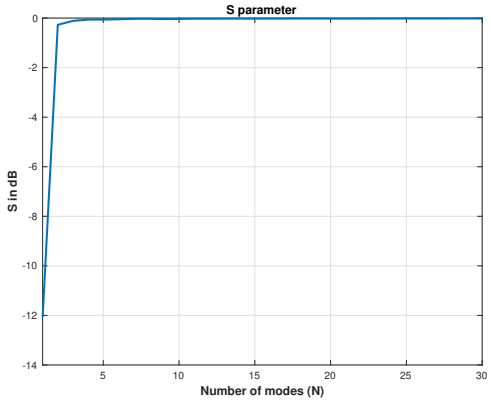

(c) S_{rp} of TE_{11} mode on each side with different number of modes on each waveguide

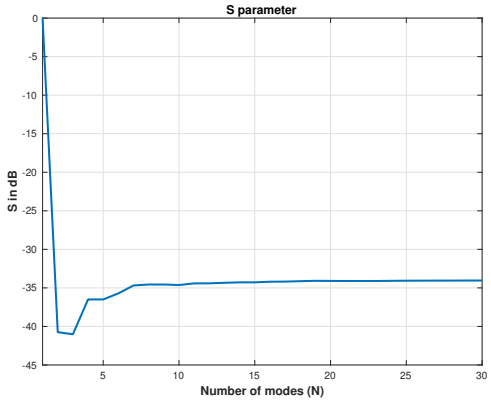

(d) S_{rr} of TE_{11} mode on each side with different number of modes on each waveguide

Figure 3.4: Convergence study when radii ratio is approximately 1.

The convergence for example 1 can be explained in the below figure 3.6 where S_{pp} is plotted for TE_{11} mode. Better results are seen when higher order modes are considered.

3.4.1. FEKO/CST Simulations and Comparison

Example 1 stated above was simulated in both FEKO (Method of Moments solver with Surface equivalence principle) and CST (time domain solver). The results are shown in figure 3.7 along with the results of the MATLAB model using the mode matching techniques mentioned above. Here, the number of modes on each waveguide is 20. The variation of phase is shown in figure 3.8.

3.4.2. Observations from the comparison of MM and FEKO/CST simulations and Conclusions

The plots shown in figure 3.7 are plotted from the frequency where the fundamental mode (TE_{11}) is a propagating mode on both the waveguides. It can be seen that at 9.5 GHz and at 16.5 GHz, there is a discontinuity in the S parameter plots from the commercial tools like FEKO and CST MWS(Microwave Studio). The reason why this discontinuity is not observed in the MATLAB implementation of Mode Matching Technique is that the modes corresponding to those cut-off frequencies have no coupling with the TE_{11} mode. In other words, the modes TE_{01}, TM_{11}, TE_{02}, TM_{12} and so on are orthogonal to the mode TE_{11}. This can be observed in the inner cross product matrix formulation. The integral of

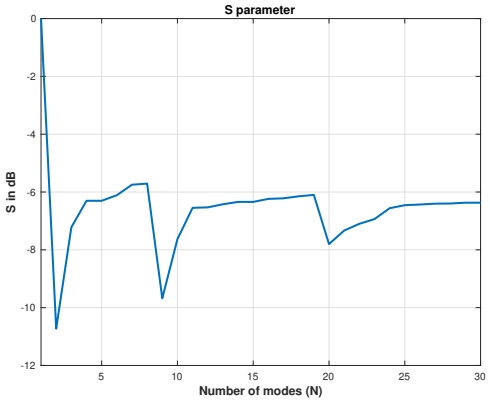

(a) S_{pp} of TE_{11} mode on each side with different number of modes on each waveguide

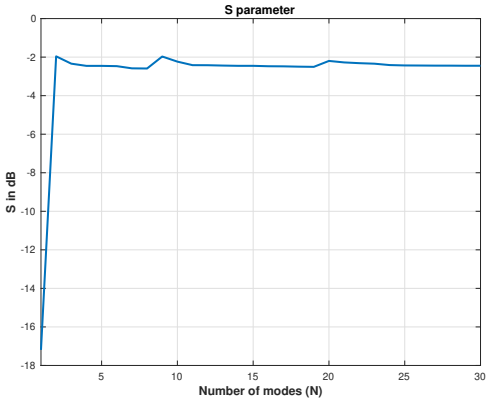

(b) S_{pr} of TE_{11} mode on each side with different number of modes on each waveguide

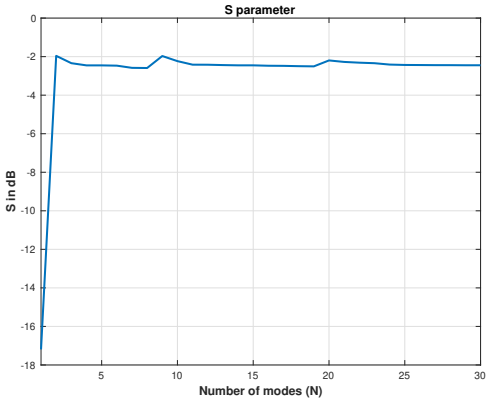

(c) S_{rp} of TE_{11} mode on each side with different number of modes on each waveguide

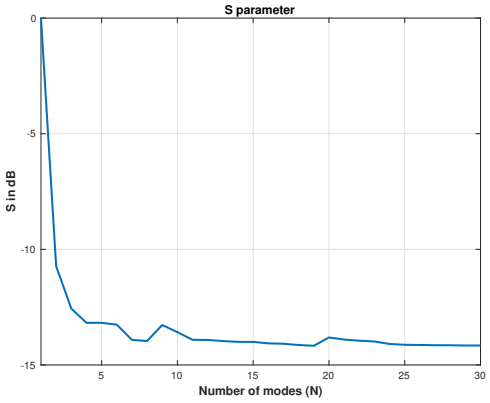

(d) S_{rr} of TE_{11} mode on each side with different number of modes on each waveguide

Figure 3.5: Convergence study when radii ratio is 2.

the inner cross product becomes zero because these TE modes have different azimuthal variations ($pm \neq rm$ case in table 3.1). This is a result of the integrals I_{cos} and I_{sin}. However, in the results that are obtained from Feko and CST MWS, it suggests that there is coupling between these TE modes with TE_{11} mode. This is a result of the discretization performed in Feko with MoM solver (triangular mesh) and similarly in CST with time domain method. As the discretization of the geometry doesn't make the aperture a smooth circle, the coupling of these modes are observed with respect to TE_{11}. To investigate this in more detail, 3 simulation results are plotted from FEKO with varying discretization length for the triangular mesh elements.

The results shown in figure 3.9 are the reflection coefficients of the TE_{11} mode with respect to TM_{11} mode. TM_{11} and TE_{01} have the same cut-off frequencies. It can be seen that with finer meshing, the value decreases. A coarse mesh also suggests that the values are below -40 dB. However, with mode matching implementation with analytical formulation, we can see that the values of reflection coefficients are around -200 dB. Apart from those discontinuities, the plots with MM and the plots from FEKO/CST MWS are very similar to each other. As, the radii in this case are also almost same (difference of the radii is one mili-meter which is electrically small), the transmission coefficients due to the coupling on both waveguides should be one (zero in dB scale) for TE_{11} mode after the cut-off frequency. It is also observed on the plots of the Mode Matching implementation.

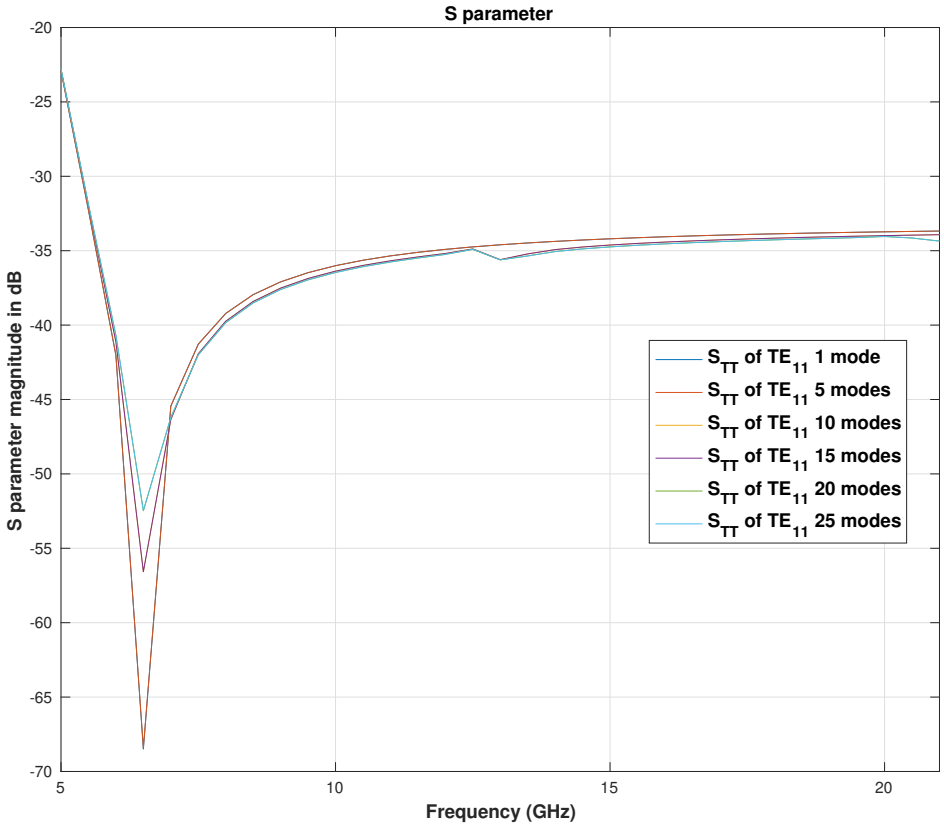

Figure 3.6: S_{pp} for TE_{11} modes with different number of modes on each waveguide using MM technique. Ratio of number of modes on each side is kept as 1.

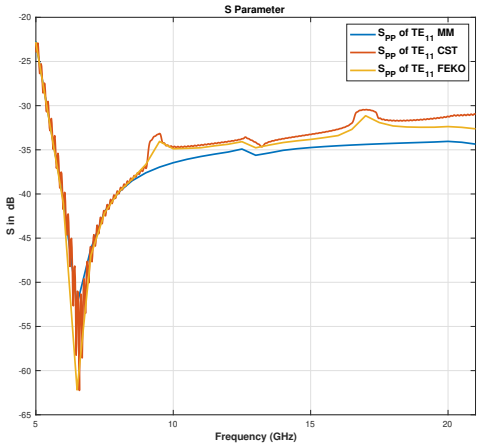

(a) S_{pp} of TE_{11} FEKO/CST vs MM

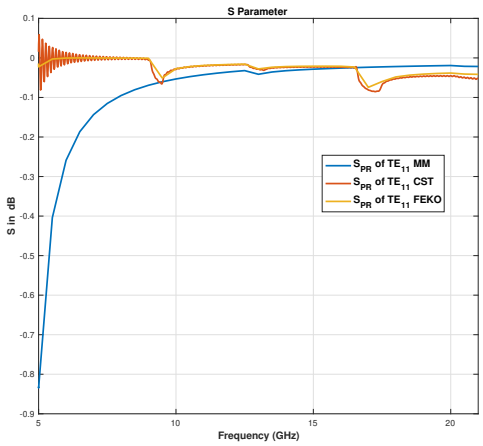

(b) S_{pr} of TE_{11} FEKO/CST vs MM

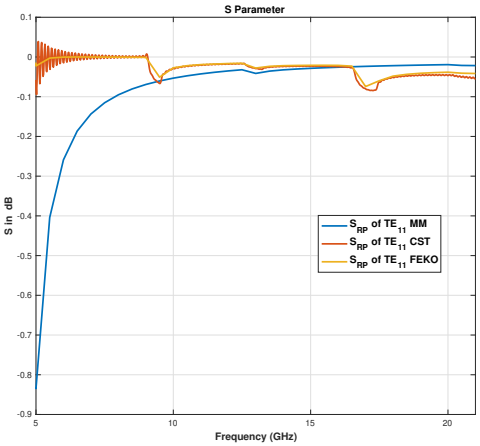

(c) S_{rp} of TE_{11} FEKO/CST vs MM

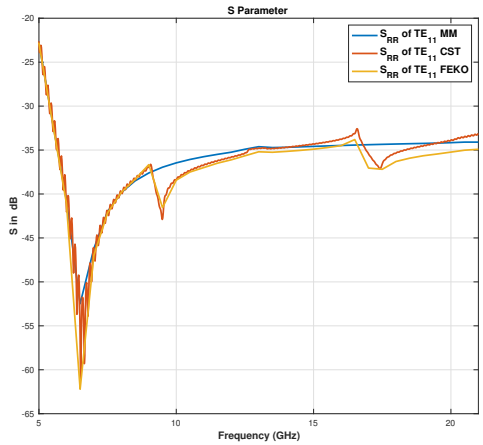

(d) S_{rr} of TE_{11} FEKO/CST vs MM

Figure 3.7: S-parameters for TE_{11} mode - FEKO/CST vs MM. 20 modes added for analysis on each waveguide

3.5. Conclusions

In this chapter a waveguide junction problem was studied with cricular cross section waveguides with the mode matching technique (MM). Analytical expressions have been derived for the general scattering matrix (GSM) for the case of a circular to circular cross section waveguide transition. The resulting analytical expressions have been implemented in MATLAB to find the general scattering matrix of the junction problem and it was verified with numerical solutions available in commercial tools like FRKO and CST. The MATLAB results of elements of the scattering matrix have good agreement with the FEKO and CST results. It was found that higher order modes have to be included in the analysis for the formulation of the GSM to get more accuracy for the S-parameters (elements of the GSM).

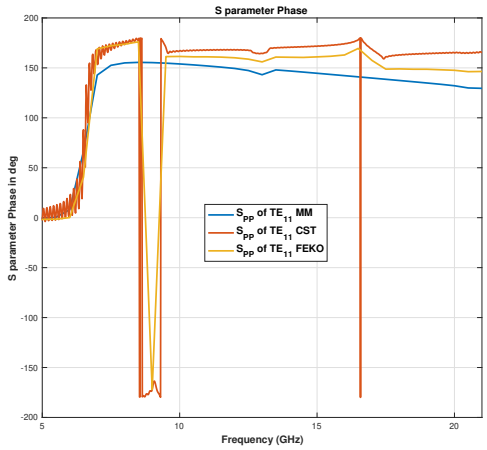

(a) phase of S_{pp} of TE_{11} FEKO/CST vs MM

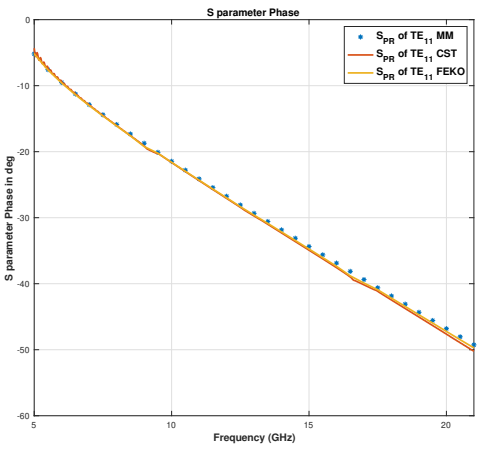

(b) phase of S_{pr} of TE_{11} FEKO/CST vs MM

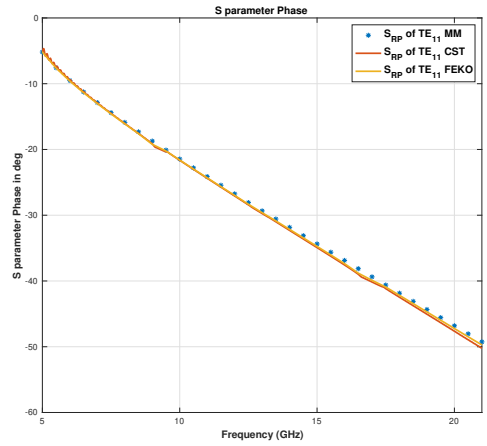

(c) phase of S_{rp} of TE_{11} FEKO/CST vs MM

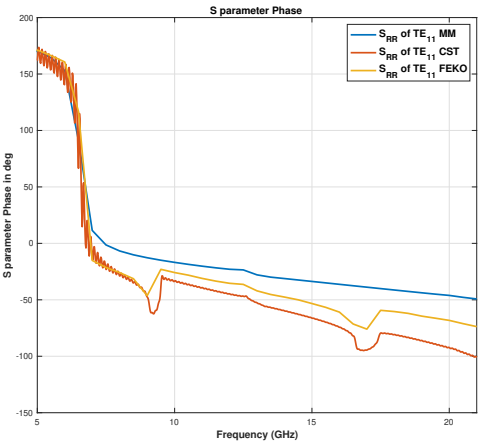

(d) phase of S_{rr} of TE_{11} FEKO/CST vs MM

Figure 3.8: S parameter phase for TE_{11} mode - FEKO vs CST vs MM. 20 modes added for the analysis on each waveguide

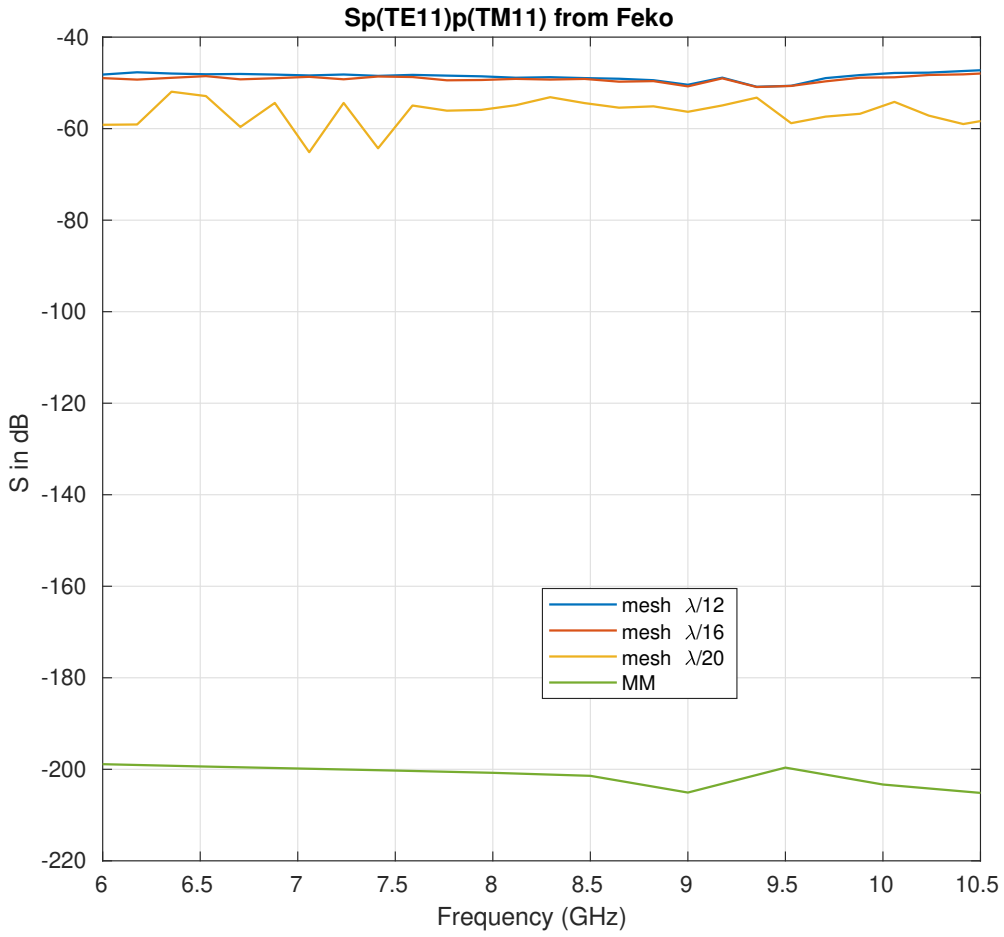

Figure 3.9: $Sp(TE_{11})p(TM_{11})$

4

Cascaded Circular Cross-Section Waveguides with Mode Matching Technique

4.1. Problem description

In the previous chapter, only two waveguides were studied with one GSM matrix. This chapter covers the formulation of the scattering matrix when a number of waveguides are connected in a row. As in the previous section the GSM was found at $z = 0$, the phase term of $e^{-j\beta_z l}$ didn't come into picture. As z dependence doesn't affect the magnitude of S parameters, it was ignored. However, in a cascaded structure, the phase information is important as the discontinuities are at different points over the z-axis. As described in [31], we first consider a simple structure with three waveguides. The two waveguides remain the same as in the previous chapter and one bigger waveguide T is cascaded after the waveguide P on the negative z axis. Therefore, the port on the outer surface of P is now translated to the outer surface of T. The figure 4.1 shows the Geometry and figure 4.2 shows the circuit structure with GSM matrices of each junction. Figure 4.3 shows the equivalent circuit representation with one equivalent GSM.

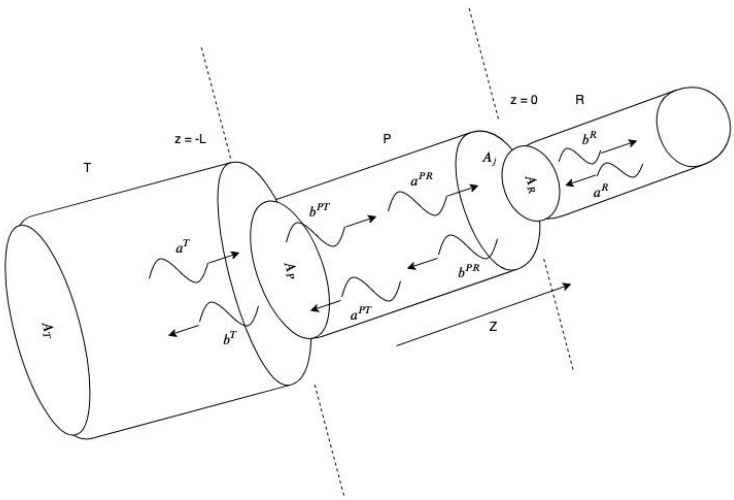

Figure 4.1: 3 waveguides configuration. 2 discontinuities.

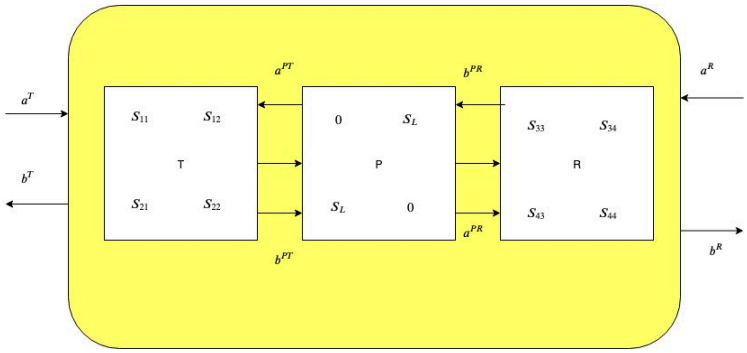

Figure 4.2: 3 waveguides cct configuration. 2 discontinuities.

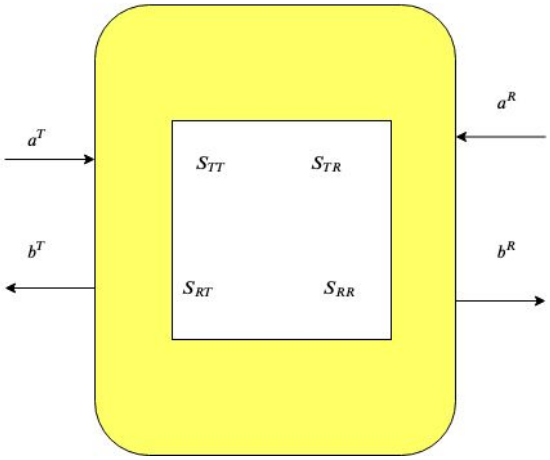

Figure 4.3: 3 waveguides equivalent cct configuration. 2 discontinuities.

4.2. Formulation of GSM

Based on section 3.1.3, we can write the matrix form equations for all the three regions as:

$$\begin{bmatrix} b_T \\ b_{PT} \end{bmatrix} = \begin{bmatrix} S_{11} & S_{12} \\ S_{21} & S_{22} \end{bmatrix} \begin{bmatrix} a_T \\ a_{PT} \end{bmatrix} \tag{4.1}$$

,

$$\begin{bmatrix} a_{PT} \\ a_{PR} \end{bmatrix} = \begin{bmatrix} 0 & S_L \\ S_L & 0 \end{bmatrix} \begin{bmatrix} b_{PT} \\ b_{PR} \end{bmatrix} \tag{4.2}$$

And,

$$\begin{bmatrix} b_{PR} \\ b_R \end{bmatrix} = \begin{bmatrix} S_{33} & S_{34} \\ S_{43} & S_{44} \end{bmatrix} \begin{bmatrix} a_{PR} \\ a_R \end{bmatrix} \tag{4.3}$$

Equations 4.1 and 4.2 yield,

$$b_T = S_{11}a_T + S_{12}S_L b_{PR} \tag{4.4}$$

$$b_{PT} = S_{21}a_T + S_{22}S_L b_{PR} \tag{4.5}$$

Equations 4.2 and 4.3 yield,

$$b_{PR} = S_{33}S_L b_P + S_{34}a_R \tag{4.6}$$

$$b_R = S_{43}S_L b_{PT} + S_{44}a_R \tag{4.7}$$

Solving 4.5 and 4.6 we have,

$$b_{PT} = U_1(S_{21}a_T + S_{22}S_L S_{34}a_R) \tag{4.8}$$

$$b_{PR} = U_2(S_{33}S_L S_{21}a_T + S_{44}a_R) \tag{4.9}$$

Where,

$$U_1 = (I - S_{22}S_L S_{33}S_L)^{-1} \tag{4.10}$$

And,

$$U_2 = (I - S_{33}S_L S_{22}S_L)^{-1} \tag{4.11}$$

Using 4.8 and 4.9 on 4.4 and 4.7, we have,

$$b_T = (s_{11} + S_{12}S_L U_2 S_{33}S_L S_{21})a_T + S_{12}S_L U_2 S_{34}a_R \tag{4.12}$$

$$b_R = (s_{44} + S_{43}S_L U_1 S_{22}S_L S_{34})a_R + S_{43}S_L U_1 S_{21}a_T \tag{4.13}$$

Therefore GSM is given by,

$$\begin{bmatrix} S_{TT} & S_{TR} \\ S_{RT} & S_{RR} \end{bmatrix} = \begin{bmatrix} s_{11} + S_{12}S_L U_2 S_{33}S_L S_{21} & S_{12}S_L U_2 S_{34} \\ S_{43}S_L U_1 S_{21} & s_{44} + S_{43}S_L U_1 S_{22}S_L S_{34} \end{bmatrix} \tag{4.14}$$

Here, S_L is a diagonal matrix with elements which are phase terms which depend on z and the wavenumber β_z. Each diagonal element is for each mode.

$$S_L = \begin{bmatrix} e^{-j\beta_{z1}L} & 0 & 0 & 0 & . & . & 0 \\ 0 & e^{-j\beta_{z2}L} & 0 & 0 & . & . & 0 \\ 0 & 0 & e^{-j\beta_{z3}L} & 0 & . & . & 0 \\ . & . & . & . & . & . & . \\ . & . & . & . & . & . & . \\ . & . & . & . & . & . & . \\ 0 & 0 & . & . & . & . & e^{-j\beta_{zN}L} \end{bmatrix} \tag{4.15}$$

Here β_{zi} is the wavenumber for the mode i.

4.2.1. Convergence with three waveguide structure

The waveguide structure that was simulated in MATLAB and Feko is shown in figure 4.4. The radius of the three waveguides are (rr = 1.93 [cm], rp = 2.03 [cm], rt = 2.13 [cm]). The waveguide length of the R waveguide in between the P and T is two centi-meter. The height of the cylinders R and T is also one mili-meter.

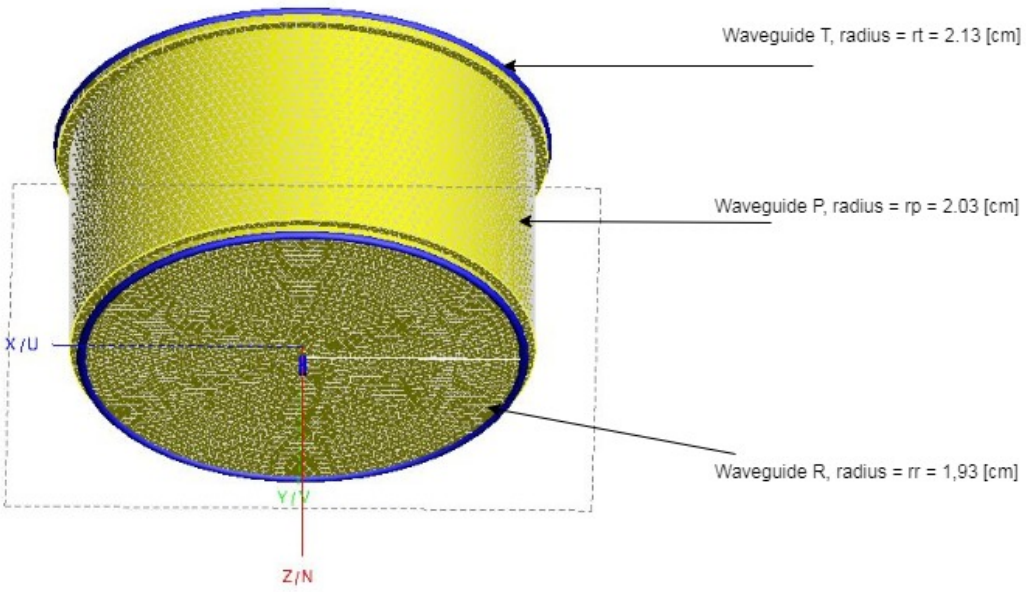

Figure 4.4: 3 waveguides geometry used for simulation.

It is seen that with almost 20 modes on each waveguide, the S-parameter is converging at the point of minimum reflection. However, for all other frequency points, convergence is achieved even with a very few number of modes like five. It also can be seen that the matrix equations that different number of modes can be used in different waveguides along the z-axis. This is useful when we have a large number of waveguides with varying cross-sections. This is shown later with a five waveguides cascade structure.

4.2.2. FEKO/CST simulation and comparison

The structure in figure 4.4 is simulated on Feko (MoM solver / Surface Equivalence Principle) and CST (Time domain solver) and the results are shown in figure 4.6 where the length of the P waveguide

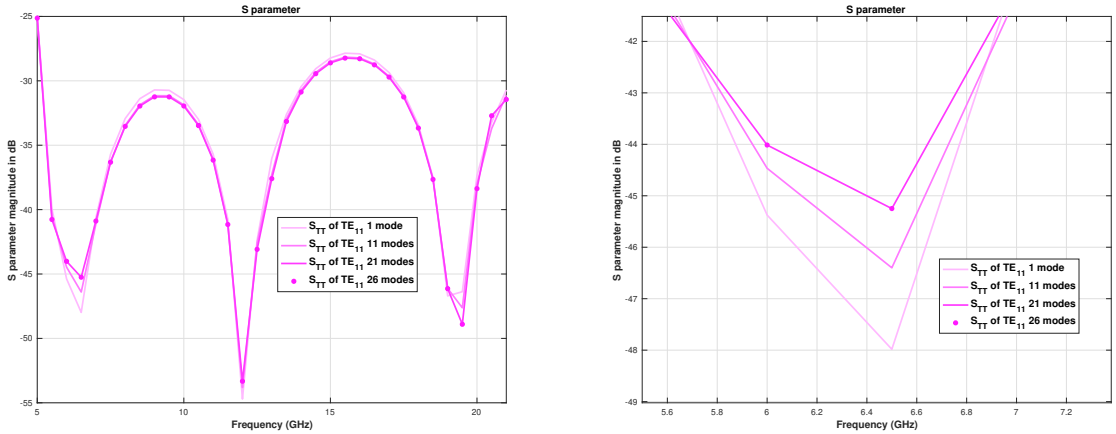

(a) S_{TT} of TE_{11}

(b) S_{TT} of TE_{11} zoomed in

Figure 4.5: S_{TT} of TE_{11} mode using MM Technique with 3 circular cross-section waveguide when the height of the cylinder P is 2 [cm].

$L = 2 \quad [cm]$. The frequency axis in the case of CST simulation has one 1001 points which is very high than the MM and FEKO simulations (35 points). This is because of the fact that in CST, a time domain solver was used. Therefore, the CST curves have more detailed pattern than the MM and FEKO simulations.

The phase comparison is shown in figure 4.7.

In all these simulations with Mode Matching Technique, the height of the first and last waveguide in the structure is also considered [21]. Therefore, the General scattering matrix is given as,

$$S = \begin{bmatrix} S_{LT} & 0 \\ 0 & S_{LR} \end{bmatrix} \begin{bmatrix} S_{TT} & S_{TR} \\ S_{RT} & S_{RR} \end{bmatrix} \begin{bmatrix} S_{LT} & 0 \\ 0 & S_{LR} \end{bmatrix} \tag{4.16}$$

Where, S_{LT} is given as,

$$S_{LT} = \begin{bmatrix} e^{-j\beta_{zT1}L_T} & 0 & 0 & 0 & . & . & 0 \\ 0 & e^{-j\beta_{zT2}L_T} & 0 & 0 & . & . & 0 \\ 0 & 0 & e^{-j\beta_{zT3}L_T} & 0 & . & . & 0 \\ . & . & . & . & . & . & . \\ . & . & . & . & . & . & . \\ . & . & . & . & . & . & . \\ 0 & 0 & . & . & . & . & e^{-j\beta_{zTN}L_T} \end{bmatrix} \tag{4.17}$$

Here,β_{zTi} is the wavenumber for the mode i in waveguide T. L_T is the height of the cylinder T.

And, S_{LR} is given as,

$$S_{LR} = \begin{bmatrix} e^{-j\beta_{zR1}L_R} & 0 & 0 & 0 & . & . & 0 \\ 0 & e^{-j\beta_{zR2}L_R} & 0 & 0 & . & . & 0 \\ 0 & 0 & e^{-j\beta_{zT3}L_R} & 0 & . & . & 0 \\ . & . & . & . & . & . & . \\ . & . & . & . & . & . & . \\ . & . & . & . & . & . & . \\ 0 & 0 & . & . & . & . & e^{-j\beta_{zRN}L_R} \end{bmatrix} \tag{4.18}$$

Here,β_{zRi} is the wavenumber for the mode i in waveguide R.L_R is the height of the cylinder R.

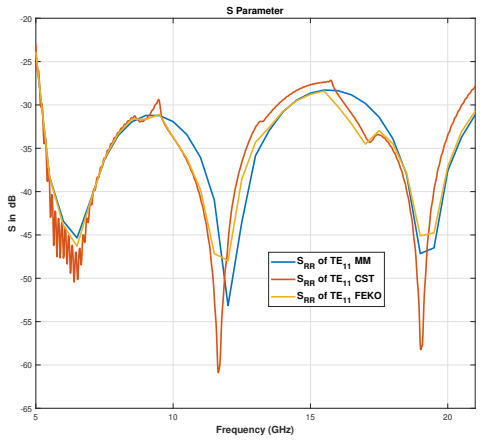

(a) S_{TT} of TE_{11} Feko vs MM

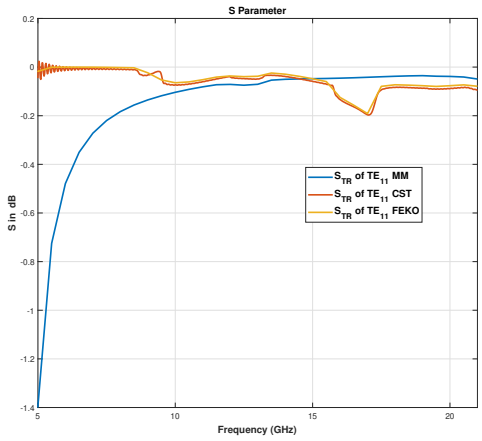

(b) S_{TR} of TE_{11} Feko vs MM

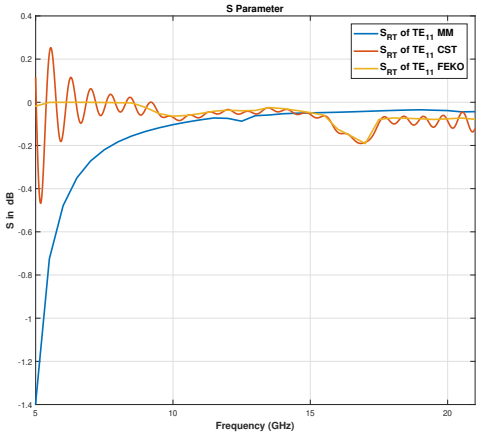

(c) S_{RT} of TE_{11} Feko vs MM

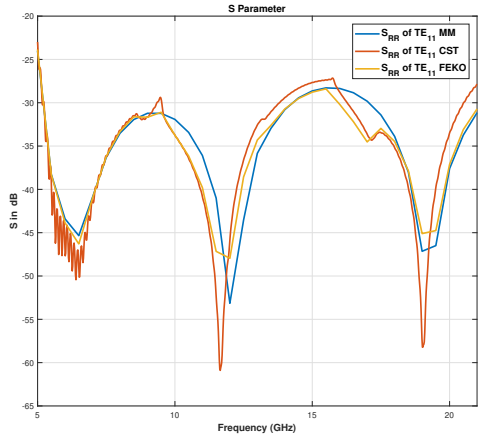

(d) S_{RR} of TE_{11} Feko vs MM

Figure 4.6: S parameters for TE_{11} mode - Feko vs MM. 5 modes active on each waveguide when length of the P waveguide is 2 cm.

4.3. Cascade of more than 3 elements

The above method is iterated until the desired configuration is simulated. The length of the 3rd waveguide is considered as a bridge (The new S_L is found from that length) and on the two sides there are 2 junctions with well defined GSMs.

The algorithm is given below at algorithm 1.

4.3.1. FEKO/CST simulations and comparison

The following figure 4.8 with 5 circular waveguides was simulated on FEKO and CST and simulated in MATLAB with the Mode Matching technique. The results are shown below in figure 4.9 and 4.10.

In this case, the 5 waveguides were simulated with 19, 23, 24, 25 and 28 modes respectively. As the maximum frequency in the plot was 21 GHz, the number of modes were decided based on the cut

Initialization;
if *Number of Junctions* $(J == 2)$ **then**

$$GSM = GSM2(R1, R2);$$

$$Return(GSM)$$

else
if *J == 3* **then**

$$GSM1 = GSM(R1, R2);$$

$$GSM2 = GSM(R2, R3);$$

$$Sl = SL(R2);$$

$$GSM = GSM_{cascade}(GSM1, GSM2, Sl);$$

$$Return(GSM)$$

else

$$GSM1 = GSM(R1, R2);$$

$$GSM2 = GSM(R2, R3);$$

$$Sl = SL(R2);$$

$$GSM_C = GSM_{cascade}(GSM1, GSM2, Sl);$$

$$m = 3$$

while $m <= J$ **do**

$$GSM1 = GSM(R(m+1), R(m));$$

$$GSM2 = GSM_C;$$

$$Sl = SL(R(m));$$

$$GSM_C = GSM_{cascade}(GSM1, GSM2);$$

$$m = m + 1;$$

end

$$Return(GSM_C)$$

end
end

Algorithm 1: Algorithm to find multi junction GSM

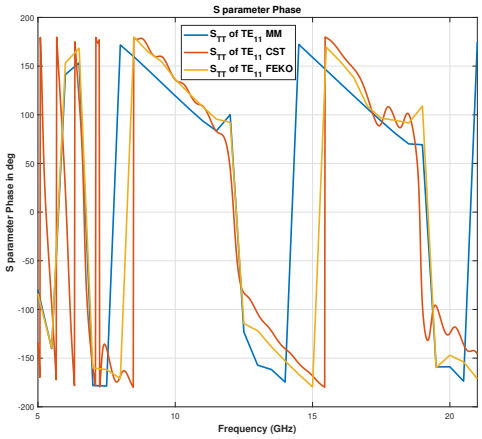

(a) Phase of S_{TT} of TE_{11} Feko vs MM

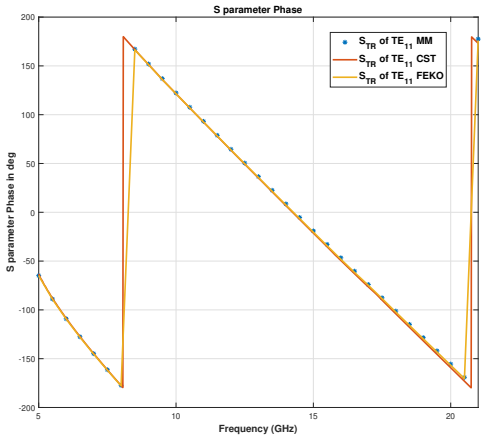

(b) Phase of S_{TR} of TE_{11} Feko vs MM

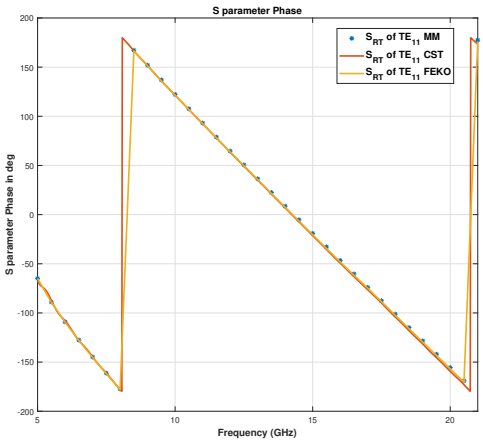

(c) S_{RT} of TE_{11} Feko vs MM

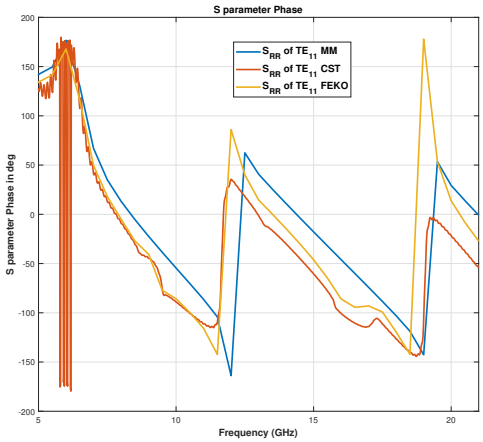

(d) Phase of S_{RR} of TE_{11} Feko vs MM

Figure 4.7: Phase of S parameters for TE_{11} mode - Feko vs MM. 5 modes active on each waveguide when length of the P waveguide is 2 cm.

off frequencies of the modes with respect to the geometry.

4.4. GSM for a conical structure

A conical waveguide with base radius 2 [cm] , top radius 4 [cm] and a height 5 [cm] was simulated with both MM technique in MATLAB and also in FEKO (MoM/SEP solver) and in CST (Time domain solver). With MM technique, the structure is simulated with different number of cylindrical waveguide components.

4.4.1. Feko/CST simulations and comparison

The comparison of S parameters are shown in figure 4.14. With MM technique, the cone structure is simulated with different number of cylindrical waveguide elements. The reflection coefficient are shown for the TE11 mode and the transmission coefficient is shown for TM01 mode. Port T is at the top end (larger radius) and port R is at the base end (smaller radius). The MM plots in figure 4.14 are with 30 cascaded cylindrical waveguide elements with the same axis for propagation(z). The convergence of results from MM technique is shown in figure 4.13 for TE_{11} mode. This figure shows the convergence

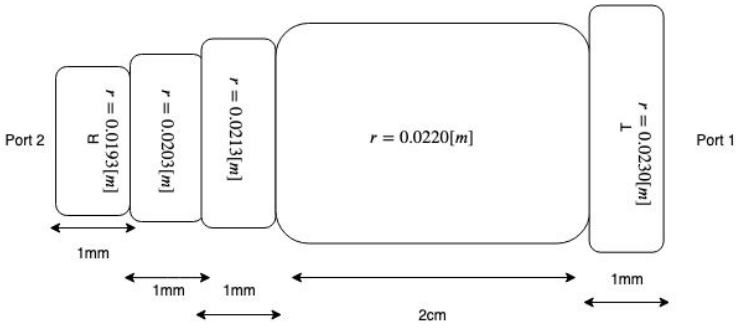

Figure 4.8: Geometry of the 5 waveguide structure with circular waveguides

of S_{RR} when the number of cascaded cylindrical waveguide elements is varied.

4.4.2. Observations

From figure 4.6 and 4.9, it can be seen that the reflection and transmission coefficients from commercial tools like FEKO or CST are very similar to the one from MATLAB with the MM technique. However, at some frequencies the discontinuities observed in FEKO/CST aren't seen in the MM plots. The reason for this is the same as 3.4.2 in chapter three. For the cone structure in figure 4.14, it is seen that the convergence is good when there are more than ten cylindrical waveguide elements for MM technique. They are very similar to the plots obtained from CST and FEKO. The phase of CST plots are not aligned properly because of two reasons. First, the CST model shown in figure 4.12 has two cylindrical waveguides of two mili-meter length at the two ends of the cone. This extra length causes the error. Secondly, the number of modes on the waveguide ports for the CST model is less than the number of modes chosen for FEKO model and for MM. For the second reason, at higher frequencies, phase and magnitude obtained from CST are not well aligned with the plots of MM and FEKO. It is also interesting to notice that the plots from MM technique seem a little shifted in the frequency axis than the results from FEKO and CST. This is due to the fact that in CST and FEKO this is assumed to be a cone with a linear taper where as with MM technique it always remains as a step waveguide junction problem. However, the difference goes down with more number of cylindrical waveguide elements. Furthermore, the length of the conical structure was five centi-meter which is nearly a wavelength of a EM wave with a frequency of five GHz (wavelength is six centi-meter). A EM wave of five GHz frequency comes under the TE_{11} mode (fundamental) bandwidth of the first waveguide in the cascaded waveguide structure. As from the S parameters plot it is seen that the results have good agreement with commercial tool results when the cone structure when the cone is assumed to be a cascaded waveguide structure with at least 10 elements, it can be concluded that, for accuracy, the length of each waveguide section has to be at most of length $\frac{\lambda}{10}$.

4.5. Conclusions

In this chapter, cascaded structures of circular cross section waveguides have been studied. The GSM for the cascaded structure has been derived. The verification was done in a step by step approach. A three waveguide cascaded structure was studied and implemented in MATLAB. The results from MATLAB have been verified with FEKO and CST simulation results. It was found that higher order modes have to be included in the analysis to have more accuracy in the results. The number of modes for analysis on each waveguide can be roughly estimated by the number of propagating modes that waveguide can support at that particular frequency. By having different number of modes for different waveguides in a cascaded junction problem instead of having the same number of modes (based on the biggest waveguide) for every waveguide in the problem saves a lot of computation time. The number of the higher order modes on each waveguide for better accuracy is also verified to be related with the aspect ratio between waveguides (which is the ratio of the areas of the cross sections of the waveguides). A

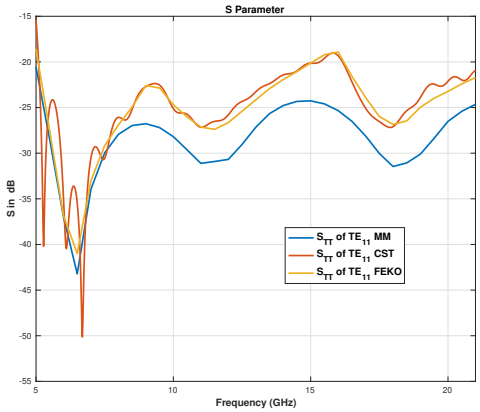

(a) S_{TT} of TE_{11} FEKO/CST vs MM

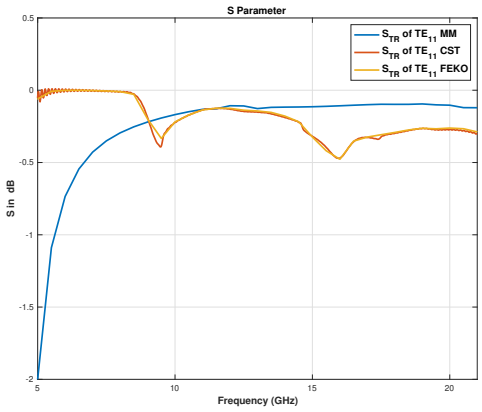

(b) S_{TR} of TE_{11} FEKO/CST vs MM

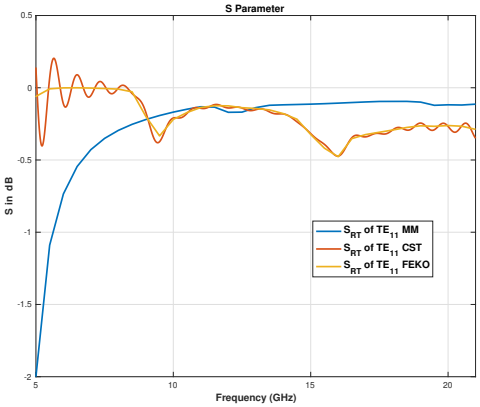

(c) S_{RT} of TE_{11} FEKO/CST vs MM

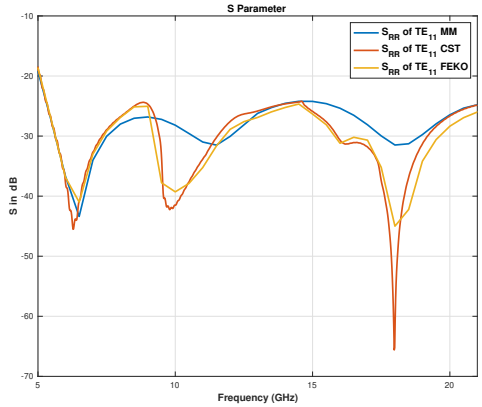

(d) S_{RR} of TE_{11} FEKO/CST vs MM

Figure 4.9: S parameters for TE_{11} mode - FEKO/CST vs MM. 5 modes active on each waveguide (5 waveguide structure)

five waveguide cascaded model was tested next and verified with FEKO and CST simulation results. The MATLAB results have good agreement with the FEKO and CST results showing the correctness of the algorithm for a problem involving three or more waveguides in a cascaded structure. Similarly, a conical waveguide structure was approximated as a cascaded structure of cylindrical waveguides and the resulting structure was implemented in MATLAB to find the GSM. The results have been verified with FEKO and CST results. The results have good agreement with each other. Convergence in the values of GSM was found with an increase of the number of cylindrical elements to approximate a conical waveguide. It is concluded that for accuracy, the cone should be approximated as a cascade cylindrical waveguide model in which each waveguide has a length of at most $\frac{\lambda}{10}$.

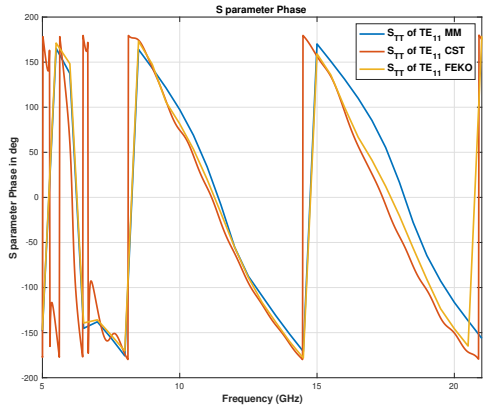

(a) Phase of S_{TT} of TE_{11} FEKO/CST vs MM

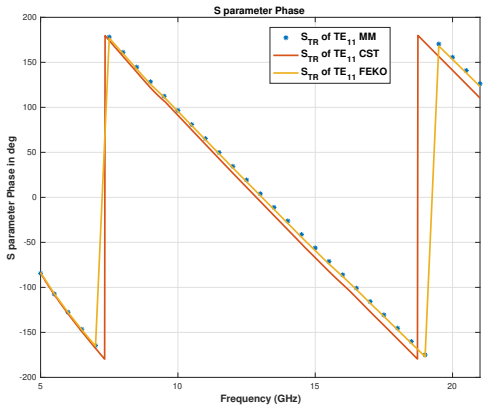

(b) Phase of S_{TR} of TE_{11} FEKO/CST vs MM

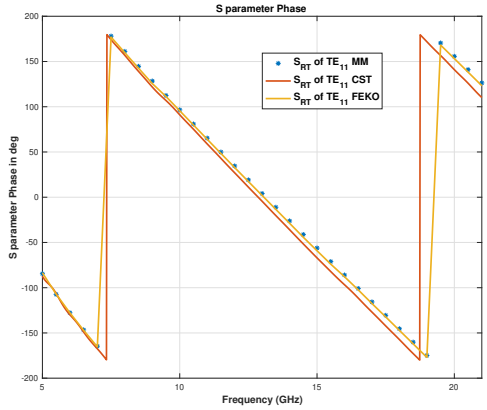

(c) Phase of S_{RT} of TE_{11} FEKO/CST vs MM

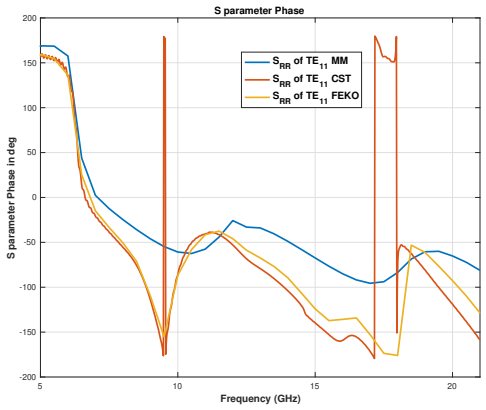

(d) Phase of S_{RR} of TE_{11} FEKO/CST vs MM

Figure 4.10: S parameter phase for TE_{11} mode - FEKO/CST vs MM. 5 modes active on each waveguide (5 waveguide structure)

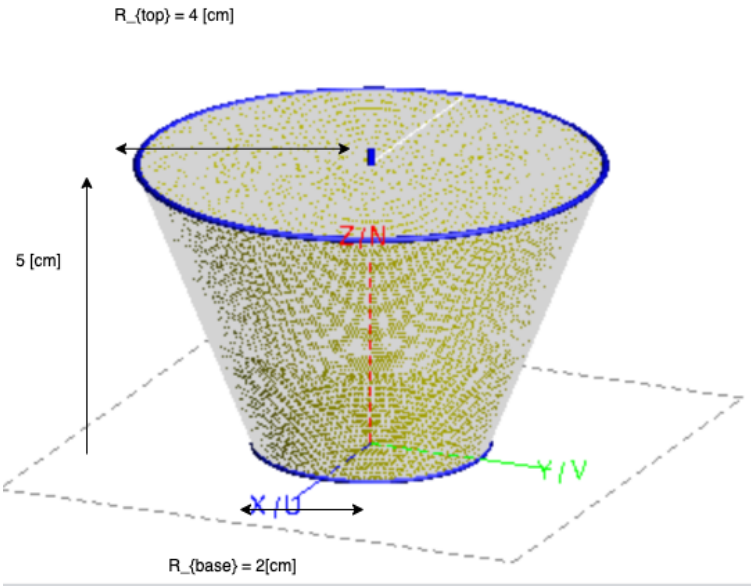

Figure 4.11: Geometry of the conical structure in FEKO

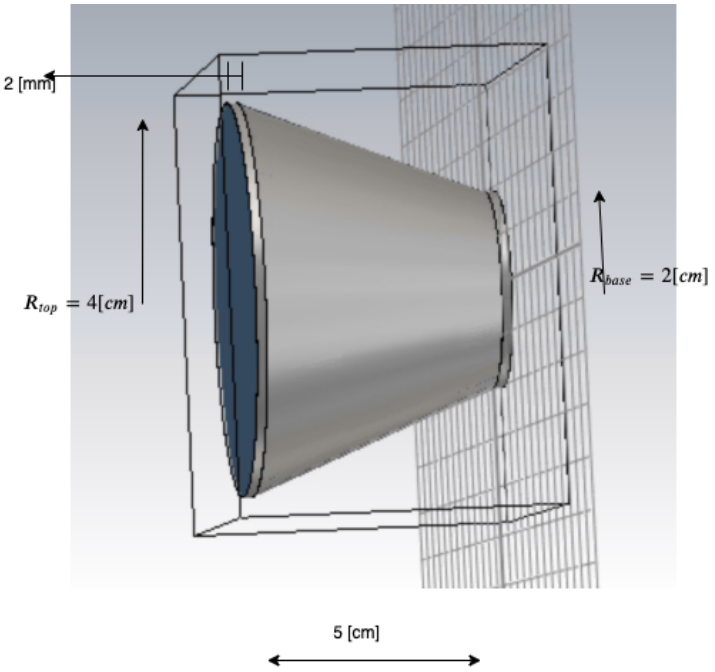

Figure 4.12: Geometry of the conical structure in CST

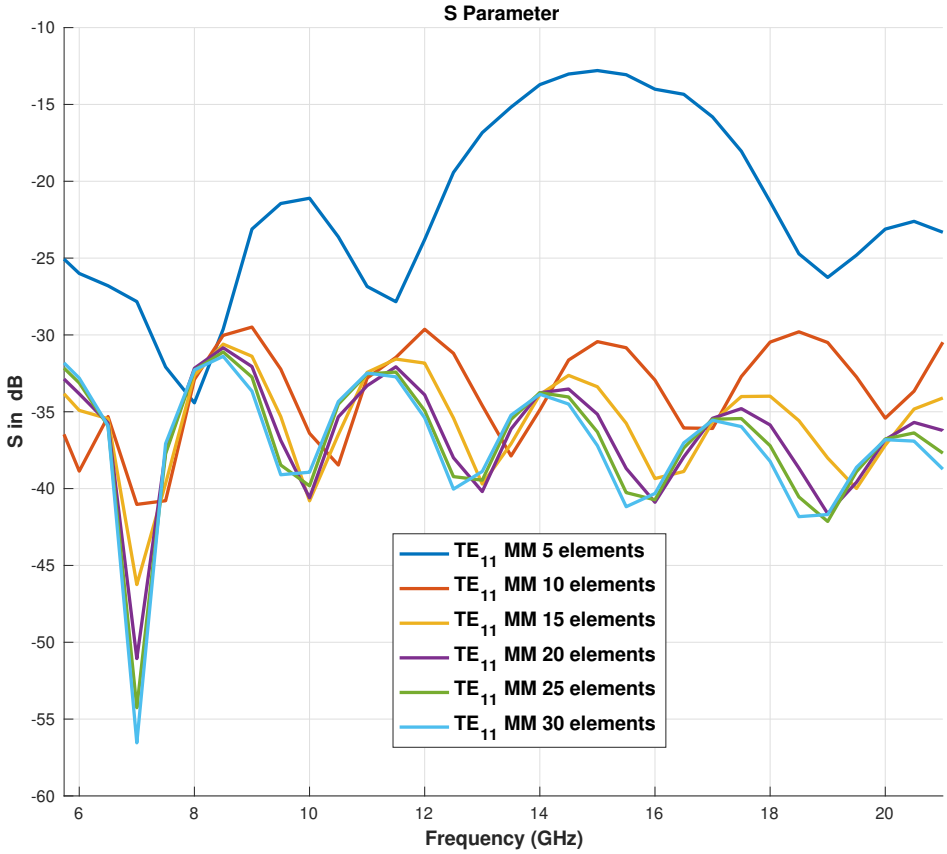

Figure 4.13: Convergence of S_{RR} of TE_{11}

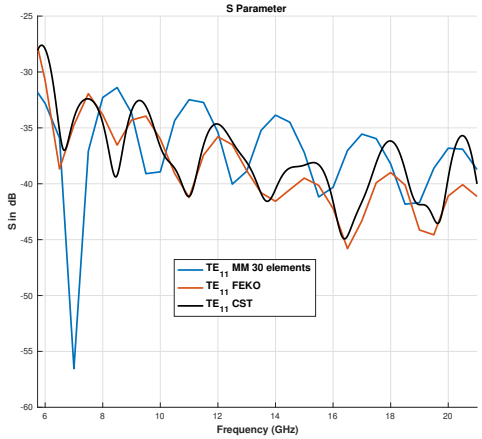

(a) S_{RR} of TE_{11} FEKO/CST vs MM

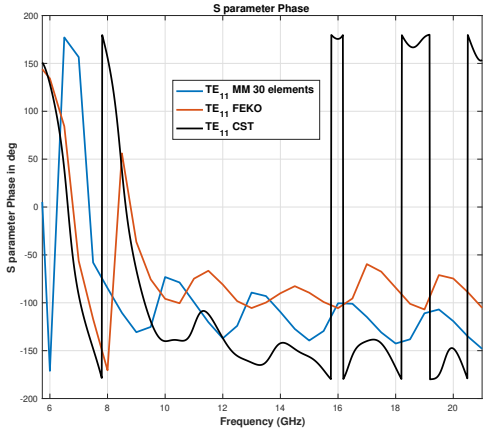

(b) S_{RR} of TE_{11} FEKO/CST vs MM Phase

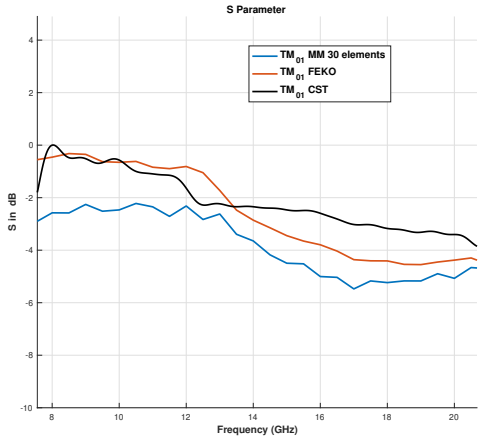

(c) S_{TR} of TM_{01} FEKO/CST vs MM

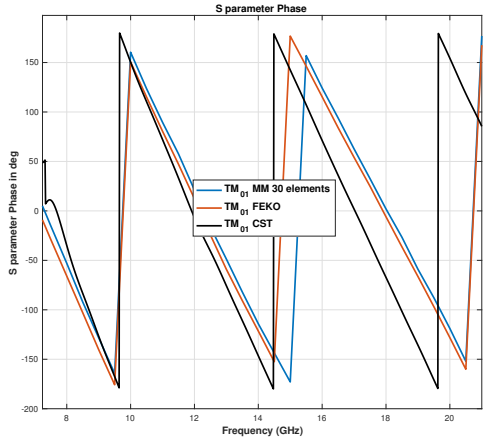

(d) S_{TR} of TM_{01} FEKO/CST vs MM Phase

Figure 4.14: S parameters FEKO/CST vs MM for the Cone Structure

5

Field Distribution on the Aperture and Far Fields of both a perfectly matched waveguide (Infinite length) and Open ended waveguides (Open to free space)

5.1. Field Distribution on the Aperture of an infinitely long waveguide horn

To find the near-field distribution on the aperture, the GSM is used from the MM technique.

$$\vec{E}_t = \sum_{n=1}^{N} (a_n + b_n)\vec{E}_n \tag{5.1}$$

This is from equation (3.1). The coefficients b associated with each mode can be calculated from the GSM and the a coefficients (excitation given to each mode at the waveguide port.)

$$\begin{bmatrix} b_n^T \\ b_n^R \end{bmatrix} = \begin{bmatrix} S_{TT} & S_{TR} \\ S_{RT} & S_{RR} \end{bmatrix} \begin{bmatrix} a_n^T \\ a_n^R \end{bmatrix} \tag{5.2}$$

The GSM can be found by the examples given in chapter 3 and 4. The field equations are given in chapter 2 and [3].

5.1.1. Example with two waveguide structure

The two waveguide structure of chapter two is simulated both on MATLAB (MM technique) and in FEKO (MoM/SEP solver) to find out the near-field at the aperture (both before and after the junction). The configuration is shown in figure 5.1. The plots of normalized aperture fields (Electric fields) after the junction are shown in figure 5.2 for the two waveguide structure. The aperture fields at the aperture of a five waveguide structure in figure 4.8 is shown in figure 5.3. The aperture fields of a conical structure of figure 4.11 is shown in figure 5.4.

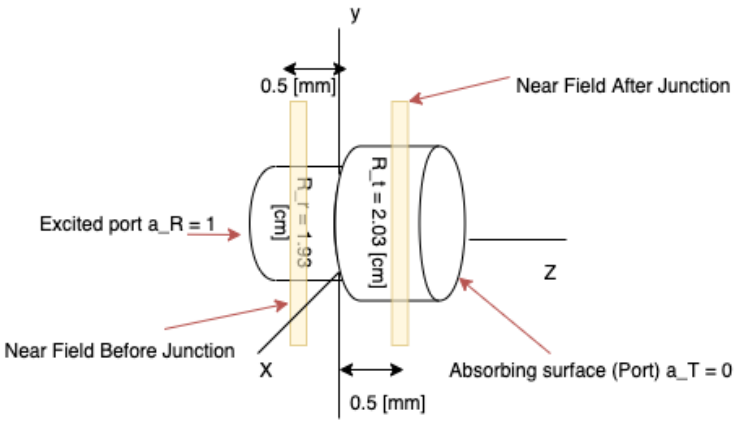

Figure 5.1: Geometry of the five waveguide structure with circular waveguides

Boundary conditions

For this example, the boundary conditions at the bigger waveguide port is set as absorbing. In FEKO, this is achieved by keeping the excitation for modes as 0 at the port. The port modes at the smaller waveguide are excited with an amplitude 1 and with an orientation of zero degree.

Therefore, equation (5.2) becomes (as $a_T = 0$),

$$b_T = S_{TR} a_R \tag{5.3}$$

$$b_R = S_{RR} a_R \tag{5.4}$$

Results

The following figures 5.2, 5.3 and 5.4 show the normalised electric field on the aperture (both ρ and ϕ components) for the two waveguide, five waveguide, and the cone structure respectively.

Observation

The near-field (aperture) patterns are similar for the MM technique in comparison to FEKO simulations except for a few changes. This is due to the fact that especially for some modes the phase at the ports are not similar (out of phase) for MM and FEKO. FEKO allows a waveguide port only on a complete metal surface. For some modes especially, this introduces an extra phase of 180 degrees in FEKO. The modes for which it is observed for transmission coefficient in the first 10 modes are TE_{21}, TE_{01} and TM_{11}. From CST plots of S-parameters, however, this is not observed. An example is shown in figure 5.5 below for TE_{21} mode. Another reason for which the results from FEKO aren't very similar is due to the fact that indirectly FEKO introduces coupling for modes not having the same azimuthal variation. The comparison of transmission coefficients for the cone model is shown in figure 5.6 at 14 GHz. The phase errors are larger sometimes. the phase error of 360 degrees are just the unwrapping of the phase. Therefore, the phases are identical in that case.

5.2. Far-Fields of infinitely long waveguide horns

The far field patterns of the multi waveguide structure can be found by using the near-field pattern of the aperture (which is derived from the MM technique). To calculate the far field patterns, first the aperture current distribution has to be found out. To do this, equivalence principle is used. By incorporating equivalene principle a E-field model is used. In this model, an imaginary PEC (Perfect

Electric conductor) is placed behind the sources. By the use of image theory, it is found that the equivalent surface has no electric currents $J = 0$ and 2 times the equivalent magnetic current produced by the incident electric field.

$$\vec{M} = \hat{z} \times 2\vec{E_t} \tag{5.5}$$

So, M as a combination of ρ and ϕ components are given below.

$$\vec{M} \propto -E_{t\phi}\hat{\rho} + E_{t\rho}\hat{\phi}; \tag{5.6}$$

The far field is given by the fast Fourier transform (FFT) of the near-field distribution, which is given by

$$E^{FF}(\theta, \phi) = \int\int_{S'} E_t(x', y')e^{-jkr}dS \tag{5.7}$$

Here r is defined as $|\rho_0 - \rho'|$, where ρ_0 is the centre of this aperture and ρ' is the distance from any arbitrary point on the aperture from the aperture centre. This can be broken down to:

$$r = \rho_0 - \rho' \sin\theta_{obs} \cos(\phi_{obs} - \phi') \tag{5.8}$$

Where θ_{obs} and ϕ_{obs} define the observation points in space and ϕ' defines the azimuth location of a point on the aperture field domain.

The FFT due to the x and y components of the near-field pattern can be expressed as below:

$$I_x(\theta, \phi) = \int\int_{S'} E_{tx}(x', y')e^{-jk\rho' \sin\theta_{obs}\cos(\phi_{obs}-\phi')}\rho' d\rho' d\phi' \tag{5.9}$$

$$I_y(\theta, \phi) = \int\int_{S'} E_{ty}(x', y')e^{-jk\rho' \sin\theta_{obs}\cos(\phi_{obs}-\phi')}\rho' d\rho' d\phi' \tag{5.10}$$

Here, the integration is in the cylindrical aperture domain. The Cartesian components E_{tx} and E_{ty} can be found from the cylindrical components as:

$$E_{tx} = \cos\phi E_{t\rho}(\rho, \phi) - \sin\phi E_{t\phi}(\rho, \phi) \tag{5.11}$$

$$E_{ty} = sin\phi E_{t\rho}(\rho, \phi) + \cos\phi E_{t\phi}(\rho, \phi) \tag{5.12}$$

The far fields then become proportional to the following:

$$E_{\theta_{obs}}(\theta_{obs}, \phi_{obs}) \propto (I_x \cos\phi_{obs} + I_y \sin\phi_{obs}) \tag{5.13}$$

$$E_{\phi_{obs}}(\theta_{obs}, \phi_{obs}) \propto \cos\theta(-I_x \sin\phi_{obs} + I_y \cos\phi_{obs}) \tag{5.14}$$

The far fields patterns are shown in figure 5.7 for two waveguide model at 14 GHz (10 modes propagating for the first waveguide). Figure 5.8 and 5.9 show far fields from the aperture fields of the cone problem at 6 GHz and 7.5 GHz respectively where port1 (at base radius) has two and three modes propagating respectively.

5.3. Free-space reflection at the end of an open waveguide with a metal flange

Till now the far-fields and the near-fields were measured by the aperture fields on the waveguide aperture when it is infinitely long (perfectly matched to free-space). In the case of horn antennas, it was considerd that the waveguide after the last transition is infinitely long. This was achieved in FEKO by putting an absorbing boundary condition at the far end of the waveguide when computing the near-fields. However, in practice, there should be an open end to the waveguide such that the energy is radiated in the far-fields. Therefore, for accurate computation of fields in the far zone and near-fields on the aperture, the reflection at the waveguide-free-space boundary needs to be taken into consideration. The boundary can excite more waveguide modes into the waveguide. Therefore, the refection from higher order modes needs to be taken care of as well.

There are ways to determine the reflection from the aperture of a waveguide. The methods in the literature that is found are listed below.

- Spherical wave expansion of free-space along with boundary condition mode matching technique
- Gaussian Beam Mode Analysis (GBMA)
- Aperture admittance methods with Fredholm integral equations
- Spectral domain reaction integral methods on the basis of Rumsey's reaction integrals with a variational approach.

5.3.1. Spherical Wave Expansion Method

In spherical wave expansion method the Electromagnetic (EM) fields in free-space are assumed to be the superposition of a number of TE/TM spherical modes. The implementation can be found in the literature [26] [27] [17] [20]. These expansion along with the boundary condition mode matching technique can determine the weights of each spherical mode in the eign expansion of free-space. This method requires a common origin for both the waveguide and the free-space. As the waveguide in the problem of this thesis is a conical waveguide (cylindrical waveguide), the waves are resp represented in cylindrical coordinate system. However, outside the aperture, the fields are represented in spherical coordinate system. To find a common origin for both modes, approximations have to be made. For example, the best candidate for the origin of the reference is the phase center of the waveguide. To determine that, an approximate concave surface has to be found for the waveguide where the phase remains constant. Then, after extending the concave surface to a sphere, the center of that sphere can be taken as the phase center. The method is too involved and the complexity becomes more when a conical horn is considered instead of a simple cylindrical waveguide. The free-space tesseral harmonics are expressed as [20],

$$T_{even}(m, n) = A\cos(m\phi)P_n^m(\cos\theta) \tag{5.15}$$

$$T_{odd}(m,n) = A\sin(m\phi)P_n^m(\cos\theta) \tag{5.16}$$

Where, P_n^m are associated Legendre's functions. These harmonics are used as potential functions to find the field expressions in the spherical coordinate system for free-space.

There is another approach to make use of spherical wave expansion method where the waveguide modes are expressed in spherical coordinate system as well. This is especially done for horn antennas like the conical horn antennas where the waveguide eign-modes are already known in spherical modes [29]. However, the complexity of that method is too high and also the computational complexity also is very high.

In this thesis, spherical modes are not explored for verification.

5.3.2. Gaussian Beam Mode Analysis (GBMA)

Gaussian Beam analysis is another technique by virtue of which the radiated fields from the aperture of a waveguide can be determined. This method assumes that the fields on the aperture of the waveguide are scalar fields. The more this scalar fields resemble a Gaussian pattern, the better the approximation works. Therefore, it is generally used for high frequencies. The electrical size of the device should be very high so that this approximation that the fields on the aperture are scalar fits the observations. This method is used in [32] [10]. This scalar field representation of the field on the aperture can be matched to the spherical mode expansion of free-space to find the weights of the modes [18]. However, it is useful when the device is electrically large. Therefore, this method is also not very useful to predict the field patterns very accurately for the AUT (Antenna Under Test).

5.3.3. Aperture admittance methods with Fredholm integral equations

In this approach (Implemented for cylindrical waveguides with a metal flange at the aperture in [19], [7] and [6]), a Green's function approach is used to find the aperture admittance of the waveguide free-space boundary. At first the equivalent magnetic current on the aperture is formulated. From the equivalent magnetic currents, the magnetic field is determined using the Green's function of free-space. Then, by using the boundary conditions (continuity of tangential electric and magnetic fields at the aperture), the equations for the aperture admittance is found out. The Green's function for the free-space is then expanded using a Fourier series expansion in cylindrical coordinates (for cylindrical waveguides). However, in [19], [7] and [6] the higher order mode excitation at the aperture is not considered due to the awkwardness of the expressions of the magnetic current at the aperture. In this thesis, the expressions for the aperture admittance from this method is used from [19]. In later sections, the results are mathched with the procedure done using the spectral domain representation of the EM fields in free-space 5.3.4.

$$y_{ap} = \frac{Y_{ap}}{Y_{FS}} = \frac{2(\mathrm{X}'_{1,1})^2(\frac{\mathrm{X}'_{11}}{k_0R})^2}{[(\mathrm{X}'_{11})^2-1]\sqrt{1-(\frac{\mathrm{X}'_{1,1}}{k_0R})^2}}\int_0^\infty \frac{\eta\sqrt{1-\eta^2}[J_1'(k_0R\eta)]^2}{\left[(\frac{\mathrm{X}'_{11}}{k_0R})^2-\eta^2\right]^2}d\eta + \frac{2}{[(\mathrm{X}'_{11})^2-1]\sqrt{1-(\frac{\mathrm{X}'_{1,1}}{k_0R})^2}}\int_0^\infty\left(\frac{[J_1(k_0R\eta)]^2}{\eta\sqrt{1-\eta^2}}\right)d\eta$$

Where, X'_{11} is the first zero of derivative of the Bessel's function of the first kind and of first order.

k_0 is the free-space wave number, R is the waveguide radius, η is the ratio of the radial wavenumber in free-space to the wave number in free-space. Y_{FS} is the free-space wave admittance.

$$\eta = \frac{k_\Omega}{k_0} = \frac{\sqrt{k_x^2 + k_y^2}}{k_0} \tag{5.17}$$

From this, the reflection coefficient can be found as,

$$\Gamma = \frac{1 - y_{ap}}{1 + y_{ap}} \tag{5.18}$$

The term $\sqrt{1-\eta^2}$ is always computed as $-1j\sqrt{-(1-\eta^2)}$ to maintain propagation characteristic of the EM waves (explained in chapter 2). As in the above integral there are branch points present at $\eta = \pm 1$ and poles at $\eta = \pm\frac{X'_{11}}{k_0 R}$, the integration is carried out in complex plane. The branch cuts, branch points, poles are shown in figure 5.10. The integration path should be chosen so that the poles are avoided and the branch cuts aren't crossed. The integral path shown in figure 5.10 should be followed while integrating the above expression. It is interesting to notice that the integral from 0 to 1 yields the real part of the aperture admittance whereas the integral from 1 to ∞ yields the imaginary part of the aperture admittance. This happens because of the fact that the square root function becomes purely imaginary when $|\eta| > 1$.

5.3.4. Spectral domain solution using Rumsey's reaction integrals

The coming subsections in the document explain the aperture reflection with the Rumsey's reaction integral method mentioned in [1]. It also has been verified and implemented in the PhD thesis [22] for rectangular waveguide when excited only with the fundamental mode.

This procedure is very similar to the above mentioned method in section 5.3.3. However, it is carried out in the spectral domain. Therefore, the fields of the free-space are expressed in terms of the spectral domain Green's functions of the potentials. The reaction integral is nothing but the conjugate power. In the rectangular waveguide case in [22], it is assumed that at the aperture, due to the discontinuity, higher order modes of the waveguide can be excited. Using the same principles, parameters such as the aperture admittance, the reflection coefficient and the excitation coefficients for the higher order modes at the aperture are derived for cylindrical waveguides in this thesis. In the circular waveguide case also the fundamental mode excitation is considered in the beginning.

Rectangular Waveguide with a Metal Flange

In this section, for simplicity, a rectangular waveguide is tested with the fundamental mode excitation (i.e the TE10 mode). It is assumed that there is an infinite ground plane which surrounds the aperture. The electric field of TE10 mode has only one component which is the y component in this case and therefore, there should be one component of magnetic field which is the x component. If we incorporate the reflection from the aperture-free-space boundary, we can write the tangential components as follows. Only $TE_{m,0}$ higher order modes are taken in consideration at the aperture where $m = 3, 5, 7, \ldots$ (Remember to cite).

$$E_y^{(1)} = E_0(1+\Gamma)\cos(\frac{\pi x}{a}) + \sum_{m=3,5,\ldots}^{\infty} E_0(1+\Gamma)D_m \cos(\frac{m\pi x}{a}) \tag{5.19}$$

$$H_x^{(1)} = -E_0 Y_{10}(1-\Gamma)\cos(\frac{\pi x}{a}) + \sum_{m=3,5,\dots}^{\infty} E_0(1+\Gamma)D_m Y_{m0}\cos(\frac{m\pi x}{a}) \tag{5.20}$$

Here, E_0 is the amplitude of the field for TE_{10} mode. Γ is the refection from the boundary and D_m is the excitation constant of the higher order modes at the aperture. Y_{10} is the characteristic admittance of the mode TE_{10} and Y_{m0} is the characteristic impedance of the mode TE_{m0}. (1) refers to the waveguide (medium 1). Applying Rumsey's reaction concept, the unknown quantities (Γ and D_m) can be found. (Remember to cite).

$$< 1,1 >= \int\int_{S_{aperture}} H^{(1)}(x,y,z).(\hat{z} \times E^{(1)}(x,y,z))dS \tag{5.21}$$

which then can be further written as (using orthogonality of modes),

$$< 1,1 >= E_0^2(1+\Gamma^2)\frac{ab}{2}\Big(Y_{10}\frac{1-\Gamma}{1+\Gamma} - \sum_{m=3,5,\dots}^{\infty} D_m^2 Y_{m0}\Big) \tag{5.22}$$

The aperture admittance in this can be written in terms of the reflection coefficient as,

$$y_{ap} = \frac{1-\Gamma}{1+\Gamma} \tag{5.23}$$

In another form it can be written as [22],

$$y_{ap} = \frac{< 1,1 >}{\frac{ab}{2}E_0^2(1+\Gamma)^2 Y_{10}} + \sum_{m=3,5,\dots}^{\infty} D_m^2 \frac{Y_{m0}}{Y_{10}} \tag{5.24}$$

The reaction integral outside the aperture (in free-space) also can be determined and which should be essentially the same as the reaction integral of the inner fields inside the waveguide. (2) stands for the seond medium and in this case it is free-space.

$$< 2,2 >= \int\int_{S_{aperture}} H^{(2)}(x,y,z).(\hat{z} \times E^{(2)}(x,y,z))dS \tag{5.25}$$

In spectral domain representation it can be written as,

$$< 2,2 >= -\int\int_{S_{aperture}} E_y^{(2)}(x,y)H_x^{(2)}(x,y)dS = -\frac{1}{4\pi^2}\int_{-\infty}^{\infty}\int_{-\infty}^{\infty} E_y^{(2)}(k_x,k_y)H_x^{(2)}(k_x,k_y)dk_x dk_y \tag{5.26}$$

$E_y^{(2)}(k_x,k_y)$ and $H_x^{(2)}(k_x,k_y)$ are spectral domain representation of the field components. They can all be found in [[22]].

Using the spectral domain field representations of [22], $H_x^{(2)}(k_x,k_y)$ can be written in terms of $E_y^{(2)}(k_x,k_y)$ and $E_x^{(2)}(k_x,k_y)$.

$$H_x^{(2)}(k_x,k_y) = -\frac{1}{\omega\mu k_z}\Big(k_x k_y E_x^{(2)}(k_x,k_y) + (k^2 - k_x^2)E_y^{(2)}(k_x,k_y)\Big) \tag{5.27}$$

From electric field boundary condition at the aperture we know,

$$E_x^{(2)}(k_x,k_y) = E_x^{(1)}(k_x,k_y) \quad |_{S_{ap}} \tag{5.28}$$

$$E_y^{(2)}(k_x,k_y) = E_y^{(1)}(k_x,k_y) \quad |_{S_{ap}} \tag{5.29}$$

As $E_x^{(1)}(x,y) = 0$, $E_x^{(1)}(k_x,k_y,z_{ap}) = 0$. Therefore,

$$H_x^{(2)}(k_x,k_y) = -\frac{1}{\omega\mu k_z}\Big((k^2 - k_x^2)E_y^{(1)}(k_x,k_y)\Big) \tag{5.30}$$

Therefore, the reaction integral in the second medium can be written as,

$$< 2,2 >= \frac{1}{4\pi^2} - \int_{-\infty}^{\infty}\int_{-\infty}^{\infty}\frac{1}{\omega\mu k_z}(k^2 - k_x^2)(E_y^{(2)}(k_x,k_y))^2 dk_x dk_y \tag{5.31}$$

The spectral field representation of $E_y^{(1)}(k_x,k_y)$ can be given as,

$$E_y^{(1)}(k_x,k_y) = \int\int_{S'_{aperture}} E_y^{(1)}(x,y)e^{jk_x x' + k_y y'}\, dS' \tag{5.32}$$

It can be analytically found for the rectangular waveguides and is given by,

$$E_y^{(1)}(k_x,k_y) = E_0(1+\Gamma)C_0(k_y)\Big(C_1(kx) + \sum_{m=3,5,\ldots}^{\infty} D_m C_m(k_x)\Big) \tag{5.33}$$

Where $C_0(k_y)$ and $C_m(k_x)$ are given by,

$$C_0(k_y) = \frac{\sin(\frac{k_y b}{2})}{\frac{k_y b}{2}} \tag{5.34}$$

$$C_m(k_x) = \int_{-\frac{a}{2}}^{\frac{a}{2}} \cos(\frac{m\pi x}{2})e^{jk_x x'}dx' = \frac{2m\pi a j^{m-1}\cos(\frac{k_x a}{2})}{(m\pi)^2 - (k_x a)^2} \tag{5.35}$$

Using the expression for $E_y^{(1)}(k_x, k_y)$, the reaction intgral can be formed and using the reaction integral $< 2,2 >=< 1,1 >$, the aperture admittance can be formed.

The aperture admittance can be found as,

$$y_{ap} = \frac{Y_{mut,11}}{Y_{10}} + 2\sum_{m=3,5,\dots}^{\infty} \frac{Y_{mut,1m}}{Y_{10}} + \sum_{m=3,5,\dots}^{\infty}\sum_{n=3,5,\dots}^{\infty} \frac{Y_{mut,mn}}{Y_{10}} + \sum_{m=3,5,\dots}^{\infty} D_m^2 \frac{Y_{m0}}{Y_{10}} \tag{5.36}$$

Here, $Y_{mut,mn}$ are the mutual admittance between modes of the waveguide and can be represented by,

$$Y_{mut,mn} = -j^{m+n} nm \int_{-\infty}^{\infty}\int_{-\infty}^{\infty} \frac{2ab(k^2 - k_x^2)\sin^2(\frac{k_y b}{2})\cos^2(\frac{k_x a}{2})}{\omega\mu k_z(\frac{k_y b}{2})^2[(n\pi)^2 - (k_x a)^2][(m\pi)^2 - (k_x a)^2]} dk_x dk_y \tag{5.37}$$

This can be reduced to a numerical integral in spacial domain which is given in the appendix of [[22]].

The value of y_{ap} should be invariable and therefore the condition $\frac{\partial y_{ap}}{\partial D_m} = 0$ is applied and the result of this application is presented in matrix form below.

$$\begin{bmatrix} Y_{mut,33} + Y_{30} & Y_{mut,35} & \dots & Y_{mut,3\infty} \\ Y_{mut,53} & Y_{mut,55} + Y_{50} & \dots & Y_{mut,5\infty} \\ . & . & \dots & . \\ Y_{mut,\infty 3} & . & \dots & Y_{mut,\infty\infty} + Y_{\infty 0} \end{bmatrix} \begin{bmatrix} D_3 \\ D_5 \\ . \\ D_\infty \end{bmatrix} = \begin{bmatrix} -Y_{mut,13} \\ -Y_{mut,15} \\ . \\ -Y_{mut,1\infty} \end{bmatrix} \tag{5.38}$$

From this, with an inverse operation the D_m values can be found. Using the above relation, the aperture admittance can be even more simplified and is given by,

$$y_{ap} Y_{1,0} = Y_{mut,11} + \begin{bmatrix} D_3 & D_5 & \dots & D_\infty \end{bmatrix} \begin{bmatrix} Y_{mut,13} \\ Y_{mut,15} \\ . \\ Y_{mut,1\infty} \end{bmatrix} \tag{5.39}$$

After the evaluation of y_{ap}, the reflection coefficient Γ can be found from equation (5.19). Using these values the aperture field can be computed as equation (5.15).

This model assumes that the aperture lies on a infinite ground plane. For this model the far-fields can be computed in a very similar approach as equation (5.13) and (5.14) except for the fact that here, $I_x(k_x, k_y) = 0$ and $I_y(k_x, k_y) = E_y^{(1)}(k_x, k_y)$. Therefore, the far-field of this configuration can be expressed as,

$$E_{\theta_{obs}}^{FF} \propto E_y^{(1)}(k_x, k_y)\sin\phi_{obs} \tag{5.40}$$

$$E_{\phi_{obs}}^{FF} \propto E_y^{(1)}(k_x, k_y)\cos\theta_{obs}\cos\phi_{obs} \tag{5.41}$$

Circular Waveguide with a Metal Flange

Similarly the same reaction integrals can be used for a circular cross section waveguide. The tangential field component here has both a ρ component and a ϕ component. It can be written as,

$$E_{\rho}^{(1)} = \sqrt{(N_{11}^{TE})}(1+\Gamma)\frac{1}{\rho}J_1(\beta_{\rho,(1,1)}\rho)\sin(\phi) + \sum_{n=2,3,..}^{\infty}\sqrt{(N_{1n}^{TE})}(1+\Gamma)\frac{1}{\rho}J_1(\beta_{\rho,(1,n)}\rho)\sin(\phi)D_n^{TE} \quad (5.42)$$

$$E_{\phi}^{(1)} = \sqrt{(N_{11}^{TE})}(1+\Gamma)\beta_{\rho,(1,1)}J_1'(\beta_{\rho,(1,1)}\rho)\cos(\phi) + \sum_{n=2,3,..}^{\infty}\sqrt{(N_{1n}^{TE})}(1+\Gamma)\beta_{\rho,(1,n)}J_1'(\beta_{\rho,(1,n)}\rho)\cos(\phi) \quad (5.43)$$

Here, only the modes TE_{1n} are considered because they have the same azimuthal variation with TE_{11} mode and most likely to have coupling with TE_{11} mode at the aperture. This can be assumed because of the analysis of mode matching technique. Here, $N_{1,n}^{TE}$ is the normalization constants of the modes TE_{1n}. They can derived by the same procedure mentioned in section 3.2.1. For TE modes, the normalization is constant is,

$$N_{mn}^{TE} = \frac{\frac{2}{\pi}}{J_m^2(\mathrm{X}'_{m,n})(\mathrm{X}'^2_{m,n} - m^2)} \quad (5.44)$$

Similarly the magnetic fields are,

$$H_{\rho}^{(1)} = -\sqrt{(N_{11}^{TE})}(1-\Gamma)Y_{11}^{TE}\beta_{\rho,(1,1)}J_1'(\beta_{\rho,(1,1)}\rho)\cos(\phi) + \sum_{n=2,3,..}^{\infty}\sqrt{(N_{1n}^{TE})}(1+\Gamma)\beta_{\rho,(1,n)}J_1'(\beta_{\rho,(1,n)}\rho)\cos(\phi)Y_{1n}^{TE}D_n^{TE} \quad (5.45)$$

$$H_{\phi}^{(1)} = \sqrt{(N_{11}^{TE})}(1-\Gamma)Y_{11}^{TE}\frac{1}{\rho}J_1(\beta_{\rho,(1,1)}\rho)\sin(\phi) - \sum_{n=2,3,..}^{\infty}\sqrt{(N_{1n}^{TE})}(1+\Gamma)\frac{1}{\rho}J_1(\beta_{\rho,(1,n)}\rho)\sin(\phi)Y_{1n}^{TE}D_n^{TE} \quad (5.46)$$

Therefore, the reaction integral can be written as,

$$< 1,1 >= \int\int_{S_{ap}} (E_{\rho}H_{\phi} - H_{\rho}E_{\phi})dS \quad (5.47)$$

This gives rise to (Incorporating the orthogonality property of the modes),

$$< 1,1 >= \int\int_{S_{ap}} \Big((N_{11}^{TE})(1+\Gamma)(1-\Gamma) Y_{11}^{TE} \frac{1}{\rho^2} J_1^2(\beta_{\rho,(1,1)}\rho) \sin^2\phi + (N_{11}^{TE})(1+\Gamma)(1-\Gamma) Y_{11}^{TE} \beta_{\rho,(1,1)}^2 J_1'^2(\beta_{\rho,(1,1)}\rho) \cos^2\phi - \sum_{n=1,2..}^{\infty} (N_{1n}^{TE})(1+\Gamma)^2 \frac{1}{\rho^2} J_1^2(\beta_{\rho,(1,n)}\rho) \sin^2\phi D_n^2 - \sum_{n=1,2..}^{\infty} (N_{1n}^{TE})(1+\Gamma)^2 Y_{11}^{TE} \beta_{\rho,(1,n)}^2 J_1'^2(\beta_{\rho,(1,n)}\rho) \cos^2\phi D_n^2 \Big) dS$$

This can be reduced to (using the integrals of section 3.2.1),

$$< 1,1 >= \frac{\pi}{2}(1+\Gamma)^2 \left[\frac{1-\Gamma}{1+\Gamma} (N_{11}^{TE}) Y_{11}^{TE} J_1^2(\mathrm{X}'_{1,1})(\mathrm{X}'^2_{1,1} - 1) \right] - \sum_{n=1,2,...}^{\infty} \frac{\pi}{2}(1+\Gamma)^2 \left[(N_{1n}^{TE}) Y_{1n}^{TE} J_1^2(\mathrm{X}'_{1,n})(\mathrm{X}'^2_{1,n} - 1) D_n^2 \right]$$

$\Rightarrow$

$$< 1,1 >= (1+\Gamma)^2 \left[\frac{1-\Gamma}{1+\Gamma} Y_{11}^{TE} \right] - \sum_{n=1,2,...}^{\infty} (1+\Gamma)^2 \left[Y_{1n}^{TE} D_n^2 \right] \tag{5.48}$$

Considering aperture admittance as $y_{ap} = \frac{1-\Gamma}{1+\Gamma}$, we can write,

$$y_{ap} = \frac{< 1,1 >}{(1+\Gamma)^2 Y_{11}^{TE}} + \sum_{n=1,2,...}^{\infty} \left[D_n^2 \frac{Y_{1n}^{TE}}{Y_{11}^{TE}} \right] \tag{5.49}$$

Now it is time to calculate the reaction integral in the second medium (free-space). As the fundamental mode of a circular waveguide has both the x and y component, using the boundary conditions for the continuity of tangential electric and magnetic fields, it can be said that the x and y component of both components in the second medium are also finite (Unlike the rectangular waveguide case). Using the Green's function spectral domain representation of EM fields explained in [[22]], the magnetic field components can be written as,

$$H_x^{(2)}(k_x, k_y) = -\frac{1}{\omega\mu k_z}(k_x k_y E_x^{(2)}(k_x, k_y) + (k^2 - k_x^2) E_y^{(2)}(k_x, k_y)) \tag{5.50}$$

$$H_y^{(2)}(k_x, k_y) = \frac{1}{\omega\mu k_z}(k_x k_y E_y^{(2)}(k_x, k_y) + (k^2 - k_y^2) E_x^{(2)}(k_x, k_y)) \tag{5.51}$$

Therefore, the reaction integral in the second medium is given by,

$$< 2,2 >= \int\int_{S_{aperture}} H^{(2)}(x,y,z).(\hat{z} \times E^{(2)}(x,y,z))dS \tag{5.52}$$

In spectral domain representation it can be written as,

$$< 2,2 >= \int\int_{S_{aperture}} (E_x^{(2)}(x,y)H_y^{(2)}(x,y) - E_y^{(2)}(x,y)H_x^{(2)}(x,y))dS$$
$$= \frac{1}{4\pi^2}\int_{-\infty}^{\infty}\int_{-\infty}^{\infty}(E_x^{(2)}(k_x,k_y)H_y^{(2)}(k_x,k_y) - E_y^{(2)}(k_x,k_y)H_x^{(2)}(k_x,k_y))dk_xdk_y$$

The term $< 2,2 >$ can be written only in terms of the spectral electric fields as,

$$< 2,2 >= \int\int_{S_{aperture}} \frac{1}{\omega\mu k_z}(E_x^{(2)}(x,y)H_y^{(2)}(x,y) - E_y^{(2)}(x,y)H_x^{(2)}(x,y))dS$$
$$= \frac{1}{4\pi^2}\int_{-\infty}^{\infty}\int_{-\infty}^{\infty}(2k_xk_yE_x^{(1)}(k_x,k_y)E_y^{(1)}(k_x,k_y)+(k^2-k_y^2)E_x^{(1)}(k_x,k_y)^2+(k^2-k_x^2)E_y^{(1)}(k_x,k_y)^2)dk_xdk_y$$

The (2) is replaced with (1), because the reaction integrals are found at the aperture and the boundary conditions suggest that the tangential fields should be continuous at the aperture.

The spectral domain representation of the fields can be computed efficiently if the Fourier transforms of the fields E_x and E_y in spectral domain are known analytically. Therefore, the spectral integral was carried out to find the analytical expressions for the spectra domain fields of E_x and E_y.

Let's now instead of finding a function of (k_x, k_y), functions of (k_Ω, Θ) can be derived. The terms (k_Ω, Θ) are defined as,

$$k_\Omega = \sqrt{(k_x^2 + k_y^2)} \tag{5.53}$$

$$\Theta = \arccos(\frac{k_x}{k_\Omega}) = \arcsin(\frac{k_y}{k_\Omega}) \tag{5.54}$$

The example below is given for E_x^{TE}.

$$E_x^{TE}(k_\Omega,\Theta) = \sqrt{(}N_{11}^{TE})(1+\Gamma)\int\int_{S_{ap}}\Big[\sin\phi\cos\phi\Big(\frac{1}{\rho}J_1(\beta_{\rho,(1,1)}\rho) - \beta_{\rho,(1,1)}J_1'(\beta_{\rho,(1,1)}\rho)\Big)\Big]e^{k_\Omega\rho\cos(\phi-\Theta)}\rho d\rho d\phi$$
$$+\sum_{n=1,2,..}^{\infty}\sqrt{(}N_{1n}^{TE})D_n(1+\Gamma)\int\int_{S_{ap}}\Big[\sin\phi\cos\phi\Big(\frac{1}{\rho}J_1(\beta_{\rho,(1,n)}\rho) - \beta_{\rho,(1,n)}J_1'(\beta_{\rho,(1,n)}\rho)\Big)\Big]e^{k_\Omega\rho\cos(\phi-\Theta)}\rho d\rho d\phi$$

It can be simply written as,

$$E_x^{TE}(k_\Omega,\Theta)=\sqrt{(}N_{11}^{TE})(1+\Gamma)\ddot{o}_{11}^{TE}(k_\Omega,\Theta)+\sum_{n=1,2,..}^{\infty}\sqrt{(}N_{1n}^{TE})(1+\Gamma)D_n\ddot{o}_{1n}^{TE}(k_\Omega,\Theta) \tag{5.55}$$

Where,

$$\ddot{o}_{1n}^{TE}(k_\Omega,\Theta)=\int_0^R\left(\left(\frac{1}{\rho}J_1(\beta_{\rho,(1,n)}\rho)-\beta_{\rho,(1,n)}J_1'(\beta_{\rho,(1,n)}\rho)\right)\left(\int_0^{2\pi}\sin\phi\cos\phi e^{k_\Omega\rho\cos(\phi-\Theta)}d\phi\right)\rho d\rho\right) \tag{5.56}$$

This integral can be analytically derived by using the bessel function properties of equation (3.11), (3.12) and the equation given below (5.59).

$$J_l(\beta)=\frac{1}{2\pi j^l}\int_0^{2\pi}e^{jl\phi}e^{j\beta\cos\phi}d\phi \tag{5.57}$$

Finally the integral $\ddot{o}_{1n}^{TE}$ is given by,

$$\ddot{o}_{1n}^{TE}(k_\Omega,\Theta)=-\pi\beta_{\rho(1,n)}\sin(2\Theta)I_{22}^{1,n} \tag{5.58}$$

Where, I_{22} is given by,

$$I_{22}^{1,n}(k_\Omega)=\int_0^R\rho J_2(\beta_{\rho(1,n)})J_2(k_\Omega\rho)d\rho \tag{5.59}$$

This integral can be solved with the Lommel's integral of the form (3.85).

Similarly the spectrum function of $E_y(x,y)$ can be found as,

$$E_y^{TE}(k_\Omega,\Theta)=\sqrt{(}N_{11}^{TE})(1+\Gamma)\int\int_{S_{ap}}\left[\left(\frac{1}{\rho}J_1(\beta_{\rho,(1,1)}\rho)\sin^2\phi+\beta_{\rho,(1,1)}J_1'(\beta_{\rho,(1,1)}\rho)\cos^2\phi\right)\right]e^{k_\Omega\rho\cos(\phi-\Theta)}\rho d\rho d\phi$$

$$+\sum_{n=1,2,..}^{\infty}\sqrt{(}N_{1n}^{TE})D_n(1+\Gamma)\int\int_{S_{ap}}\left[\left(\frac{1}{\rho}J_1(\beta_{\rho,(1,n)}\rho)\sin^2\phi+\beta_{\rho,(1,n)}J_1'(\beta_{\rho,(1,n)}\rho)\cos^2\phi\right)\right]e^{k_\Omega\rho\cos(\phi-\Theta)}\rho d\rho d\phi$$

It can be simply written as,

$$E_y^{TE}(k_x,k_y)=\sqrt{(}N_{11}^{TE})(1+\Gamma)\ddot{u}_{11}^{TE}(k_\Omega,\Theta)+\sum_{n=1,2,..}^{\infty}\sqrt{(}N_{1n}^{TE})D_n(1+\Gamma)\ddot{u}_{1n}^{TE}(k_\Omega,\Theta) \tag{5.60}$$

The integral $\ddot{u}_{1n}^{TE}(k_\Omega,\Theta)=\int\int_{S_{ap}}\left[\left(\frac{1}{\rho}J_1(\beta_{\rho,(1,n)}\rho)\sin^2\phi+\beta_{\rho,(1,n)}J_1'(\beta_{\rho,(1,n)}\rho)\cos^2\phi\right)\right]e^{k_\Omega\rho\cos(\phi-\Theta)}\rho d\rho d\phi$.

The integral can be found using a similar approach as $\ddot{o}_{1n}^{TE}$ using Bessel function properties. Therefore,

$$\ddot{u}_{1n}^{TE}(k_\Omega,\Theta)=\pi\beta_{\rho(1,n)}\left[I_{00}^{1,n}(k_\Omega)+I_{22}^{1,n}(k_\Omega)\cos(2\Theta)\right] \tag{5.61}$$

Where,

$$I_{00}^{1,n}(k_\Omega)=\int_0^R \rho J_0(\beta_{\rho(1,n)})J_0(k_\Omega\rho)d\rho \tag{5.62}$$

This can also be evaluated using the Lommel's integral of the form (3.85).

Finally applying equations of the form (in terms of k_Ω and Θ)(5.55) and (5.60) into the expression of $<2,2>$ and finally using it in the equation for the aperture admittance in (5.49), we have,

$$y_{ap}Y_{11}^{TE}=\Xi_{1,1}^{xx}+\Xi_{1,1}^{yy}+\Xi_{1,1}^{xy}+2\sum_{n=2,3,..}^{\infty}(\Xi_{1,n}^{xx}+\Xi_{1,n}^{yy}+\Xi_{1,n}^{xy})D_n+\sum_{m=2,3,..}^{\infty}\sum_{n=2,3,..}^{\infty}(\Xi_{m,n}^{xx}+\Xi_{m,n}^{yy}+\Xi_{m,n}^{xy})D_mD_n+\sum_{n=2,3,..}^{\infty}D_n^2Y_{1,n}^{TE} \tag{5.63}$$

Where,

$$\Xi_{m,n}^{xx}=\Upsilon(m,n)\int\int_{-\infty}^{\infty}\frac{k^2-k_\Omega^2\sin^2(\Theta)}{\omega\mu k_z(k_\Omega)}\pi^2\sin^2(2\Theta)I_{22}^{1,n}(k_\Omega)I_{22}^{1,m}(k_\Omega)k_\Omega dk_\Omega d\Theta \tag{5.64}$$

$$\Xi_{m,n}^{yy}=\Upsilon(m,n)\int\int_{-\infty}^{\infty}\frac{k^2-k_\Omega^2\cos^2(\Theta)}{\omega\mu k_z(k_\Omega)}\pi^2\left[I_{00}^{1,n}(k_\Omega)+I_{22}^{1,n}(k_\Omega)\cos(2\Theta)\right]\left[I_{00}^{1,m}(k_\Omega)+I_{22}^{1,m}(k_\Omega)\cos(2\Theta)\right]k_\Omega dk_\Omega d\Theta \tag{5.65}$$

$$\Xi_{m,n}^{xy}=\Upsilon(m,n)\int\int_{-\infty}^{\infty}\frac{2k_\Omega^2\sin(\Theta)\cos(\Theta)}{\omega\mu k_z(k_\Omega)}\pi^2\sin(2\Theta)I_{22}^{1,n}(k_\Omega)\left[I_{00}^{1,m}(k_\Omega)+I_{22}^{1,m}(k_\Omega)\cos(2\Theta)\right]k_\Omega dk_\Omega d\Theta \tag{5.66}$$

Where,

$$\Upsilon(m,n)=\frac{\sqrt{N_{1,n}^{TE}N_{1,m}^{TE}}\beta_{\rho,(1,n)}\beta_{\rho,(1,m)}}{4\pi^2} \tag{5.67}$$

For small variation of the fields at the aperture it is assumed that the changes of y_{ap} is small with respect to D_n. Therefore,

$$\frac{\partial y_{ap}}{\partial D_n}=0 \tag{5.68}$$

Equation (5.63) can be written in a matrix form as,

$$y_{ap}Y_{11}^{TE} = \tau_{1,1} + 2\begin{bmatrix} D_2 & D_3 & D_4 & \dots & D_\infty \end{bmatrix}\begin{bmatrix} \tau_{1,2} \\ \tau_{1,3} \\ \tau_{1,4} \\ . \\ \tau_{1,\infty} \end{bmatrix} + \begin{bmatrix} D_2 & D_3 & D_4 & \dots D_\infty \end{bmatrix}\begin{bmatrix} \tau_{2,2} + Y_{1,2}^{TE} & \tau_{2,3} & \dots & \tau_{2,\infty} \\ \tau_{3,2} & \tau_{3,3} + Y_{1,3}^{TE} & \dots & \tau_{3,\text{inf}} \\ . & & & \\ \tau_{\infty,2} & \tau_{\infty,3} & \dots & \tau_{\infty,\infty} + Y_{1,\infty}^{TE} \end{bmatrix}\begin{bmatrix} D_2 \\ D_3 \\ D_4 \\ . \\ D_\infty \end{bmatrix} \tag{5.69}$$

Where,

$$\tau_{m,n} = \Xi_{m,n}^{xx} + \Xi_{m,n}^{yy} + \Xi_{m,n}^{xy} \tag{5.70}$$

Taking the derivative with respect to D_n and equating it to zero gives rise to,

$$\begin{bmatrix} \tau_{2,2} + Y_{1,2}^{TE} & \tau_{2,3} & \dots & \tau_{2,\infty} \\ \tau_{3,2} & \tau_{3,3} + Y_{1,3}^{TE} & \dots & \tau_{3,\text{inf}} \\ . & & & \\ \tau_{\infty,2} & \tau_{\infty,3} & \dots & \tau_{\infty,\infty} + Y_{1,\infty}^{TE} \end{bmatrix}\begin{bmatrix} D_2 \\ D_3 \\ D_4 \\ . \\ D_\infty \end{bmatrix} = \begin{bmatrix} -\tau_{1,2} \\ -\tau_{1,3} \\ -\tau_{1,4} \\ . \\ -\tau_{1,\infty} \end{bmatrix} \tag{5.71}$$

The inversion in equation (5.71) yields the D_n excitation coefficients. After D_n is known, y_{ap} can be found as (using equation (5.68) and (5.69)),

$$y_{ap}Y_{11}^{TE} = \tau_{1,1} + \begin{bmatrix} D_2 & D_3 & D_4 & \dots & D_\infty \end{bmatrix}\begin{bmatrix} \tau_{1,2} \\ \tau_{1,3} \\ \tau_{1,4} \\ . \\ \tau_{1,\infty} \end{bmatrix} \tag{5.72}$$

Using the y_{ap} the reflection coefficient Γ can be found using (5.23).

The expressions for $\tau_{m,n}$ also can be simplified using integral over cylindrical system (k_Ω and Θ). After separating the expressions for Θ and integrating it from 0 to 2π, we can find the integral in terms of only k_Ω as,

$$\tau_{m,n} = \Xi_{m,n}^{xx} + \Xi_{m,n}^{yy} + \Xi_{m,n}^{xy} \tag{5.73}$$

$$\tau_{m,n} = \int_0^\infty \frac{\sqrt{N_{1,n}^{TE}N_{1,m}^{TE}}\beta_{\rho(1,n)}\beta_{\rho(1,n)}\pi}{4\omega\mu k_z(k_\Omega)}\Big((2k_0^2 - k_\Omega^2)(I_{00}^{1,n}(k_\Omega)I_{00}^{1,m}(k_\Omega) + I_{22}^{1,n}(k_\Omega)I_{22}^{1,m}(k_\Omega)) - \frac{k_\Omega^2}{2}(I_{00}^{1,n}(k_\Omega)I_{22}^{1,m}(k_\Omega) + I_{22}^{1,n}(k_\Omega)I_{00}^{1,m}(k_\Omega))\Big)k_\Omega dk_\Omega$$

where,

$$k_z(k_\Omega) = -j\sqrt{-(k^2 - k_\Omega^2)} \tag{5.74}$$

For example, for $\tau_{1,1}$, the mutual admittance between the fundamental mode with itself (TE_{11}),

$$\tau_{1,1} = \mathrm{Z}_{11,11} \int_0^\infty \frac{1}{k_z(k_\Omega)} \Big((2k_0^2 - k_{k_\Omega}^2) \Big[(I_{00}^{1,1}(k_\Omega))^2 + (I_{22}^{1,1}(k_\Omega))^2 \Big] - k_\Omega^2 I_{00}^{1,1}(k_\Omega) I_{22}^{1,1}(k_\Omega) \Big) k_\Omega dk_\Omega \quad (5.75)$$

Where $\mathrm{Z}_{11,11}$ is a constant and defined as,

$$\mathrm{Z}_{11,11} = \frac{N_{1,1}^{TE} \beta_{\rho(1,1)}^2 \pi}{4\omega\mu} \quad (5.76)$$

Where I_{00}^{11} and I_{22}^{11} are given by (Lommel's integrals),

$$I_{00}^{11} = R^2 \frac{\beta_{\rho(1,1)} J_1(\beta_{\rho(1,1)} R) J_0(k_\Omega R) - k_\Omega J_0(\beta_{\rho(1,1)} R) J_1(k_\Omega R)}{\beta_{\rho(1,1)}^2 - k_\Omega^2} \quad (5.77)$$

$$I_{22}^{11} = R^2 \frac{-\beta_{\rho(1,1)} J_1(\beta_{\rho(1,1)} R) J_2(k_\Omega R) + k_\Omega J_2(\beta_{\rho(1,1)} R) J_1(k_\Omega R)}{\beta_{\rho(1,1)}^2 - k_\Omega^2} \quad (5.78)$$

Furthermore, as from chapter 3 we know that there are Lommel's integral analytical expressions when the argument to the two Bessel function expressions are same, those expressions can be used at the locality of the pole locations in the above integral expression ($\tau_{m,n}$).

$$I_{00,(\beta_{\rho(1,1)}=k_\Omega)}^{11} = \frac{1}{2} R^2 ([J_0(\beta_{\rho(1,1)} R)]^2 + [J_1(\beta_{\rho(1,1)} R)]^2) \quad (5.79)$$

$$I_{22,(\beta_{\rho(1,1)}=k_\Omega)}^{11} = \frac{1}{2} R^2 ([J_2(\beta_{\rho(1,1)} R)]^2 - J_1(\beta_{\rho(1,1)} R) J_3(\beta_{\rho(1,1)} R)) \quad (5.80)$$

Hence, the integrals can be done in 3 parts. One is from 0 to $\beta_{\rho(1,1)} - \epsilon$, then from $\beta_{\rho(1,1)} - \epsilon$ to $\beta_{\rho(1,1)} + \epsilon$ and finally from $\beta_{\rho(1,1)} + \epsilon$ to ∞ (where ϵ is a very small quantity).

While doing the integral, it is also important not to cross the branch cut of the square root function $k_z(k_\Omega)$. This multi-valued square root function is plotted in figure 5.11 (both real and imaginary quantities). It is seen that the real part has a branch cut because there is a immediate change of sign when the real line is crossed. The imaginary quantity is always negative. In Riemann sheet convention, with the expression $k_z(k_\Omega) = -j\sqrt{-(k^2 - k_\Omega^2)}$ the bottom Riemann sheet is considered [25].

The integration path, branch cut and branch points for this K space integral is shown in figure 5.12. Here, it is interesting to note that as in Mishustin integrals, here also the integral from 0 to k_0 yields the real part of the admittance where the integral from k_0 to ∞ yields the imaginary part. Clearly, the K space integrals have advantages over the Mishustin integrals as they also can compute the mutual admittance between different eign-modes in the waveguide. Furthermore, they can be more accurate than the Mishustin's integral because the poles at $|k_\Omega| = \beta_{\rho(1,1)}$ (same as $\eta = \frac{\mathrm{X}'(1,1)}{k_0 R}$ in Mishustin's case) can be avoided by using the Lommel's integrals as a step function. Similarly in the case of mutual admittance when ($m \neq n$), the poles can be avoided at the points $|k_\Omega| = \beta_{\rho(1,m)}$ and $|k_\Omega| = \beta_{\rho(1,n)}$.

5.3.5. Results related to the reflection at the aperture free-space transition

In this section the results of the reflection coefficient (Γ), aperture admittance (y_{ap}), higher order mode excitation (D_m) at the aperture free-space boundary of a circular cross section waveguide when excited with only the fundamental mode (TE_{11}).

Higher order modes at the aperture

The higher order mode excitation are shown in figure 5.13 as a function of the ratio of diameter to the wavelength ($\frac{2R}{\lambda_0}$) of operation and number of higher order modes (TE_{12}, TE_{13} and so on). The far away the higher order mode in terms of cut-off frequency, the lower is the excitation. This trend is expected at the aperture. Therefore, for analysis, only a few number of modes can be considered to have reduced time complexity and better accuracy numerically.

Normalized Aperture Admittance

Figure 5.14 shows the normalized aperture admittance ($y_{ap} = g_{in} - jb_{in}$). The g_{in} is the conductance and b_{in} is the susceptance. The susceptance is inductive and that is also expected at the aperture [7]. The K space integrals are plotted in two different ways. The first is just the aperture admittance given that there are no higher order modes excited at the aperture ($\frac{\tau_{1,1}}{Y_{11}^{TE}}$). The second is when higher order modes are included in the analysis y_{ap}. Both are compared with the Mishustin integrals which only considers the fundamental mode reflection at the aperture. The trend of all of the above mentioned parameters look very similar to one another when plotted as a function of the ratio of diameter to the wavelength of operation. It is very interesting to notice that the more the ratio of the diameter to wavelength ($\frac{2R}{\lambda_0}$), the closer g_{in} to unity and b_{in} to zero. This suggests that the aperture admittance approaches free-space wave admittance when the waveguide operates at a frequency which is far away from the cut-off frequency of the fundamental mode yet below the cut-off frequency of the next higher order mode. This is also expected at the aperture. Therefore, at higher frequencies, the waveguide tends to be perfectly matched to free-space.

Reflection coefficient

Figure 5.15 and 5.16 shows the reflection coefficient magnitude and phase respectively Γ with respect to the ratio of diameter to the wavelength $\frac{2R}{\lambda_0}$. As reflection coefficient (Γ) is directly related to the normalized aperture admittance as $\Gamma = \frac{1-y_{ap}}{1+y_{ap}}$, it is also seen here that the waveguide becomes more nearly matched to free-space atg higher frequencies (higher ratio of diameter to wavelength). The reflection coefficient is also compared with Mishustin integrals. Here, also like the normalized aperture admittance, K space integrals are considered in two different ways. One with only the fundamental mode reflection ($\Gamma = \frac{1-\frac{\tau_{1,1}}{Y_{11}^{TE}}}{1+\frac{\tau_{1,1}}{Y_{11}^{TE}}}$) and another way with higher order mode excitation $\Gamma = \frac{1-y_{ap}}{1+y_{ap}}$.

5.4. Near field and far-field of one open ended waveguide with metal flange

5.4.1. Near Fields open ended circular waveguide with metal flange

After the determination of the parameters Γ and D_m, we can find the field distribution on the aperture of an open ended waveguide.

In the case of the circular cross-section waveguide, as the Γ values are negative, the electric field patterns should have a reduced value than that of an infinitely long waveguide (a waveguide with an absorbing boundary condition at the aperture). It shows that the contribution of higher order modes at the aperture is also reduced by a factor $1 + \Gamma$. Therefore, the overall electric field should have

reduced amplitudes at the aperture. However, as the magnetic fields have a $1-\Gamma$ in the expression for fundamental mode, the fundamental mode amplitude increases and therefore becomes dominant. Therefore, the magnetic field distribution should have greater values at the aperture than that of an infinitely long waveguide (absorbing condition). In the case of magnetic fields, the higher order modes also are not dominant because of the factor $1+\Gamma$. The near-field patterns of a circular open ended waveguide of radius 2[cm] at a frequency of 5 GHz is shown in figure 5.18 with FEKO results. At this frequency this waveguide only supports TE11 mode internally (fundamental mode).

The FEKO configuration for the open ended waveguide problem (finite length) is shown in figure 5.17. In FEKO, for the open ended waveguide problem, there is a ground plane used at the aperture of radius 70 [cm] for all the below mentioned results. Surrounding the ground plane, there is a magnetic coaxial wall of thickness 10 [cm] and height 10 [cm] to ensure minimum reflection from the edge of the ground plane. In FEKO, for the infinite length waveguide problem, the far end of the waveguide is terminated with another waveguide port with no excitation to the fundamental mode (TE_{11}) to have a absorbing boundary condition.

The right column figures of the figure 5.18 is taken from FEKO. It is seen that the magnetic field distribution indeed has greater values when it is open to free-space than when it is infinitely long (with absorbing boundary conditions). The values are shown at one point on the plots. FEKO result values are close to the one which is derived from the spectral integral equation method mentioned in the thesis. Similarly, the electric field values are lesser in the case of open ended waveguide than when the waveguide is of infinite length. These values also match the values obtained from FEKO.

However, towards the edge of the waveguide cross section, FEKO results look a little different for the case of open ended waveguide (finite length). This is due to the fact that FEKO uses MoM (Method of Moments) solver and therefore assumes that the entire structure is filled with discrete triangles and therefore, it is not a perfect circle. Apart from that, at the boundary, the edge of the waveguide produces some fringing fields or diffraction fields which interfere with the pattern. The fringe field pattern near the edge is visible in the FEKO plots. These fields change their pattern when the size of the ground plane in the FEKO simulations change its dimensions.

5.4.2. Far-fields of an open ended circular waveguide with metal flange

The far-fields of the same configuration is plotted in figure 5.19. The far-field plot has both the pattern for the finite waveguide and the infinite length waveguide case. The legend which says FEKO NF MATLAB FF are the far-field plots obtained in MATLAB with numerical integration over the near-fields those are obtained from FEKO. Rest of the plots are done using the spectrum analytical functions mentioned in (5.58) and (5.61). For these plots the values of Γ, D_m are used from the K space integrals. For the infinite waveguide case, Γ was kept as zero and D_m also kept as zero. The analytical spectrum expressions for the far-fields, when applied in MATLAB compute the far-fields in seconds. Therefore, it is computationally very efficient. On the other hand, the far-fields obtained from the near fiels of FEKO with the numerical FFT technique mentioned in equation (5.13) and (5.14) take up to three to four minutes (for 180 points on azimuth and 100 points in the radial direction) for the Fourier transform.

Although the near-field patterns are a little different as depicted in figure 5.18, the far-fields show promising resemblance. This is due to the fact that far-fields are forgiving. Far-field is an integral quantity (average) over the near-field distribution. Therefore, small differences in near-fields are forgiven in the case of far-field computation. It can be seen that FEKO results are very close to the MATLAB ones, both for finite and infinite length waveguide cases. There is a clear difference between the patterns of a finite and an infinite length waveguide. This is due to the result of reflection at the aperture free-space transition.

5.5. Conclusions

In this chapter first the theoretically infinite length (or perfectly matched) waveguide horn is discussed for its near-field and far field patterns. The MM software is used to formulate the near-field patterns and spatial Fourier transform was used to determine the far fields of the aperture near-fields obtained from the MM software. The patterns implemented in MATLAB were compared with equivalent FEKO simulations for a two waveguide/ five waveguide and a conical waveguide structure. The results came out be very close to each other. In FEKO simulations, the far end of the waveguide is usually closed with an absorbing port to mimimc the same conditions (infinite waveguide or perfectly matched conditions). In the later half of the chapter, the reflection from free space is considered. Various approaches were discussed and the Rumsey's reaction concept was used to develop a numerical integral tool to determine the reflection from the aperture free space boundary. This result of aperture admittance and reflection coefficients were compared with Mishustin's integrals [19]. The near and far fields from finite length open cylindrical waveguides were then compared with FEKO results. The results have good agreement with each other. The results show that the differences between aperture fields for an open ended waveguide and a perfectly matched waveguide predicted using the MATLAB implementation derived in this chapter, are in excellent agreement.

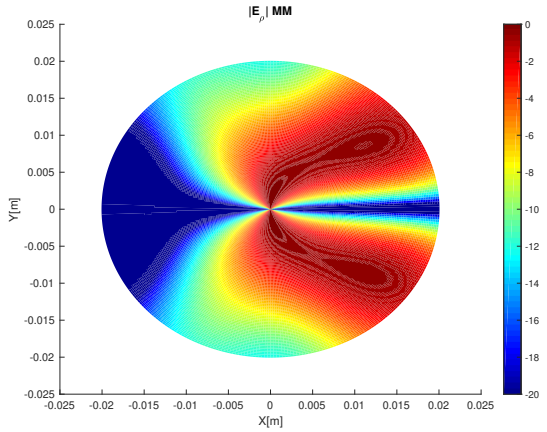

(a) E_ρ MM

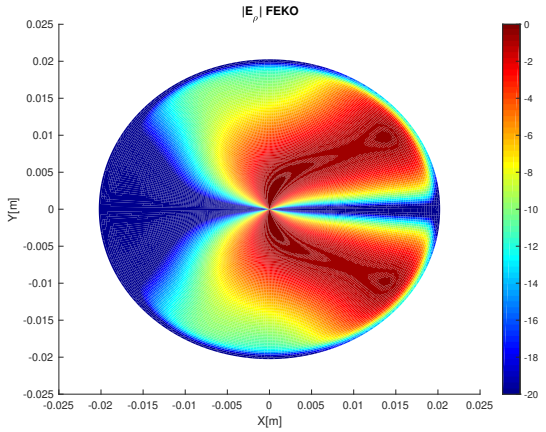

(b) E_ρ FEKO

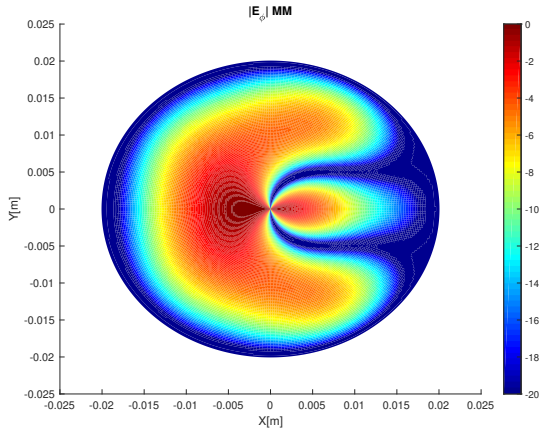

(c) E_ϕ MM

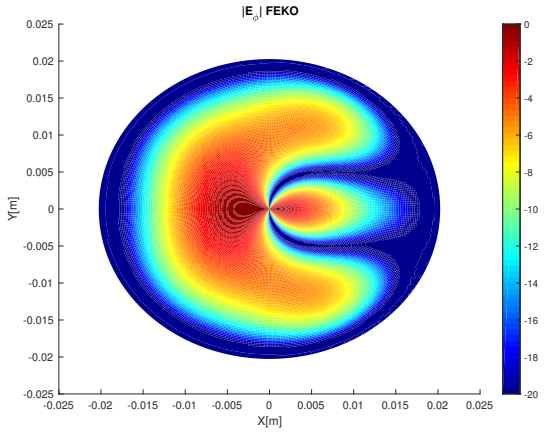

(d) E_ϕ FEKO

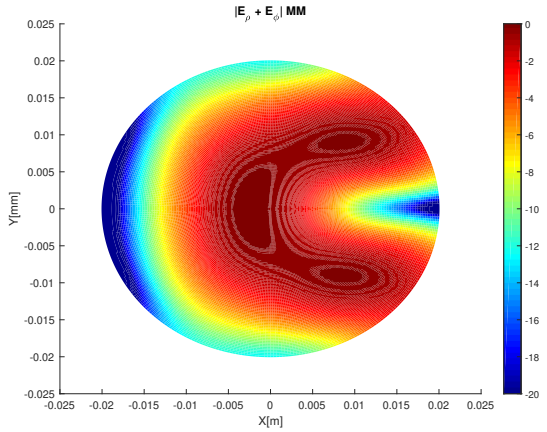

(e) $E_\phi + E_\rho$ (Tangential) MM

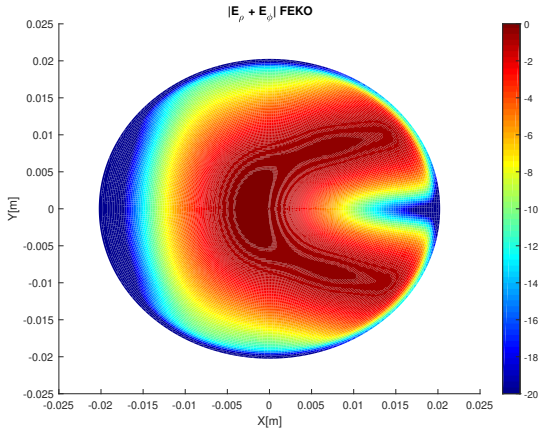

(f) $E_\phi + E_\rho$ (Tangential) FEKO

Figure 5.2: Aperture electric field at 14 GHz for the 2 waveguide problem (perfectly matched) (10 modes propagating on both waveguides) - Normalized in dB.

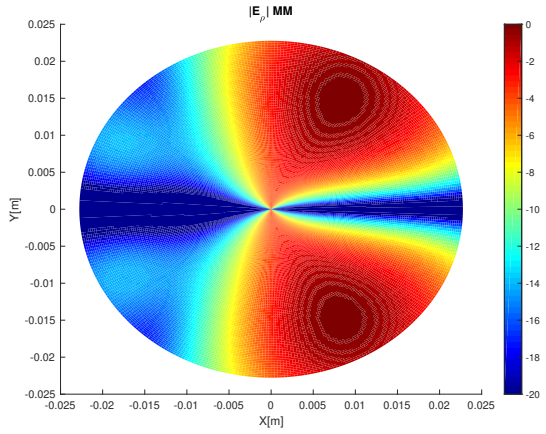

(a) E_ρ MM

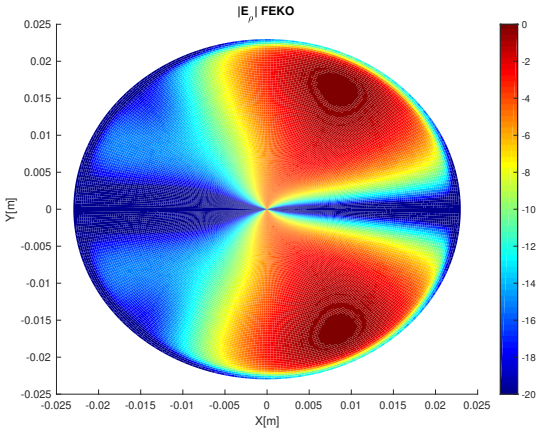

(b) E_ρ FEKO

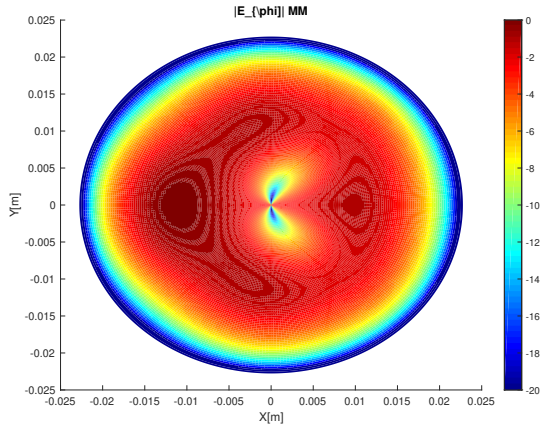

(c) E_ϕ MM

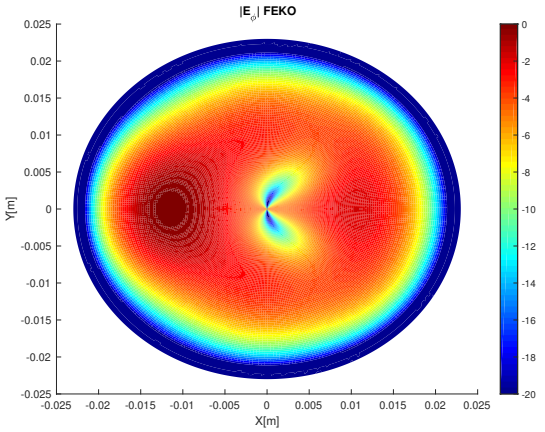

(d) E_ϕ FEKO

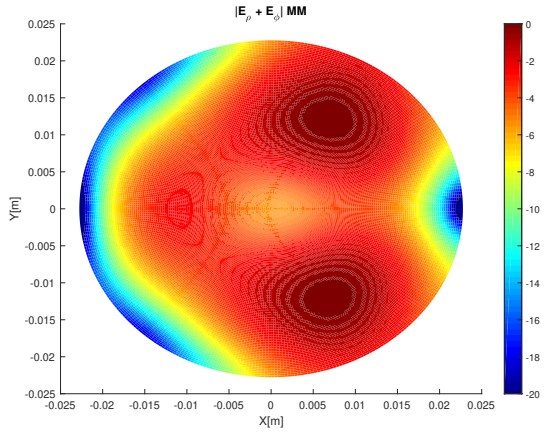

(e) $E_\phi + E_\rho$ (Tangential) MM

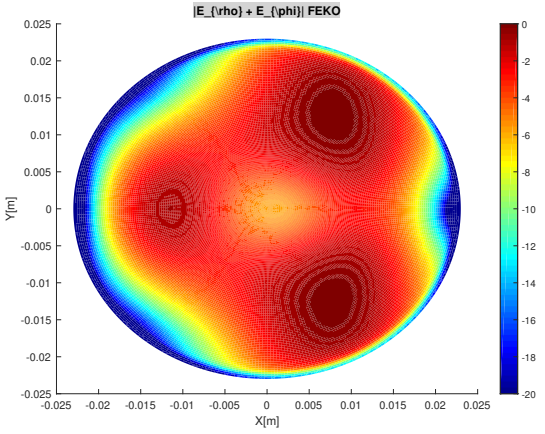

(f) $E_\phi + E_\rho$ (Tangential) FEKO

Figure 5.3: Aperture electric field at 14 GHz for the 5 waveguide problem (perfectly matched) (10 modes propagating on the first waveguide and 13 modes on the last waveguide) - Normalized in dB

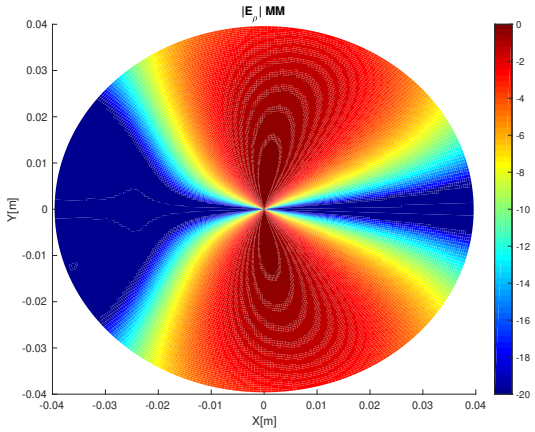

(a) E_ρ MM

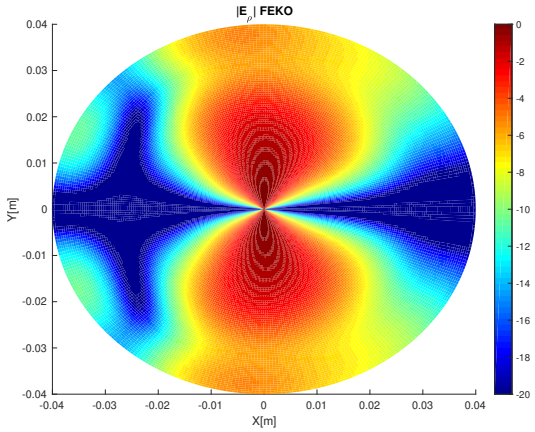

(b) E_ρ FEKO

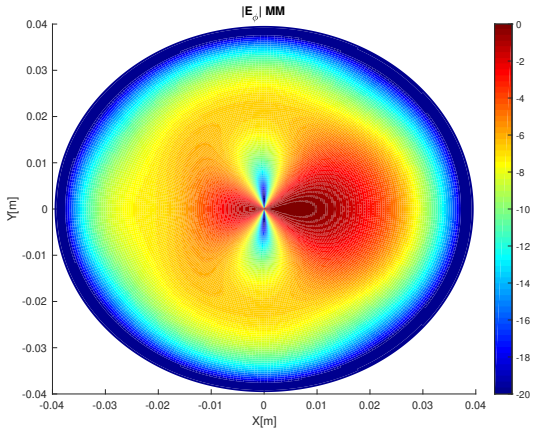

(c) E_ϕ MM

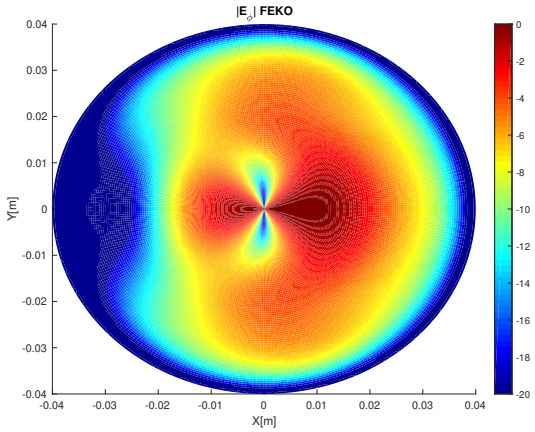

(d) E_ϕ FEKO

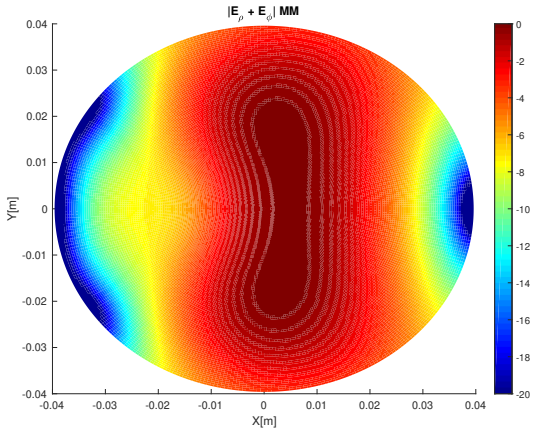

(e) $E_\phi + E_\rho$ (Tangential) MM

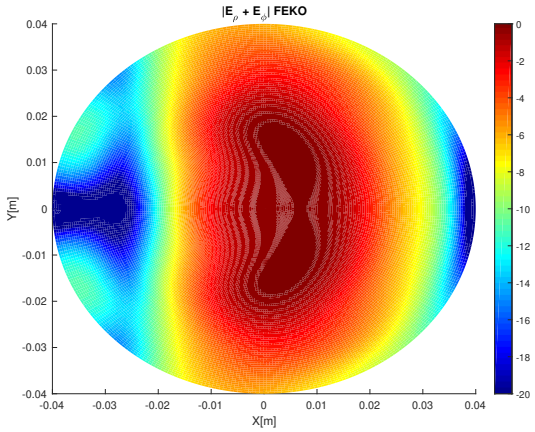

(f) $E_\phi + E_\rho$ (Tangential) FEKO

Figure 5.4: Aperture electric field at 14 GHz for the Cone problem (perfectly matched) (10 modes propagating at the first port and 40 modes propagating at the the second port of waveguide) - Normalized in dB

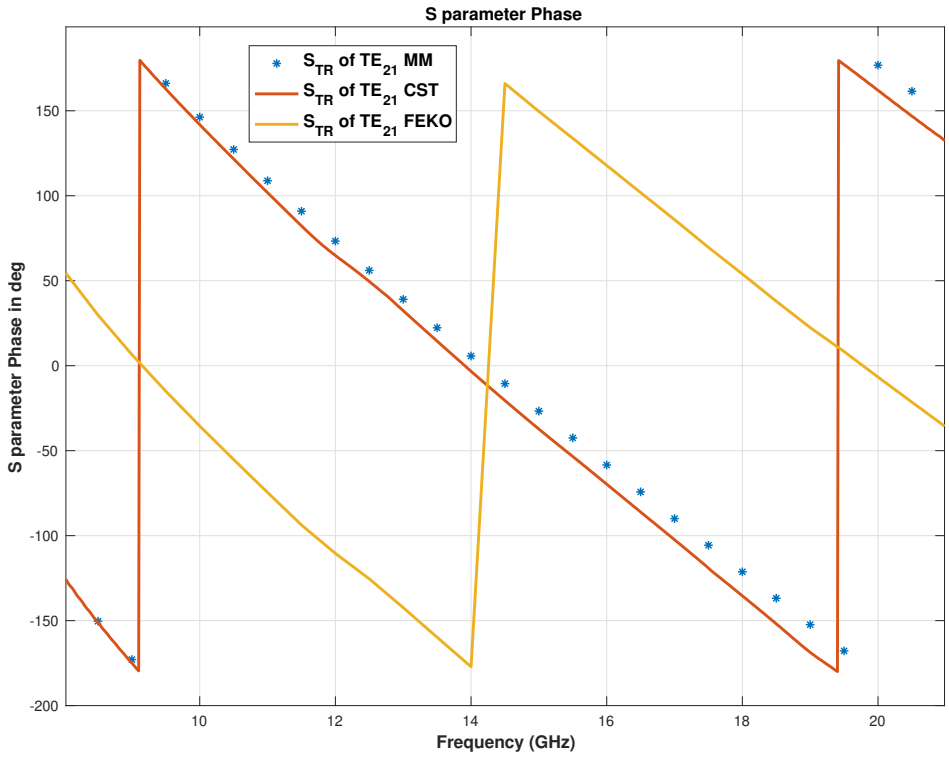

Figure 5.5: TE_{21} Phase in Degree for MM/FEKO and CST for 5 Waveguide Model

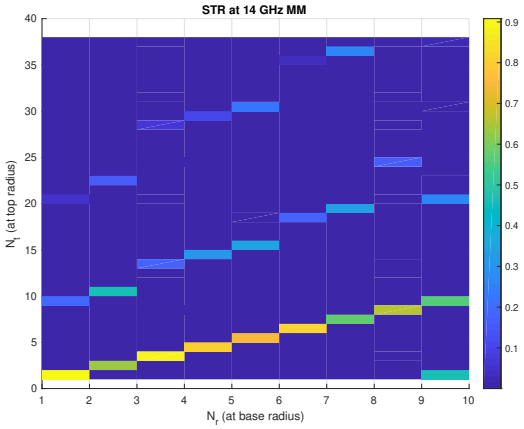

(a) |STR| MM

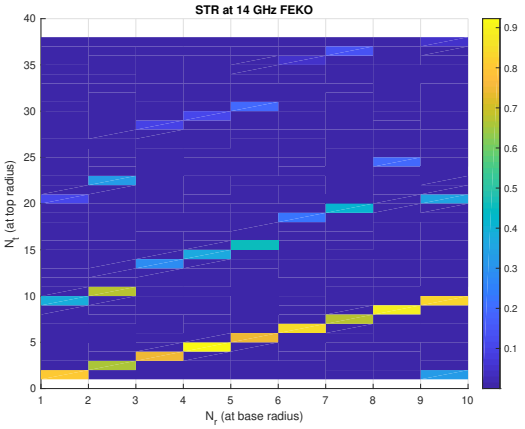

(b) |STR| FEKO

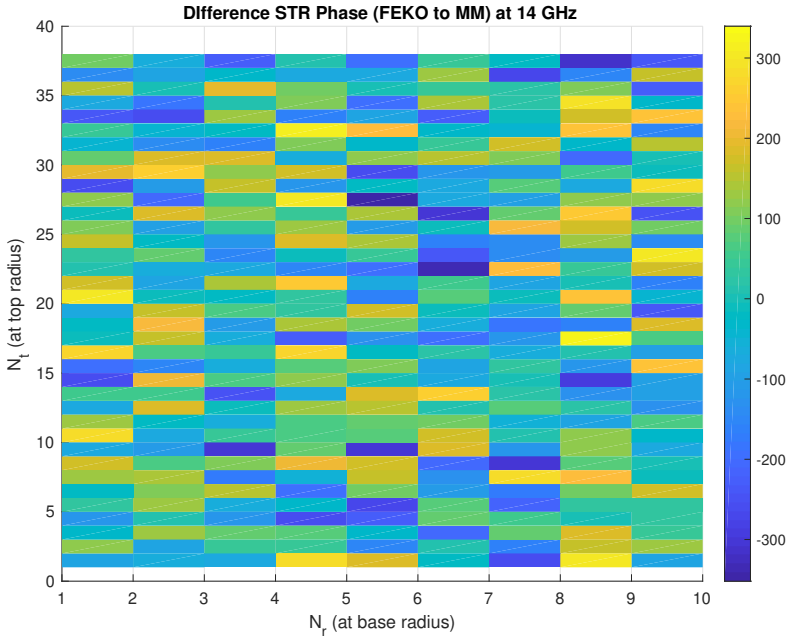

(c) Phase difference |STR(MM) - STR(FEKO)|

Figure 5.6: (1) and (2) - Amplitude of transmission coefficients for Cone model at 14 GHz. The x axis shows modes considered in the first waveguide port(smallest) and Y axis shows the modes of the last waveguide port(largest waveguide). (In the order of their cut off frequencies). (3) - Phase error between FEKO and MM models for Cone structure for transmission coefficient (in degrees).

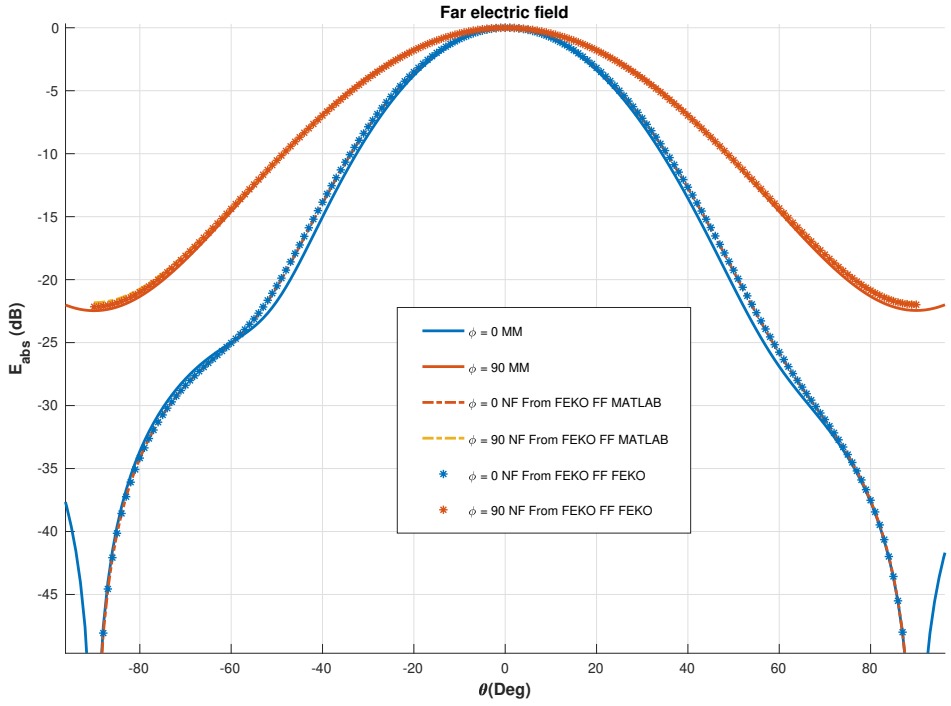

Figure 5.7: Far field from the aperture field of the 2 waveguide structure (Pefectly matched) at 14 GHz Normalized. The plots with MM are from MM software itself. ”NF From FEKO and FF MATLAB” refers to the plots which are computed in MATLAB but the input to those are the Near field patterns drawn from FEKO. ”NF From FEKO FF FEKO” refers to the plots which are computed in FEKO and input to those are the Near field distribution drawn from FEKO in a different experiment.

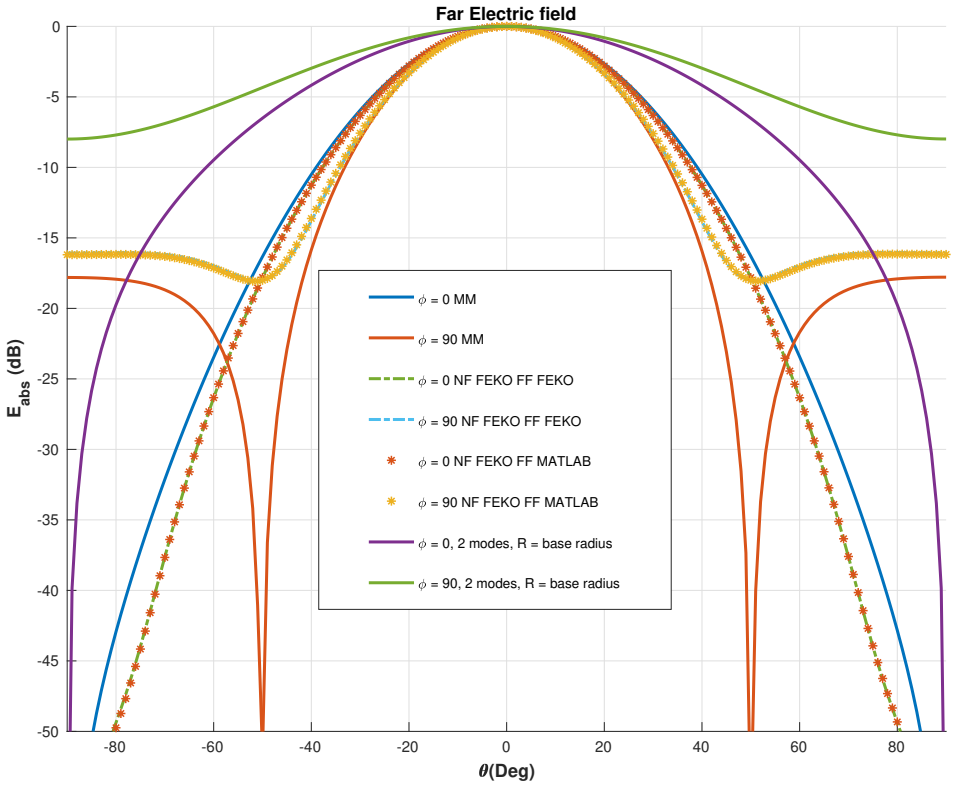

Figure 5.8: Far field from the aperture field of the Cone (Perfectly matched) structure at 6 GHz Normalized. The plots with MM are from MM software itself. ”NF From FEKO and FF MATLAB” refers to the plots which are computed in MATLAB but the input to those are the Near field patterns drawn from FEKO. ”NF From FEKO FF FEKO” refers to the plots which are computed in FEKO and input to those are the Near field distribution drawn from FEKO in a different experiment. The plots which says R=Base radius are the patterns for only one waveguide structure when its radius is the base radius of the cone in the original problem. This is present to show that the the increase in aperture in the horn makes the patterns more narrow for the main beam.

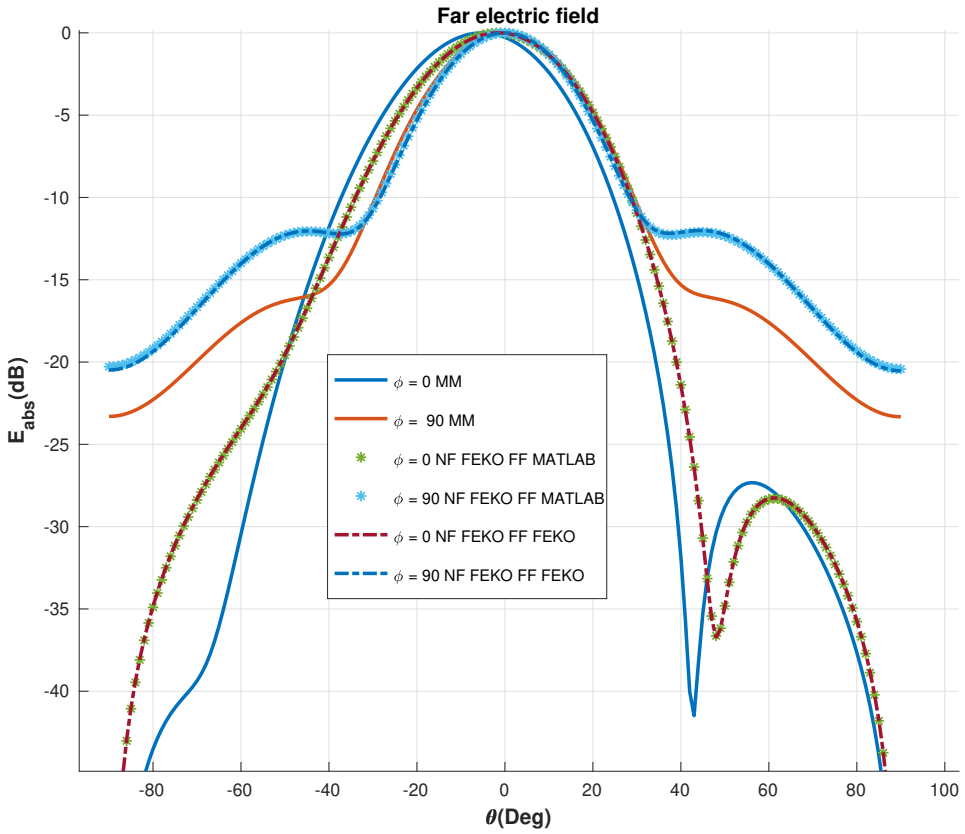

Figure 5.9: Far field from the aperture field of the Cone structure (Perfectly matched) at 7.5 GHz Normalized. The plots with MM are from MM software itself. ”NF From FEKO and FF MATLAB” refers to the plots which are computed in MATLAB but the input to those are the Near field patterns drawn from FEKO. ”NF From FEKO FF FEKO” refers to the plots which are computed in FEKO and input to those are the Near field distribution drawn from FEKO in a different experiment.

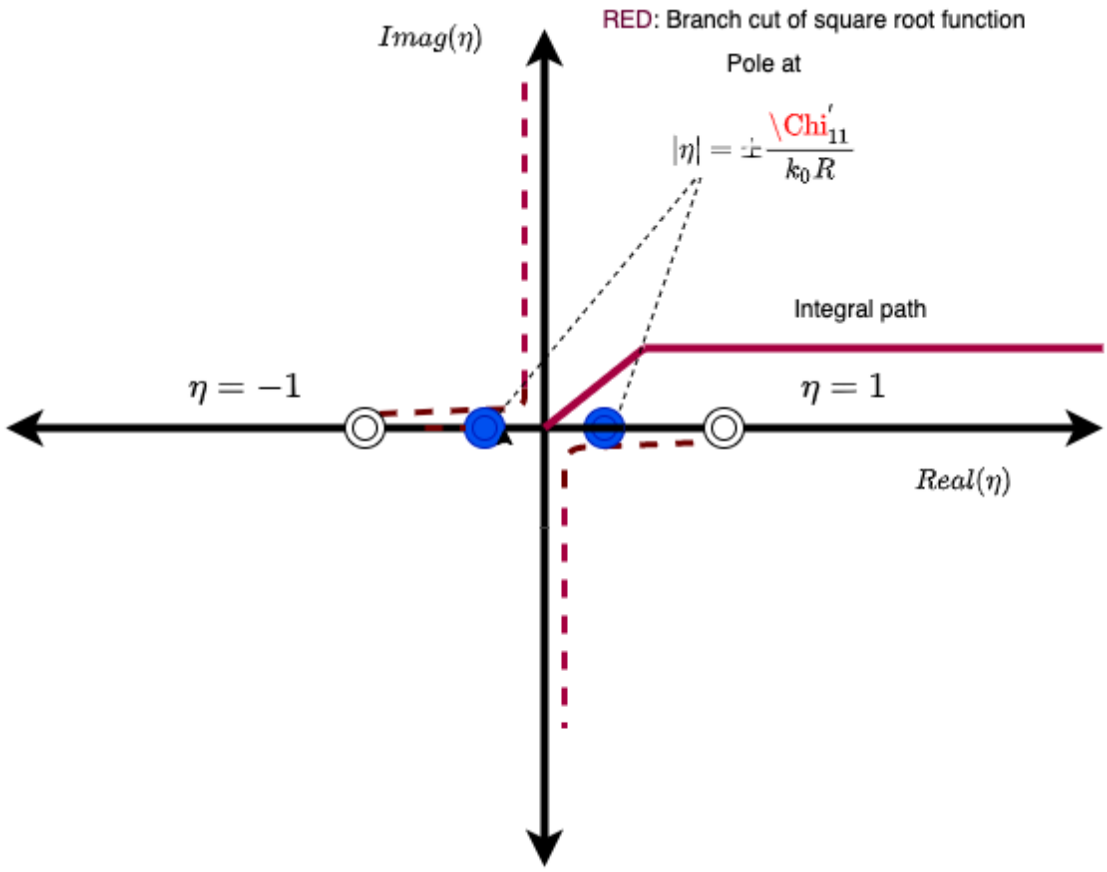

Figure 5.10: Integration path, branch cuts, branch points and poles to integrate Mishustin's integrals

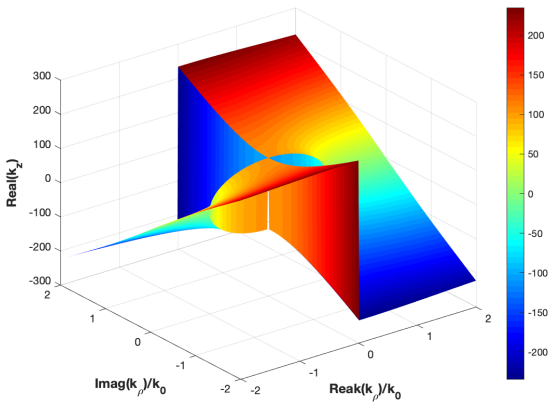

(a) Real part of $-j\sqrt{-(k^2 - k_\Omega^2)}$

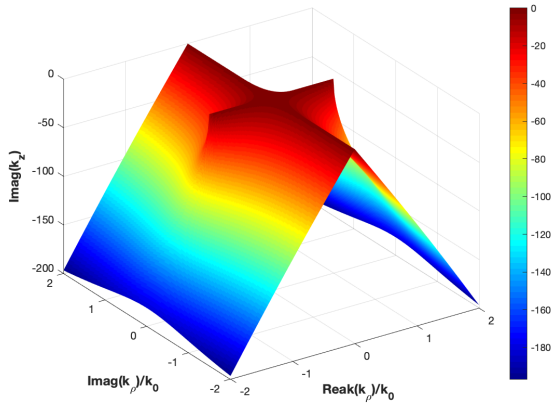

(b) Imaginary part of $-j\sqrt{-(k^2 - k_\Omega^2)}$

Figure 5.11: Real and Imaginary part of k_z

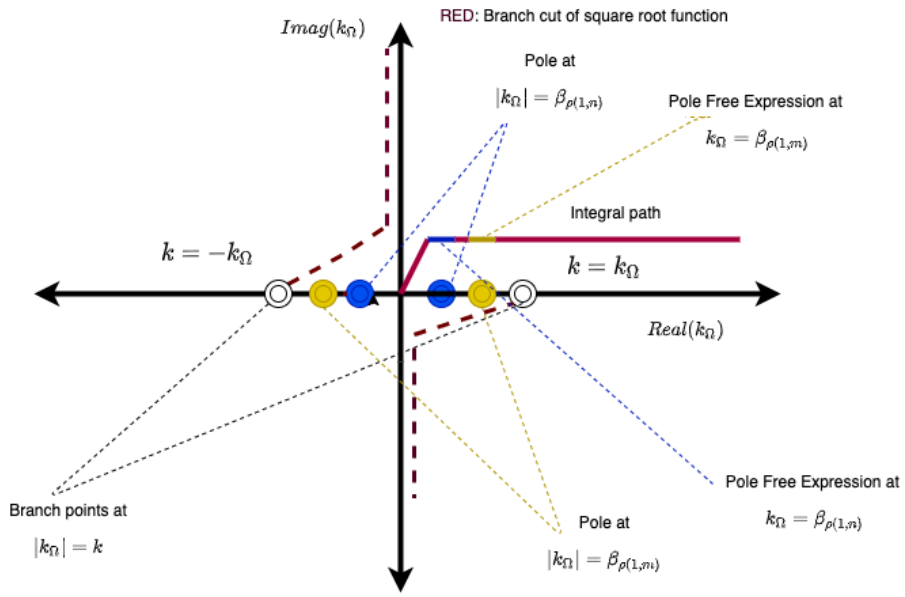

Figure 5.12: Integration path, branch cuts, branch points and poles to integrate K space integral

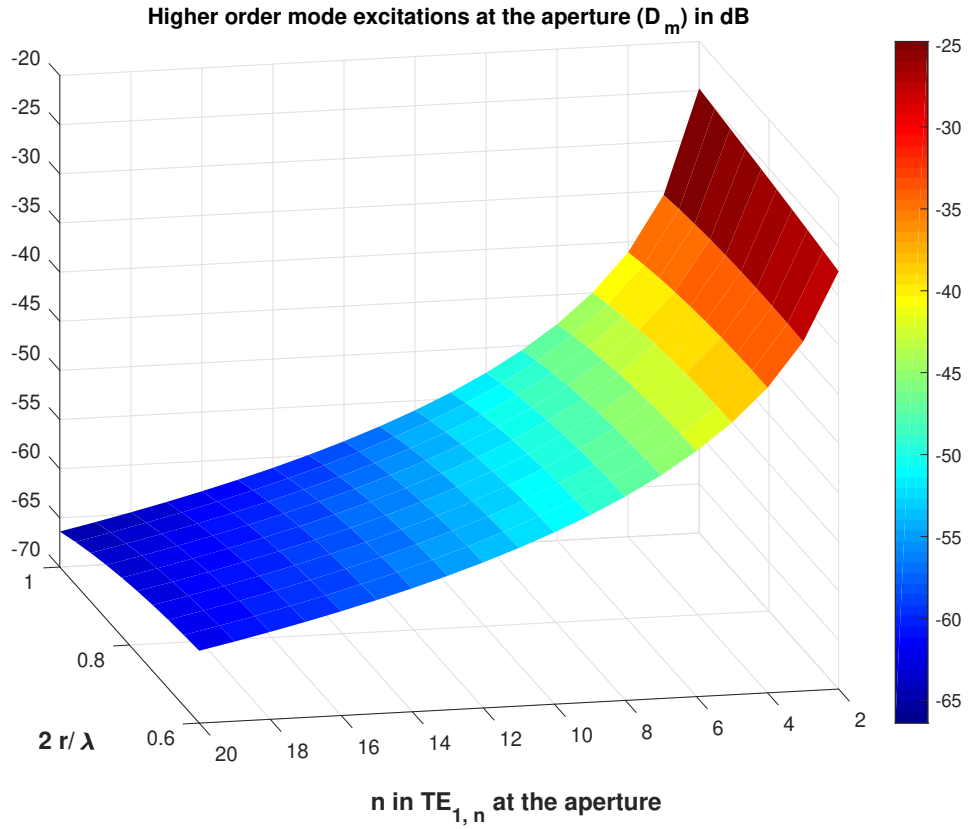

Figure 5.13: Higher order mode excitation at the aperture free-space junction with respect to the ratio of diameter to the wavelength of operation ($\frac{2R}{\lambda}$) and the higher order mode number in dB scale

.

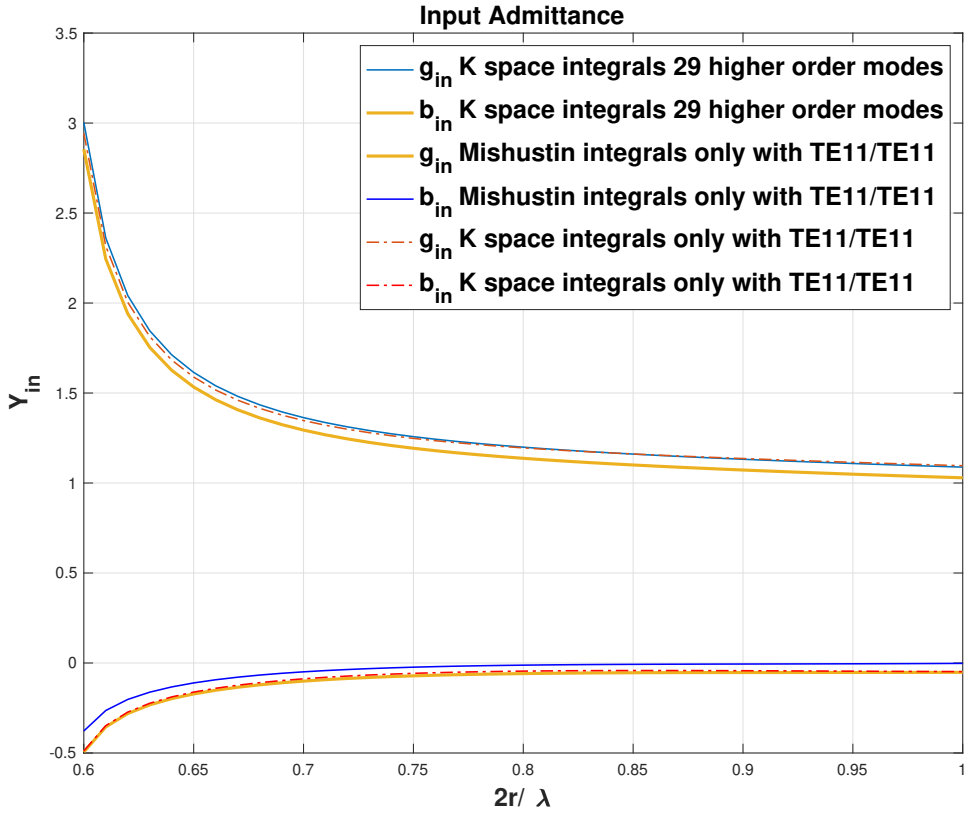

Figure 5.14: Normalized aperture admittance (real part - conductance g_{in} and imaginary part - susceptance b_{in}) with respect to the ratio of diameter to the wavelength of operation ($\frac{2R}{\lambda}$). K space integrals only with TE11/TE11 corresponds to τ_{11} of equation 5.75 (A special case of K space integrasls with higher order modes ($\tau_{m,n}$))

.

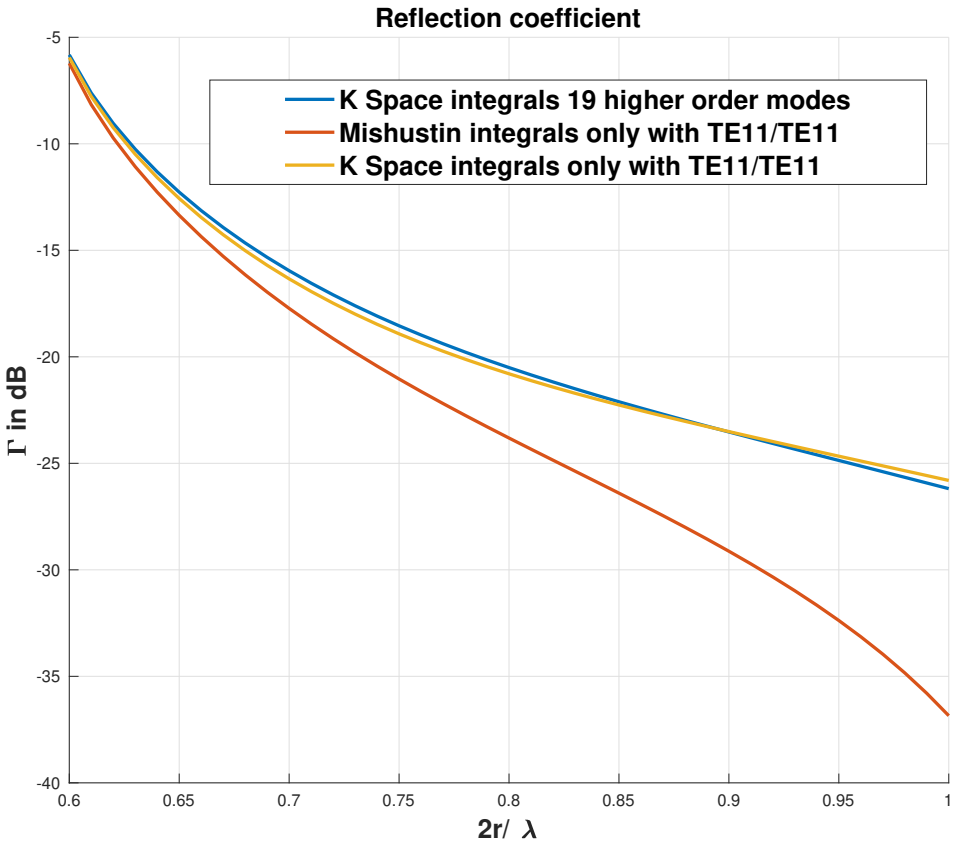

Figure 5.15: Magnitude of reflection coefficient Γ with respect to the ratio of diameter to the wavelength of operation ($\frac{2R}{\lambda}$). K space integrals only with TE11/TE11 corresponds to the use τ_{11} of equation 5.75 (A special case of K space integrasls with higher order modes ($\tau_{m,n}$)).

.

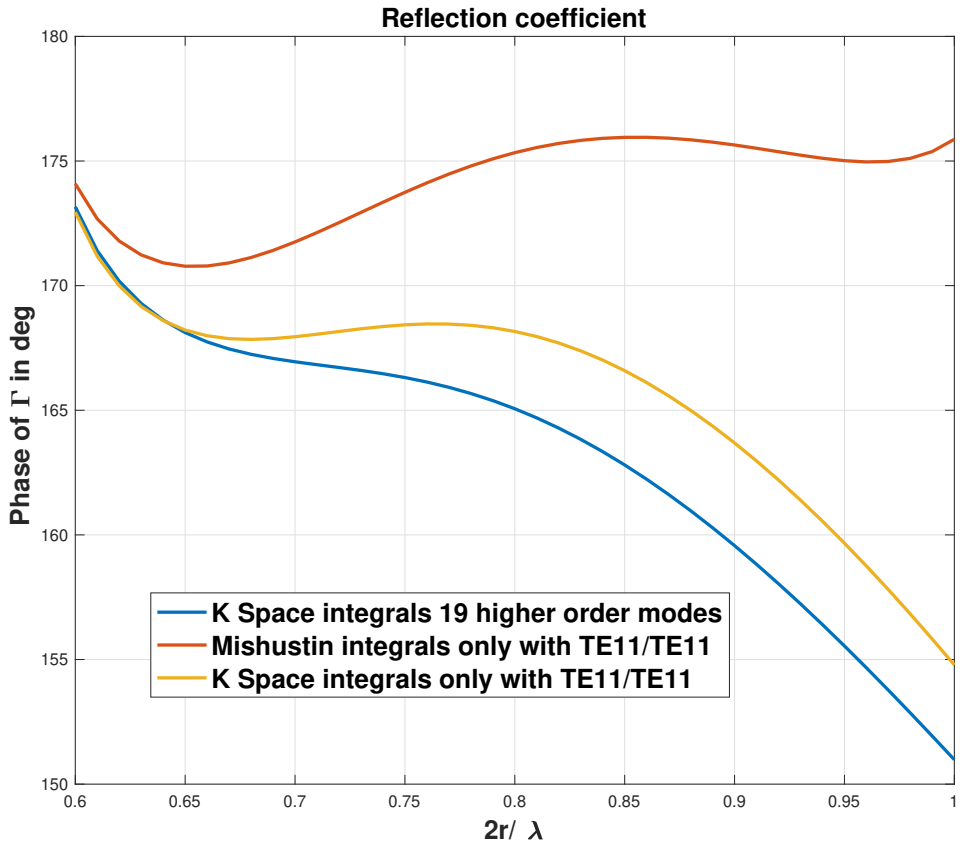

Figure 5.16: Phase of reflection coefficient Γ with respect to the ratio of diameter to the wavelength of operation ($\frac{2R}{\lambda}$). K space integrals only with TE11/TE11 corresponds to the use τ_{11} of equation 5.75 (A special case of K space integrasls with higher order modes ($\tau_{m,n}$)).

.

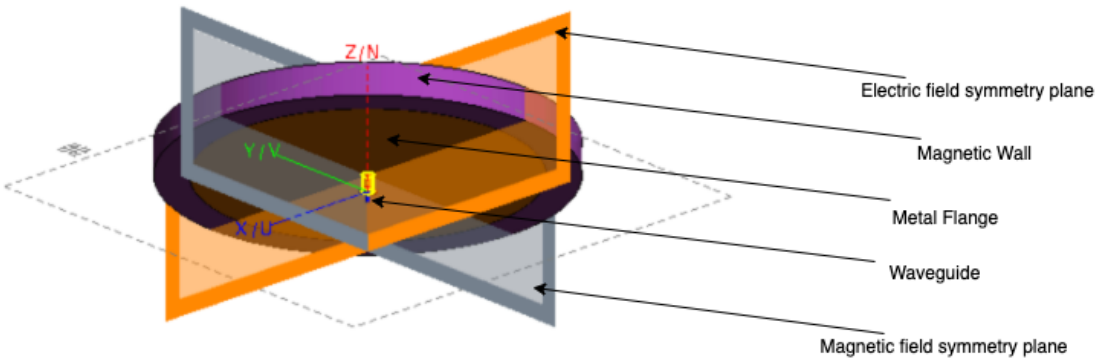

Figure 5.17: FEKO configuration of the open ended waveguide problem with a metal flange of radius 70 [cm]. There is a coaxial magnetic wall surrounding the metal flange of thickness 10 [cm] and height 10 [cm].

.

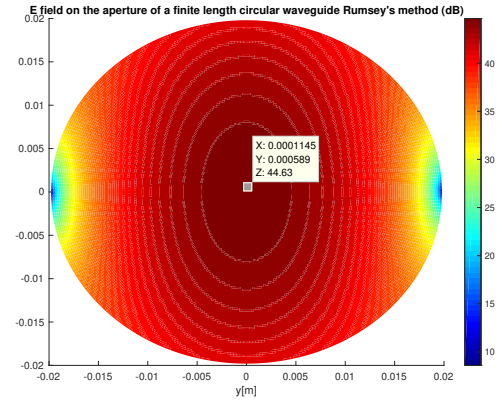

(a) E field at the aperture of a finite length circular waveguide derived with K space integrals

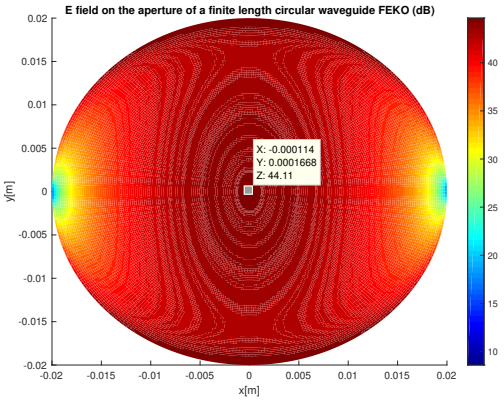

(b) E field at the aperture of a finite length circular waveguide from FEKO

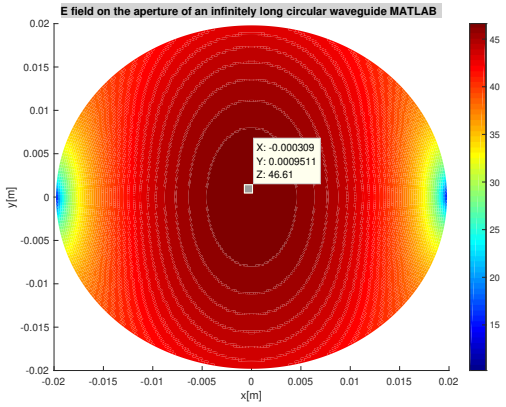

(c) E field at the aperture of a infinite length circular waveguide MATLAB

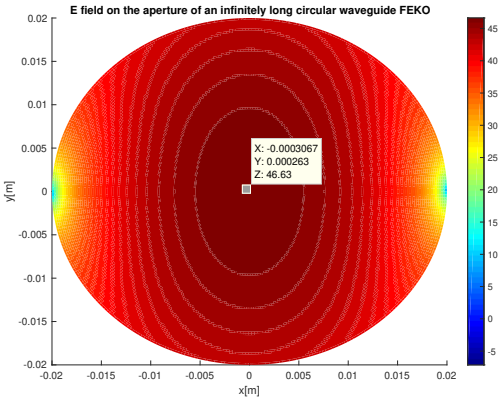

(d) E field at the aperture of a infinite length circular waveguide from FEKO (using absorbing condition)

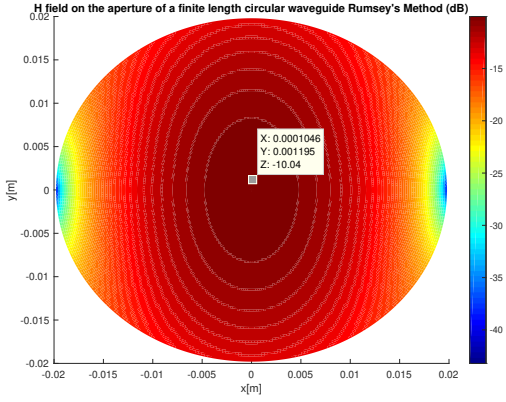

(e) H field at the aperture of a finite length circular waveguide derived with K space integrals

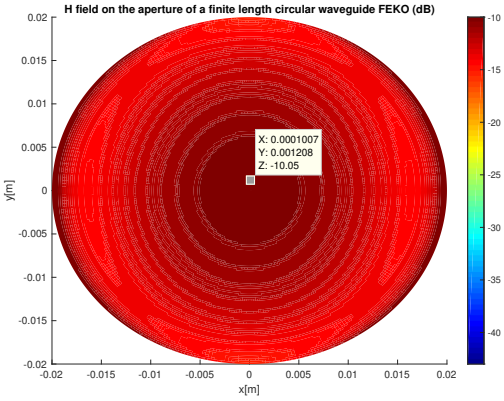

(f) H field at the aperture of a finite length circular waveguide from FEKO

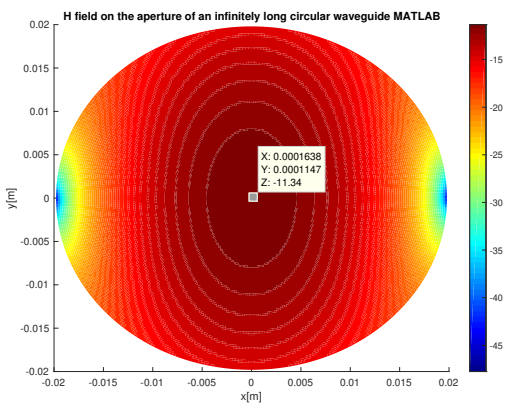

(g) H field at the aperture of a infinite length circular waveguide MATLAB

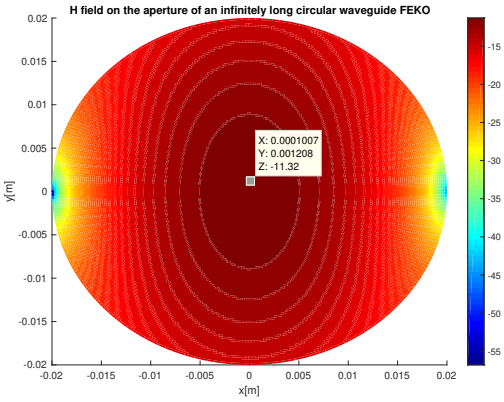

(h) H field at the aperture of a infinite length circular waveguide from FEKO (using absorbing condition)

Figure 5.18: Aperture electric/magnetic fields at 5 GHz for a circular waveguide of radius 2[cm]. Plots with Rumsey's method consider an open ended waveguide, open end being open to free space. 29 higher order modes are considered at the aperture for the same.

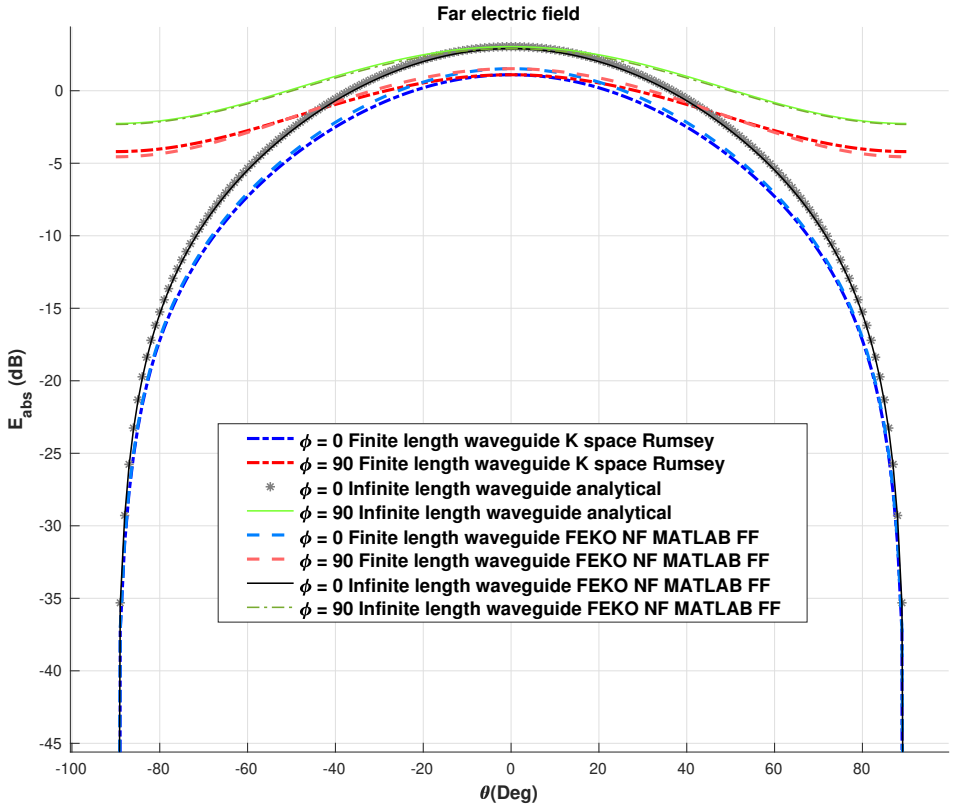

Figure 5.19: Far fields of an open ended circular waveguide (finite length) and an infinite length waveguide (with a absorbing boundary condition) with metal flange. FEKO NF and MATLAB FF suggests that the Far fields are obtained in MATLAB but the near-field patterns for the computation of the far-fields are taken from FEKO. In FEKO, the radius of the metal flange is 70 [cm]. There is a coaxial magnetic wall surrounding the metal flange of thickness 10 [cm] and height 10 [cm].

.

6

Optimization Techniques for the design of the smooth walled conical horn antenna

6.1. Problem formulation

Till chapter 5, various properties of the conical horn antenna were discussed. The antenna under test was always an aperture antenna, where the aperture is open to free space at the far end for practical purposes. For the SKA application, these types of horn antennas are used with a reflector (dish) system. The systems are designed so that the reflector-feed system should have optimum aperture efficiency, better matching with free space at the far end (minimum return loss), lower cross polar levels and so on. Using the hybrid method (Mode matching technique and the Rumesy's integrals), several goal functions can be devised which then can be optimized using some known algorithms. This way, the geometry of the horn can be determined for the requirements. The algorithms that are explored in this chapter are the genetic algorithm and the minimum non-linear programming solver ($fmincon$ in MATLAB). The reason to use these methods is that the goal functions in the case of conical horn antenna are non-linear in nature. The three parameters that are explored in this chapter for optimization are the return loss, the cross polar electric field level and the aperture efficiency of the reflector-feed system. The optimized input parameters (Geometry of the horn) are tested for a wide range of frequencies to test the consistency of the output parameters. This chapter has three sections. The first one describes the two optimization algorithms used from MATLAB libraries. In the second section, the definitions of the output parameters are discussed with the input parameters to be optimized. The third section comprises of the definition of the goal functions created for the optimization routines. The results are horn profiles for the requirements.

6.2. Optimization Algorithms

Optimization problems are used in a lot of fields including simple tasks in our daily lives. For example, for designing a smart city, one has to know how many hospitals needed to be installed and where should they be placed. Based on the requirement, certain design variables are chosen. After the design variables are chosen, using some optimization algorithms, the values to the design variables are found out for optimum performance. For example, some physical theories are a result of optimization problems such as the Euler-Lagrange differential equation [12]. Another example of a optimization problem is explained in this thesis in chapter 5. The variational approach with Rumesy's reaction concept to find the aperture admittance of aperture antennas is also an optimization problem in itself.

The variational approach is applied there to find the higher order mode excitation at the aperture free space transition and that was achieved by equating the change of aperture admittance with respect to the higher order mode excitation to zero $\frac{\partial y_{ap}}{\partial D_m} = 0$. This is done to make sure that the aperture admittance is invariant of the higher order mode excitation. Similarly variational approaches are also applied in quantum mechanics where the energy of a test state vector is minimized with respect to some design parameters [12].

There are several ways to optimize a problem. Different algorithms are developed to address such optimization problems. These algorithms find the values of the design variables that best fits the requirements. Some of the algorithms are the genetic algorithm, the pattern search optimization algorithm, the simulated-annealing optimization algorithm and so on. In this thesis, two algorithms are discussed in detail and they are the genetic algorithm and the MATLAB's $fmincon$ non-linear optimization algorithm.

6.2.1. Genetic Algorithm

Genetic algorithm is a global minima optimizer. It uses the principles of genetics to avoid stopping at local minima and find the true global minima by searching the entire solution space.

Process of optimization using genetic algorithm (GA)

In the GA optimizer, first an arbitrary initial population (sets of list of design variables) is created (if not given manually). Then, iterations are done to create new populations. The new generation is created based on fitness value maturity (return value from the goal function). Values for which the fitness is very low, are directly carried to the next generation. If they aren't very low, only some are taken. Based on the current fitness value, some are chosen to be parents and those parents create children population which then get forwarded for the next iteration. These children are derived based on mutation and cross over between the design variables of the parents. This allows the algorithm not to avoid potentially valid search spaces for global minima.

MATLAB implementation

In MATLAB, there are a broad range of arguments that can be passed to the GA algorithm function. However, in the thesis, only a few arguments are used. The implementation looks like the following.

```
problem.fitnessfcn = @(x) goal(x(1), x(2), x(N));  %Fitness function
problem.nvars = N;                   %Number of design variables
problem.lb = Lower_Bounds;           %Lower bounds of all design variables
problem.ub = Upper_Bounds;           %Upper bounds of all design variables
problem.solver = 'ga';
Ip = Initial_population_matrix;      %Initial Population Matrix
FitnessLimit = FL;                   %Fitness value limit (stop condition)

problem.options = optimoptions(@ga, 'PlotFcn',...
{'gaplotbestf', 'gaplotbestindiv'}, 'Display', 'iter',...
'InitialPopulationMatrix', [IP], 'UseParallel',...
true, 'FitnessLimit', FL); % Optimization options.

[r, fval, exf, output] = ga(problem); % Optimization call

% r - design variable optimized
% fval - fitness value for individual r
% exf - exit flag status
% output - various other attributes of the optimization
% Like maximum number of function calls or maximum number of generations
```

6.2.2. MATLAB's $fmincon$ non-linear optimization solution

Unlike the genetic algorithm, $fmincon$ is a local minima finder. It can be configured to find the first order optimality based on the derivative rule of finding local minima. It is well suited for non-linear problems and therefore it is tried in this context. The $x0$ (starting population) is chosen judiciously to avoid large run time of the algorithm.

MATLAB implementation

The implementation used in this thesis is shown in below example.

```
problem2.objective = ...
@(x) GSM_N_opt_allvar(x(1), x(2), x(N));
%Objective function

problem.lb = [lb.'];     % Lower bounds of design variables
problem.ub = [ub.']      % Upper bounds of design variables

problem.x0 = [x0];       % Starting point (design variables)
problem.solver = 'fmincon'; % solver name

problem.options = optimoptions(@fmincon,'PlotFcn', ...
    {'optimplotx', 'optimplotfirstorderopt'},...
     'UseParallel', true, 'MaxFunEval', Inf, 'MaxIter', Inf);
%fmincon options

[r, fval, exf, ouput] = fmincon(problem);

% r - design variable optimized
% fval - fitness value for individual r
% exf - exit flag status
% output - various other attributes of the optimization
% Like maximum number of function calls
```

6.3. Parameters for optimization

6.3.1. Return Loss

The return loss (RL) is defined in the MM (Mode Matching) software as the sum of the squares of the first column entries of S_{RR} matrix. S_{RR} matrix is the matrix containing the reflection coefficients at the waveguide port located the base element of the cone (at the throat) due to the excitation at the same port. As the cone is approximated as a series of cylindrical waveguides, more number of higher order modes get excited as we progress from the base to the top (open end) of the conical structure. Therefore, the S_{RR} matrix in the MM software contains the reflection coefficients of each and every mode excited inside the horn with the modes excited at the base element. In the applications, it is required to have only the fundamental mode excitation at the base element of the cone. Therefore, only the first column entry of S_{RR} is required to get the return loss of an antenna with only the fundamental mode excitation at the waveguide R or at the base element of the cone.

$$RL = |\sum_{j}^{N_j} S_{RR}^{1,j}|^2 \tag{6.1}$$

In this chapter, for the optimization of the return loss, the reflection at the waveguide free space

boundary is not considered. This is done to save computation time. Another reason for it is the reflection of the fundamental mode at the aperture of a flared horn antenna is very negligible as these horn antennas are well matched at the free space boundary.

6.3.2. Cross-polar levels

In this case of aperture antennas, cross polarizated fields are the fields which are anti-symmetric on the aperture and can leak into the co polarized field of the radiation pattern [16]. The cross polar field expression can be determined from the Ludwig's definitions [14]. The co and cross polar components, hence take the form given below,

$$E^{co} = \frac{e^{-jkr}}{r}\Big[CO(\theta) + XP(\theta)\cos(2\phi)\Big] \tag{6.2}$$

$$E^{xp} = \frac{e^{-jkr}}{r}\Big[XP(\theta)sin(2\phi)\Big] \tag{6.3}$$

Here, $CO(\theta)$ and $XP(\theta)$ are the radiation patterns which depend on θ and computed at $\phi = \frac{\pi}{4}$.

$$CO(\theta) = \frac{1}{2}\Big[A(\theta) + B(\theta)\Big] \tag{6.4}$$

$$XP(\theta) = \frac{1}{2}\Big[A(\theta) - B(\theta)\Big] \tag{6.5}$$

Here, A and B are defined as the radiation patterns with respect to θ on E and H planes. Therefore $A(\theta)$ is computed when $\phi = 0$ and $B(\theta)$ is computed when $\phi = \frac{\pi}{2}$.

The co-polar and cross-polar fields also can be found from the θ and ϕ components of the electric far-field.

$$E^{co} = \sin\phi E_\theta\hat{\theta} + \cos\phi E_\phi\hat{\phi} \tag{6.6}$$

$$E^{xp} = \cos\phi E_\theta\hat{\theta} - \sin\phi E_\phi\hat{\phi} \tag{6.7}$$

The radiation patterns E_θ and E_ϕ can be computed from the spectrum functions (In the K-Space domain). The spectrum functions in x and y components can be found in equations (5.55) and (5.60). In the spectrum function, stationary phase approximation has to be used for the computation of far-fields. Therefore, the spectral arguments k_Ω and Θ in the equations (5.58) and (5.61) can be used as the following in spacial domain.

$$k_\Omega = \sqrt{k_x^2 + k_y^2} = k\sin\theta\sqrt{\cos^2\phi + \sin^2\theta} = k\sin\theta \tag{6.8}$$

And also the term Θ in the expressions of equation (5.58) and (5.61) is given by,

$$\Theta = \arccos(\frac{k_x}{k_\Omega}) = \phi \tag{6.9}$$

Therefore, the terms $I_{00}(k_\Omega)$ and $I_{22}(k_\Omega)$ can be expressed as $I_{00}(\theta)$ and $I_{22}(\theta)$.

The requirement from SKA says that the cross polarization levels should be below -15 dB for the HPBW (Half power Beamwidth). This should be consistent through out the bandwidth of operation. These requirements are taken from [4] which are relevant to the quadruple-ridge flared horn (QRFH) as well.

6.3.3. Efficiencies

There are several types of efficiencies related to the feed-reflector system. They are respectively the taper efficiency, spillover efficiency, polarization efficiency, phase efficiency and the aperture efficiency. Aperture efficiency is the multiplication of the illumination efficiency, spillover efficiency, polarization efficiency and the phase efficiency.

Taper Efficiency

Taper efficiency is a measure of how effectively the reflector area with respect to the physical area projected on the equivalent aperture. It is dependent on the distribution of phase, amplitude, and polarization of the aperture field. It can be calculated from the aperture field as

$$\eta_t = \frac{1}{A_{phys}} \frac{|\int\int_S E_a^{co}(\rho', \phi') dS|^2}{\int\int_S |E_a(\rho', \phi')|^2 dS} \tag{6.10}$$

The term $E_a^{co}(\rho', \phi')$ is the incident electric field on the reflector from the feed. The incident field on the reflector surface can be found from the far-fields of the feed as given below,

$$E_{a,\rho}(\rho, \phi) = -E_{\theta,obs}^{FF}(2\arctan(\frac{\rho}{2f}, \phi)) \frac{4f}{4f^2 + (\rho^2)} e^{2jkf} \tag{6.11}$$

$$E_{a,\phi}(\rho, \phi) = -E_{\phi,obs}^{FF}(2\arctan(\frac{\rho}{2f}, \phi)) \frac{4f}{4f^2 + (\rho^2)} e^{2jkf} \tag{6.12}$$

Therefore, the ρ component of the aperture field on the reflector is equal in magnitude and opposite in direction with the θ component of the incident far field of the feed. The ϕ component of the reflector aperture field has the same relation with the ϕ component of the far field of the feed (incident field on the reflector).

Here, f is the focal length of the reflector system.

Spillover Efficiency

It is a measure of the feed power that is intercepted by the reflector: high spillover efficiency means all the power is intercepted. It can be calculated from feed far field.

$$\eta_{sp} = \frac{\int_0^{2\pi} \int_0^{\theta_0} U_{feed} \sin\theta d\theta d\phi}{\int_0^{2\pi} \int_0^{\pi/2} U_{feed} \sin\theta d\theta d\phi} \tag{6.13}$$

In another form, it is,

$$\eta_{sp} = \frac{\int_0^{\theta_0} [|CO(\theta)|^2 + |XP(\theta)|^2] \sin\theta d\theta}{\int_0^{\frac{\pi}{2}} [|CO(\theta)|^2 + |XP(\theta)|^2] \sin\theta d\theta} \tag{6.14}$$

Here, $CO(\theta)$ and $XP(\theta)$ are taken from equations (6.4) and (6.5). Here, U_{feed} is defined as,

$$U_{feed} = \frac{|E_{feed}^{FF}|^2}{2\zeta} \tag{6.15}$$

Here, E_{feed}^{FF} is the far-field of the Feed and ζ is the free space wave impedance (120π). The elevation angle on the denominator is here set as $\pi/2$ because the far field so far is calculated assuming that there is a ground plane at the aperture of the feed which allows no radiation on the bottom half elevation space ($\pi/2 < \theta < \pi$).

The angle θ_0 is defined as the subtended half angle of the feed-reflector system and it depends on the focal length to diameter ratio of the reflector. For a typical SKA 1 dual reflector systems, this angle is derived from the effective f/D ratio and they typically have the values 0.45, 0.5 and 0.55. The angle θ_0 for these values of f/D are found to be 58, 53 and 49 degrees [4]. For the analysis in the optimization routines, f/D of 0.55 is used typically in this thesis.

Polarization efficiency

Polarization efficiency is the ratio of the power carried by the co-polar component of the field to that of the total field.

$$\eta_{pol} = \frac{\int_0^{\theta_0} [|CO(\theta)|^2 + \frac{1}{2}|XP(\theta)|^2] \sin\theta d\theta}{\int_0^{\theta_0} [|CO(\theta)|^2 + |XP(\theta)|^2] \sin\theta d\theta} \tag{6.16}$$

These integrals are only on the θ domain because $CO(\theta)$ and $XP(\theta)$ are defined at $\phi = 45$ degree where the cross-polar levels are the worst.

Aperture Efficiency

This efficiency is one optimizaiton parameter which is considered in the thesis. It is the overall efficiency of the reflector-feed system. It is defined as the multiplication of the taper, the spillover and the polarization efficiencies.

$$\eta_{ap} = \eta_t \eta_{sp} \eta_{pol} \tag{6.17}$$

Typically for the SKA 1 dual reflector system, the requirement is to have as much aperture efficiency as possible. Typically it should be more than 50% for WBSPFs [4]. There is a trade off between the spillover and the taper efficiency. The more the ratio between the reflector diameter to the feed diameter, the better is the spillover but the worse is the taper efficiency. Therefore, it is the duty of the engineer to find a sweet spot where the trade off is not worse and we get maximum aperture efficiency.

6.3.4. Input parameters to be optimized for the smooth walled horn antenna

In the MM software along with the reflection coefficient software for free-space-waveguide boundary, it is known that the variables that affect the performance of the conical horn antenna are the number of cylindrical waveguide elements, the radius and height of each cylindrical element and the length of the horn. In all optimization routines, the length of the base cylindrical element (the throat) is kept as $\lambda/4$. It remains a constant and this variable isn't optimized. This is done to make sure all the evanescent modes are died out before entering into the flared section of the horn.

6.4. Goal/Objective Functions

6.4.1. Return loss goal function and optimization procedure

For the return loss, the output of the goal function is very straight forward. It is the square sum of the first column of the matrix S_{RR} as mentioned in the equation (6.1). It is derived from the MM software.

The horn in this case was divided into four conical sections and one throat cylindrical section (N = 5). The length of the cylindrical throat section was kept as one fourth of the wavelength of the frequency used. The bottom and top radii of each conical section was kept as design variables. The overall length of the flared section was the 5th design variable. Their upper and lower bounds are shown in table 7.1. In the goal function, the input arguments are the radii of each conical section (top and bottom), the overall length of the flared section. The overall structure was then divided into a number of cylindrical waveguide sections of length $\lambda/10$ each. After the radii and lengths of all cylindrical elements were defined, it was used to find the return loss using the GSM software of mode matching.

This optimization is done by both the genetic algorithm (GA) and the non-linear programming solver ($fmincon$) of MATLAB.

In GA algorithm, there is a fitness limit set to save computation time. In this case, the fitness limit was kept at $-25dB$. The MATLAB routine looks like the following. The initial population matrix is a equispaced cascaded structure of N conical waveguides whose radii vary linearly from throat to the aperture. Similarly with $fmincon$ also it is simulated.

```
%%  Fitness function

problem2.fitnessfcn = @(x) GSM_N_opt_allvar([x(1:N)], [l1 x(N+1:2*N-1)], F, HM);
problem2.nvars = 2*N - 1; % Number of variables to be optimized

lb = zeros(2.*N-1, 1); % Initialization of lower bounds
ub = zeros(2.*N-1, 1); % Initialization of upper bounds

lb(1) = R1;              % lower bound radius of first element
ub(1) = R1 + R1/5;       % upper bound radius of first element

for i =  2:N             % radii upper and lower bounds
    lb(i) = ub(i - 1) - R_test(1)/5;
    ub(i) = R_test(i) + R_test(1)/5;
end

for m = N+1:2*N-1        % Length segment, upper and lower bounds
    lb(m) = l(m - N) - lamb/5;
    ub(m) = l(m - N) + lamb/5;
end

problem2.lb = [lb.'];
problem2.ub = [ub.'];

IP = [R_test l.'];      % Initial population matrix

problem2.solver = 'ga'; % Solver

problem2.options = optimoptions(@ga, 'PlotFcn', {'gaplotbestf',...
'gaplotbestindiv'}, 'Display', 'iter',...
    'InitialPopulationMatrix', [IP], 'UseParallel',...
    true, 'FitnessLimit', 10^{-45/20}); % Optimization options.
```

```
[r, fval2, exf2, ouput2] = ga(problem2); % Optimization call
```

Where $R1$ is the radius of the first element, R_test is a linear profile of all radii from the first to last element. lb and ub are the vectors containing all the lower bounds and all the upper bounds of the radius and length of each section respectively. The F and HM arguments in the fitness function are the frequency and the number of higher order modes to be considered in the MM software respectively.

The upper ΔL_{ub} and lower bounds $\Delta L_{lb}$of the length segments are kept as follows,

$$\Delta L_{ub} = \frac{L}{N} + \frac{\lambda}{5} \tag{6.18}$$

$$\Delta L_{lb} = \frac{L}{N} - \frac{\lambda}{5} \tag{6.19}$$

Where, L is the length of the horn.

The Fitness function (Goal function) is the MM software to calculate the scattering matrix of a cascaded structure of cylindrical waveguide structures.

After the optimized variables are obtained, with the same geometry, the return loss at different frequency points are tested.

6.4.2. Cross polarization goal function and optimization procedure

The optimization is performed as mentioned above for return loss. In this case, just that the fitness function is a different function and it returns the maximum of relative cross-polarization level with respect to the maximum of co-polar field. From the knowledge of cross-polarization in equation (6.2) and (6.3), we know that the cross polarization has maximum values when the azimuth angle is 45 degree ($\phi = 45$ deg). Therefore, this fitness function has several steps. First it calculates the General Scattering matrix using the MM software. After that it calculates the reflection coefficients of every mode that can be present at the aperture (As due to the flare, more modes are excited) with the free space boundary. Then, using the higher order mode excitation at the aperture-free space boundary and the reflection coefficients of each mode at the aperture, the far fields are calculated analytically for every mode separately. Furthermore, as only the dominant mode is the fundamental mode, using the general scattering matrix information (Transmission coefficients), the far fields due to every mode is calculated and added as a weighed sum where the weights are the transmission coefficients of each mode from the base to the top of the horn with respect to the fundamental mode (TE_{11}).

Using the information of the far fields and the analytical analogy mentioned in equation (6.2) and (6.3), the ratio of the maximum cross-polar field at $\phi = 45$ to the maximum of co-polar field is returned in dB scale.

The goal function in MATLAB looks like the following.

```
function [Max_Exp_diff] = MinXP_Goal(R, L, F, k, timesk0, HM)

n = length(R);


er = ones(1, n); % Relative Permittivity of each WG section
mur = ones(1, n); % Relative Permeability of each WG sectio
```

```
dth = pi/180;
dph = pi/180;

[th, ph] = meshgrid(eps:dth:pi/2+eps, eps:dph:2*pi+eps);

[Gamma, Dm, ModeNumberAper, Transmission_sum]  = ...
Feed_Gamma_Dm_opt(R, L, F, k, er, mur, timesk0, HM);

% MM software and aperture-freespace software to calculate
% the reflection coefficients at the aperture and GSM inside the horn.

[~, ~, Eco, Exp, ~, ~] = ...
Feed_FF_Superposition(ModeNumberAper, Gamma, Dm, th, ph, F, er, mur, R,...
Transmission_sum, HM);
% Fields calculation

Max_Exp_diff = - db(abs(max(max(abs(Eco)))./max(abs(Exp(46, :)))));

% Negative difference of co and cross polar fields in dB

end
```

Here, $timesk0$ is used as the maximum integration limit in the Rumsey's reaction integrals present in chapter 5 for the calculation of the reflection coefficients of modes at the free space-waveguide boundaries (at the aperture). Here k is the higher order modes used in MM software and HM is the higher order modes in the aperture reflection software.

6.4.3. Aperture efficiency goal function and optimization procedure

In this case as the aperture efficiency has to be a maximum, the negative of the aperture efficiency is taken into account as the return value from the goal function. The initial population is chosen by plotting the aperture efficiency of linear taper conical profile for a fixed f/D ratio of the reflector but a variable size of the aperture of the conical horn. The aperture radius at which the aperture efficiency comes out to be maximum is chosen as one of the design variables of the initial population vector in the case of genetic algorithm solver and the starting point vector in the $fmincon$ solver in MATLAB.

The goal function for that is given below.

```
function [e_ap] = Ga_opt_aper_eff(R, L, F, k, HM, timesk0, focal_length, d)

zeta = 120 .* pi;

n = length(R);

er = ones(1, n); % Relative Permittivity of each WG section
mur = ones(1, n); % Relative Permeability of each WG sectio

dth = pi/180;
dph = pi/180;

[th, ph] = meshgrid(eps:dth:pi/2+eps, eps:dph:2*pi+eps);

[Gamma, Dm, ModeNumberAper, Transmission_sum]  = ...
Feed_Gamma_Dm_opt(R, L, F, k, er, mur, timesk0, HM);
```

```
[Eth, Eph, ~, ~, CO, XP] = ...
Feed_FF_Superposition(ModeNumberAper, Gamma, Dm, th, ph, F, er, mur, R,...
Transmission_sum, HM);

C_spillover = 1/(2 .* zeta);

f_pattern_square = abs(Eth).^2 + abs(Eph).^2;

U_feed = C_spillover .* f_pattern_square;

CO_XP_square = abs(CO).^2 + abs(XP).^2;
CO_XP_half = abs(CO).^2 + 1./2 .* abs(XP).^2;

drho = d/200; dphi = pi/ 180;

[rho, phi] = meshgrid(eps:drho:d/2, eps:dphi:2*pi);

theta_ = 2 * atan(rho/(2 * focal_length));

f_hash = focal_length./d; %f/D ratio of reflector

% Spillover efficiency (eta_s)

theta_0 = 2 * acot(4 * f_hash); % subtended half angle

% numerator
Int_u_n = U_feed(:,th(1,:)<=theta_0) .* sin(th(:,th(1,:)<=theta_0)) .* dth .* dph;
n_f = sum(sum(Int_u_n));

%denominator
Int_u_d = U_feed .* sin(th) .* dth .* dph;
d_f = sum(sum(Int_u_d));


eta_s = n_f/d_f;

% Taper efficiency (eta_t)

[Eth_, Eph_, Eco_, ~, ~, ~] = ...
Feed_FF_Superposition(ModeNumberAper, Gamma, Dm, theta_, phi, F, er, mur, R,...
Transmission_sum, HM);

C = ((4 .* focal_length)./(4 .* focal_length.^2 + rho.^2));

Erho_ = - Eth_ .* C;
Eph_  = - Eph_ .* C;
Ecoa  = - Eco_ .* C;

etp_n = abs(sum(sum(Ecoa .* rho .* drho .* dphi))).^2;

E_abs_rpz = abs(Erho_).^2 + abs(Eph_).^2;
Int_etp_d = E_abs_rpz .* rho .* drho .* dphi;
etp_d = sum(sum(Int_etp_d));

Area = pi .* (d^2)/4;
e_tp =  (1/Area) * etp_n./etp_d;
```

```
%Polarization efficiency

eta_pol_n = sum(sum((abs(CO_XP_half(:,th(1,:)<=theta_0))) .*...
sin(th(:,th(1,:)<=theta_0)) .* dth .* dph));
eta_pol_d = sum(sum(CO_XP_square(:,th(1,:)<=theta_0) .*...
sin(th(:,th(1,:)<=theta_0)) .* dth .* dph));

eta_pol = eta_pol_n./eta_pol_d;
% aperture efficiency
e_ap = -eta_s .* eta_pol .* e_tp;

end
```

The simulation results using these algorithms and the commercial tool equivalent models are shown in the next chapter (chapter 7).

7

Optimization Results

This chapter contains the results of the optimization mentioned in chapter six. This chapter contains three sections. The first part is about the return loss optimization. The second part is about the cross polarization optimization. The third section is about the aperture efficiency optimization. All sections include their corresponding commercial tool results for verification.

7.1. Results of return loss optimization

7.1.1. Genetic algorithm

With the genetic algorithm, the problem of return loss is a convex problem where with optimization iteration, the return value of the objective function is decreasing and converging. The upper limits and the lower limits of the design variables are shown in table 7.1. The horn is divided into four conical sections and one throat cylindrical section. The radii of all these sections are considered as the design variables. The way these design variables are used for the optimization is given in section 6.4.1. In addition to that, the combined length of the four conical sections is used as the final design variable.

The initial profile of the horn is chosen to be a linearly increasing cross section where the radius of the throat is two centimeter and the aperture radius is two times the wavelength (12 centimeter). The intitial horn profile length is six times the wavelength (30 centimeter).

Design Variable	lower bound	upper bound
r1	2 [cm]	5 [cm]
r2	2 [cm]	7.5 [cm]
r3	4.5 [cm]	10 [cm]
r4	7 [cm]	12.5 [cm]
r5	9.5 [cm]	15 [cm]
Length	30 [cm]	48 [cm]

Table 7.1: Lower and upper bounds of the design variables

With genetic algorithm, it takes two generation of populations to reach a minimum threshold for the fitness value (return value from the objective function). It is set to be -45 dB. The values of the design variables retrieved from the genetic algorithm optimization is shown in the table 7.2.

The horn profile that is derived at five GHz is shown below in the figure 7.1. The base radius is kept in a way that the frequency five GHz falls within the bandwidth of a waveguide of the same radius for its fundamental mode (TE_{11}). This horn profile is used to further calculate the return loss of at

Design Variable	GA algorithm return value
r1	2.833 [cm]
r2	6.313 [cm]
r3	7.772 [cm]
r4	9.971 [cm]
r5	14.67 [cm]
Length	32.73 [cm]

Table 7.2: Horn profile retrieved from GA optimization for return loss

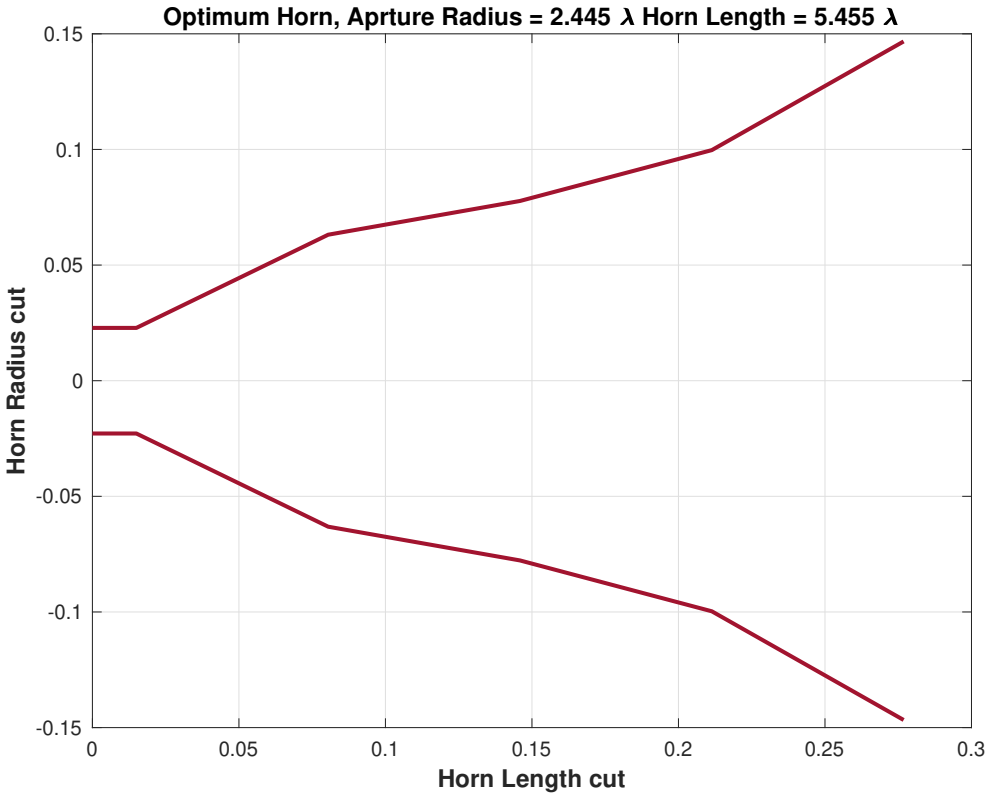

Figure 7.1: Horn profile retrieved from GA optimization

different frequencies. The return loss of the optimized antenna is shown in figure 7.3 from four to eight GHz. With the MM technique, it is still possible to compute the return loss for even higher frequencies. However, in FEKO, it is very computationally expensive and sometimes it is not possible due to the limited computational resources. The S-parameters of TE_{11} mode with itself and TE_{12} mode with TE_{11} mode is shown in figure 7.4. It is seen that they have excellent agreement with one another.

Although, it is assumed that, when determining the return loss, the structure of the antenna should favour for only one frequency (in this case five GHz) and not for other neighbouring frequencies, surprisingly it did favour the other frequencies in the band. For a wide range of frequencies the return loss remained below -10 dB. The same structure is simulated in FEKO. Furthermore, the radius of the throat is found to be 2.833 [cm]. It is a very good result from the optimizer because the frequency at which the optimized antenna dimensions are calculated is five GHz and for a waveguide of radius 2.833 [cm], five GHz is just below the cut off frequency of the first higher order mode (TM_{01}). For a waveguide excited with the mode TE_{11}, minimum reflection occurs at higher frequencies when the aperture size is electrically big in size (in this case the higher frequencies supported by the fundamental mode).

The equivalent model simulated in FEKO is shown in figure 7.2. It uses two symmetry planes. On

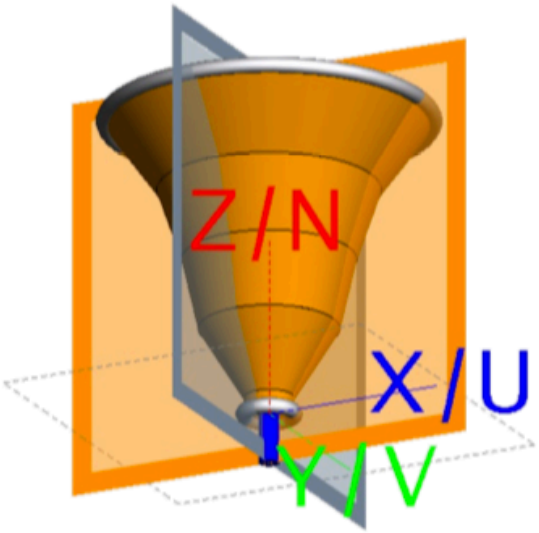

Figure 7.2: Horn profile simulated for a frequency band of 4 to 8 GHz in FEKO. The genetic algorithm optimized horn profile.

the zy plane $x = 0$, there is a magnetic symmetry and on the xz plane $y = 0$, there is an electric symmetry plane. Symmetry planes are used for two reasons. One reason to use the symmetry planes is to reduce the computational time and second is to have a more uniform mesh along the cuts of the symmetry planes.

7.1.2. $fmincon$ algorithm

The horn profile is optimized with the goal function returning the reflection coefficient of the fundamental mode TE_{11} with itself at five GHz. The horn profile is shown in figure 7.5.

The lower bound and upper bounds for all design variables are taken the same as in table 7.1. The starting point for all design variables are taken the same as in the case of return loss. The optimized design variables are shown in table 7.3. The same profile is used to find the return loss at a band of frequencies from 2.75 GHz to 9.43 GHz. The results are shown in figure 7.7 from the MATLAB model and from an equivalent FEKO model of the same horn profile. The FEKO model is shown in figure 7.6. In the FEKO model, symmetry planes are used to reduce the computational time and resources. However, for frequencies higher than 9.43 GHz, the computational resources and time are very high. Therefore, the comparison is shown till 9.43 GHz. It covers an useful band of frequencies because the cut off frequency of the second mode having the same type and same azimuthal variation as TE_{11}, which is TE_{12} is 7.9 GHz for the cylindrical waveguide at the throat of the cone. The comparison shows that the MATLAB model has good agreement with the commercial solver from FEKO. The comparison for the reflection coefficient of TE_{11} with TE_{11} and also the reflection coefficient of TE_{12} with TE_{11} at the throat of the cone is shown in figure 7.8.

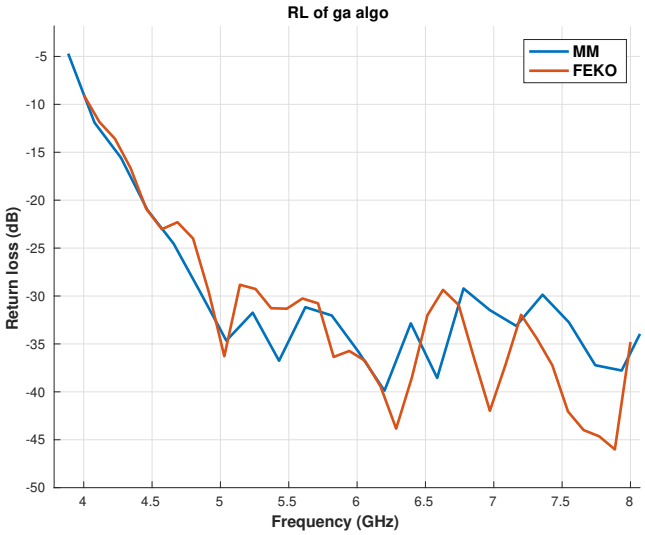

Figure 7.3: Return loss of the optimized horn profile with GA algorithm.

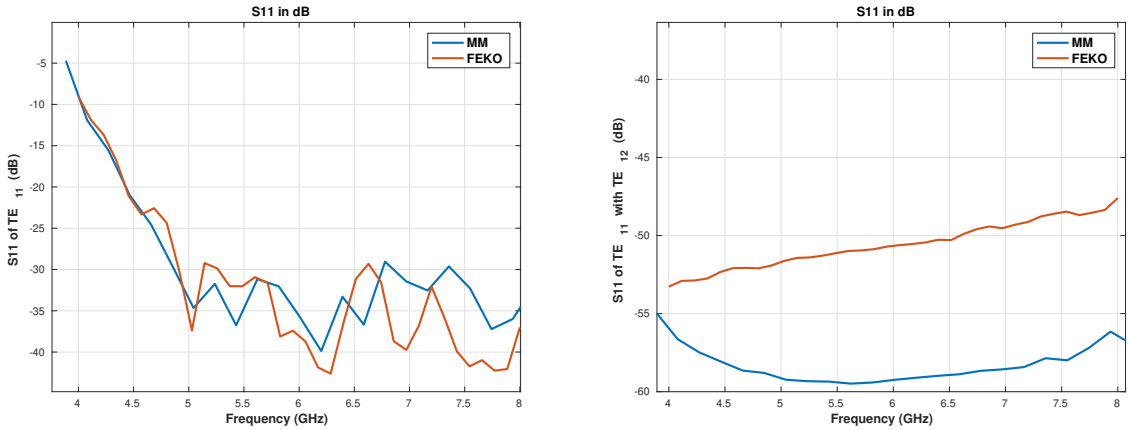

(a) S_{RR} of TE_{11} with TE_{11}

(b) S_{RR} of TE_{11} with TE_{12}

Figure 7.4: Reflection coefficient of TE_{11} with TE_{11} and TE_{11} with TE_{12}

7.2. Results of cross polarization optimization

7.2.1. Genetic algorithm

The cross-polarization optimization is also done at five GHz frequency with the same initial points, upper bounds and lower bounds for the return loss optimization. The results from optimization with genetic algorithm are shown in table 7.4. The horn profile is shown in figure 7.9.

The same configuration is simulated in FEKO with a frequencies 2.6129 GHz, 5.0492 GHz and 7.7561 GHz. The FEKO configuration also has the symmetry planes as in the case of return loss experiments. The FEKO configuration is shown in figure 7.10.

The co- and cross-polarization radiation patterns obtained from this profile is shown in figure 7.11. The comparison shows that FEKO results and MM results have very good agreement with one another. At higher frequencies (7.7561 GHz), however, there are differences observed between the two methods. This occurs because of two reasons. At higher frequencies, FEKO offers good results only when the mesh is very fine. Furthermore, at high frequencies more higher order modes can be excited along

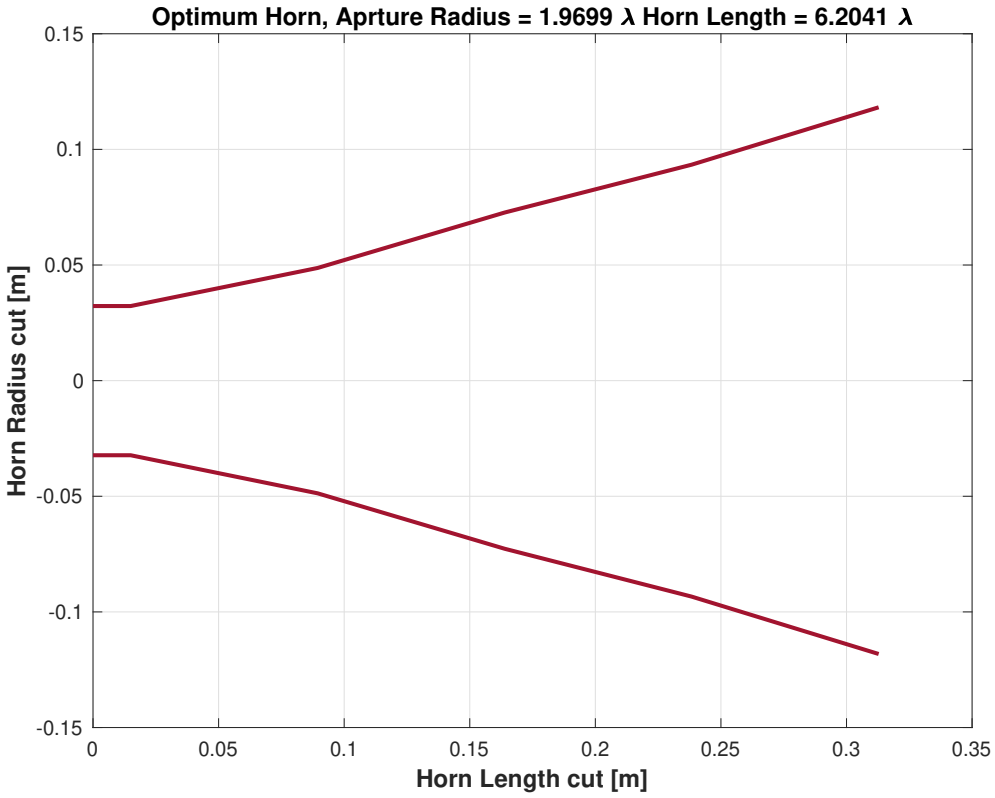

Figure 7.5: Horn profile retrieved from $fmincon$ algorithm.

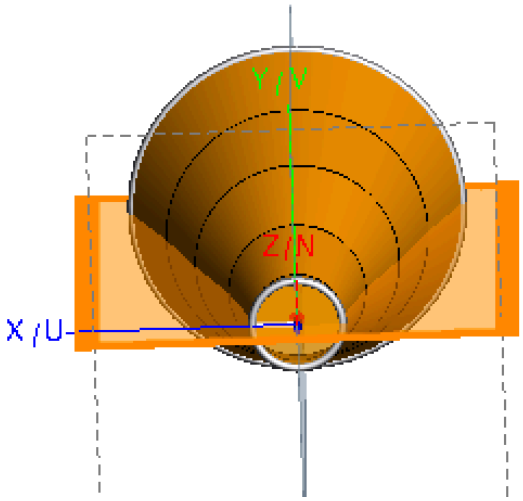

Figure 7.6: Horn profile simulated for a frequency band of 2.75 GHz to 9.43 GHz in FEKO. The $fmincon$ algorithm optimized horn profile.

Design Variable	$fmincon$ algorithm return value
r1	3.23 [cm]
r2	4.87 [cm]
r3	7.27 [cm]
r4	9.34 [cm]
r5	11.82 [cm]
Length	37.22 [cm]

Table 7.3: Horn profile retrieved from $fmincon$ algorithm optimization for return loss

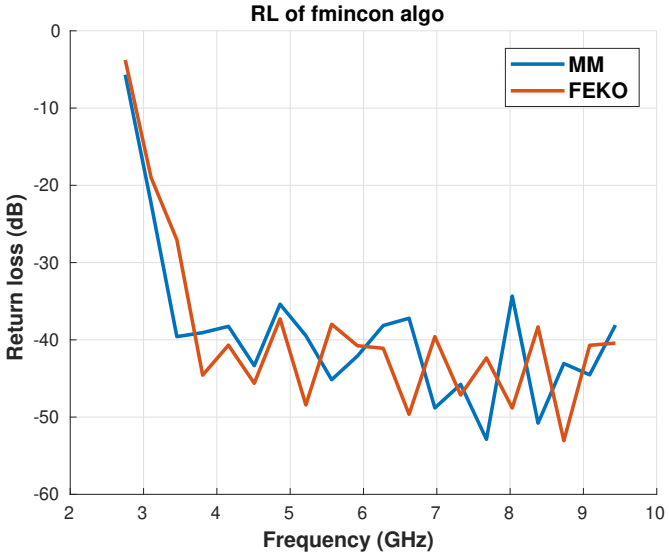

Figure 7.7: Return loss of the optimized horn profile with $fmincon$ algorithm.

the flare of the horn. Hence, as discussed in chapter three, some modes can be coupled in FEKO simulations but not in the proposed software. Therefore, some differences in the radiation pattern is observed. As in the proposed technique, the geometry is considered to be a combination of perfect cones, and the coupling is observed only with the modes having the same azimuthal variation, the field patterns contain deep minimum values (not observed in FEKO results). It can also be observed that at higher frequencies, the maximum cross polar level obtained from the proposed technique is greater than the maximum cross polar level obtained from FEKO simulations. Therefore, the optimization with respect to the goal function built from the proposed technique is effective as it considers the worst cross polar levels (as it considers ideal conditions with respect to geometry).

7.3. Results of aperture efficiency optimization

7.3.1. $fmincon$ algorithm

The aperture efficiency optimization was carried out at three GHz. Here, the starting point was chosen differently than the other two optimization performed in sections 7.1 and 7.2. The horn length in this case was chosen to be smaller (around one wavelength). This is done to make sure that the directivity is not very high (which results in lower taper efficiency). The initial radius of the throat section is chosen to be 3.03 centimeter and the initial top radius of the last conical section is chosen to be 6.58 centimeter. The intermediate radii follow a linear trend from 3.03 centimeter till 6.58 centimeter. The initial length of the conical sections combined is chosen to be one wavelength (10 centimeter). Without the waveguide-free space transition in consideration, the aperture efficiency of the initial profile of the antenna is found to be 72%. The upper bound and lower bounds of the design variables are shown in table 7.5. The subtended angle of the feed reflector system is chosen to be 50 degree.

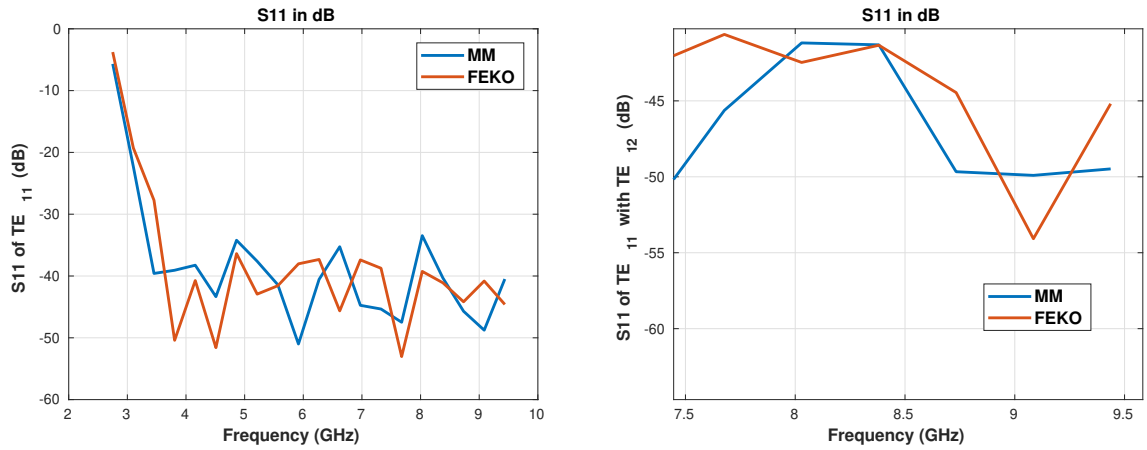

(a) S_{RR} of TE_{11} with TE_{11}

(b) S_{RR} of TE_{11} with TE_{12}

Figure 7.8: Reflection coefficient of TE_{11} with TE_{11} and TE_{11} with TE_{12}

Design Variable	GA algorithm return value
r1	3.40 [cm]
r2	5.40 [cm]
r3	4.78 [cm]
r4	7.00 [cm]
r5	9.41 [cm]
Length	45 [cm]

Table 7.4: Horn profile retrieved from GA optimization for cross-polarization.

The optimized antenna dimensions are given in table 7.6. The horn profile is shown in figure 7.12. The aperture efficiency of the optimized antenna at the frequency of optimization is found to be 74.23%. The aperture efficiency is shown in figure 7.13 with respect to frequency. The aperture efficiecny in this case is above 50% for a bandwidth of 2:1. The maximum aperture efficiency is observed at 2.998 GHz. As frequency increases, the taper efficiency decreases. For this reason, the aperture efficiency decreases. The directivity of the optimized antenna is shown in figure 7.15b with the comparison to an equivalent FEKO model (shown in figure 7.14) at frequency 2.998 GHz. The results have very good agreement with one another. The normalized co-polar and cross-polar fields are shown in figure 7.15a with the comparison to the FEKO results. The results also have good agreement with one another.

7.4. Conclusions

In this chapter, the goal functions defined in chapter six are used for optimization of the return loss, the cross-polarization levels and the aperture efficiency. The horn profile was simulated over a band of frequencies. The results are compared with equivalent FEKO model simulations. The results have excellent agreement with one another. Therefore, it can be concluded that with goal functions developed in this thesis project based on the novel technique is very effective in finding out optimized antenna profiles for minimum return loss, cross-polarization levels and aperture efficiency.

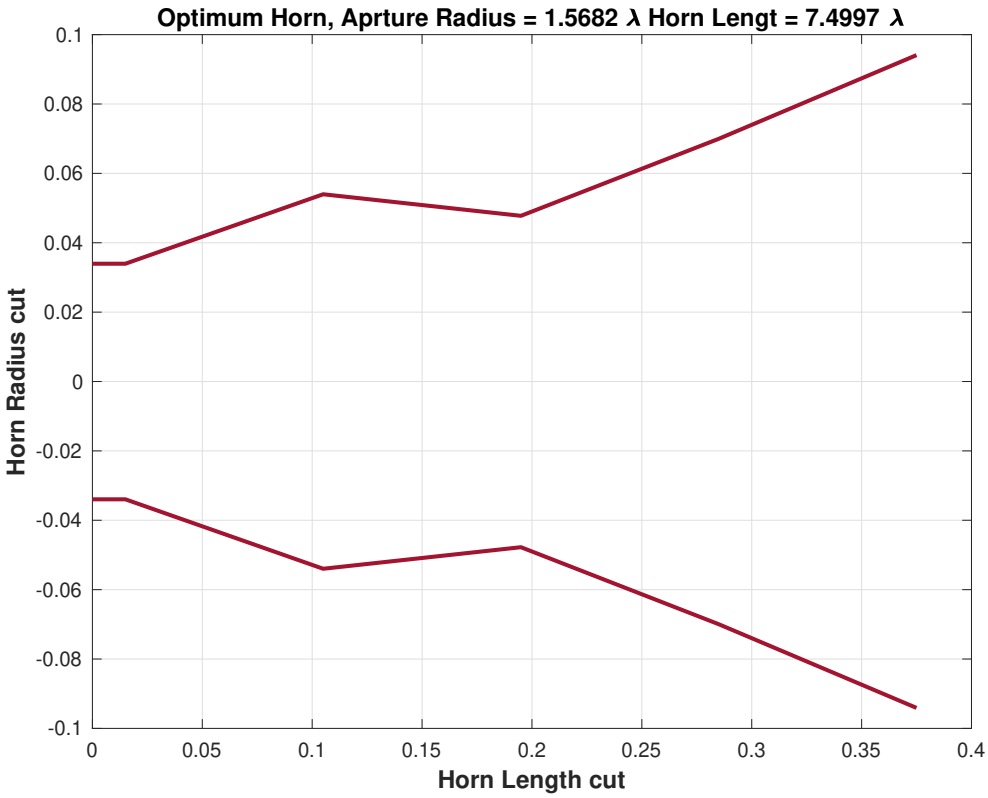

Figure 7.9: Horn profile retrieved from GA optimization for cross-polarization

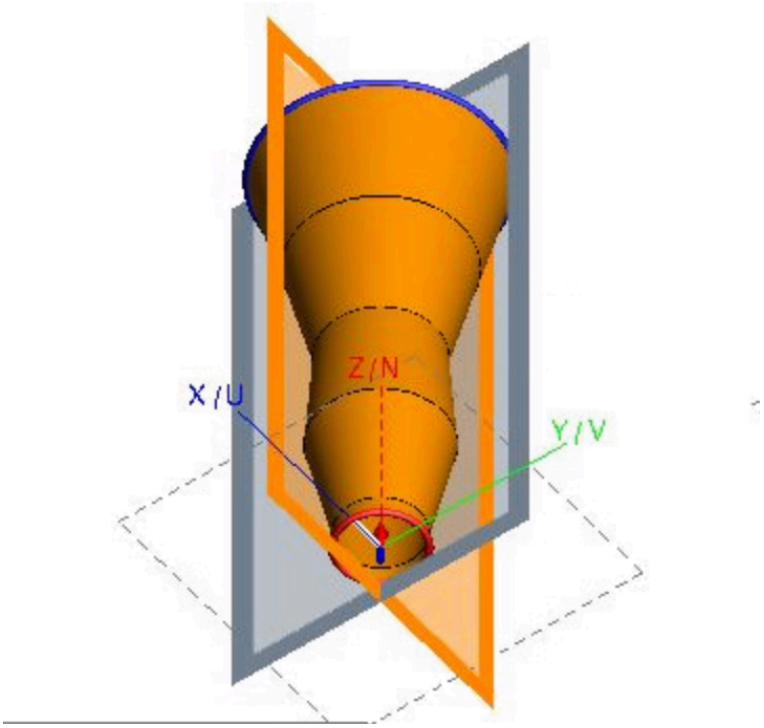

Figure 7.10: Horn profile simulated for frequencies 2.6129 GHz, 5.0492 GHz and 7.7561 GHz in FEKO. The GA optimized horn profile.

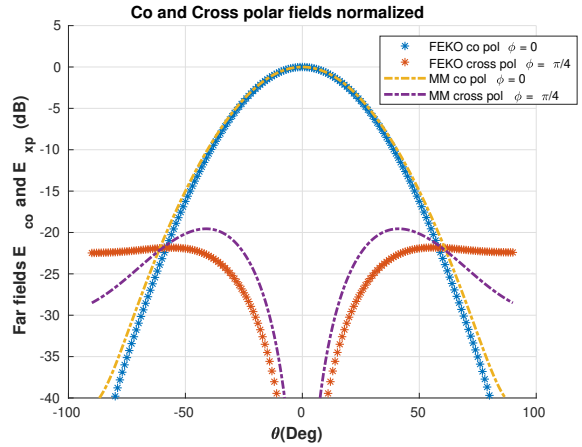

(a) 2.6129 GHz

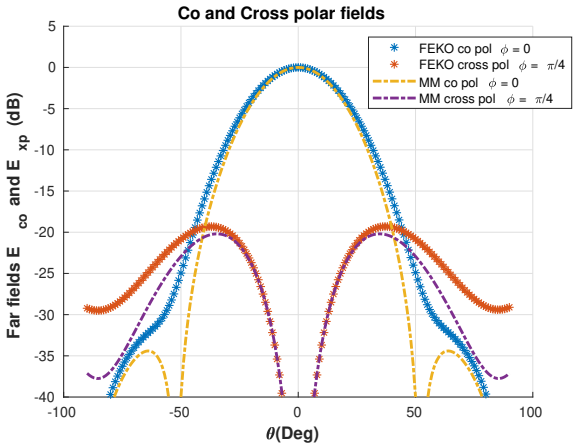

(b) 3.4250 GHz

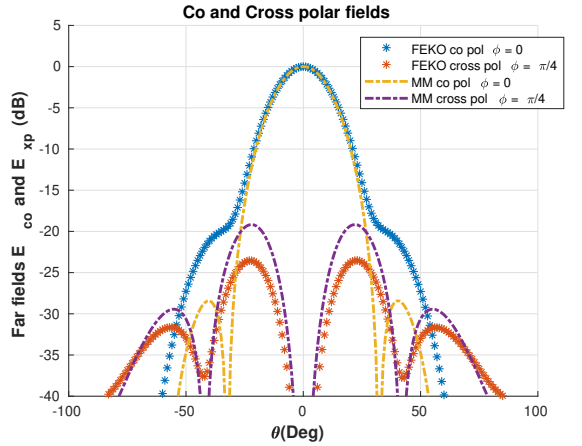

(c) 5.0492 GHz

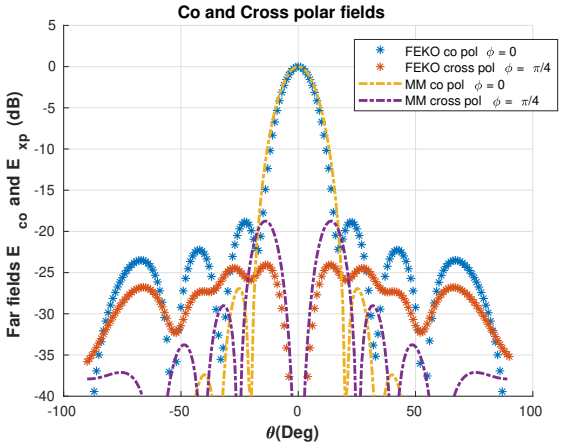

(d) 7.7561 GHz

Figure 7.11: Co- and cross-polarized radiation patterns of GA optimized horn profile when excited with only the fundamental mode TE_{11}

Design Variable	lower bound	upper bound
r1	3.03 [cm]	5.53 [cm]
r2	3.03 [cm]	6.42 [cm]
r3	3.92 [cm]	7.30 [cm]
r4	4.80 [cm]	8.19 [cm]
r5	5.69 [cm]	9.08 [cm]
Length	5 [cm]	20 [cm]

Table 7.5: Lower and upper bounds of the design variables for aperture efficiency optimization.

Design Variable	$fmincon$ algorithm return value
r1	4.28 [cm]
r2	4.72 [cm]
r3	5.61 [cm]
r4	6.5 [cm]
r5	6.04 [cm]
Length	12.50 [cm]

Table 7.6: Horn profile retrieved from $fmincon$ optimization for aperture efficiency.

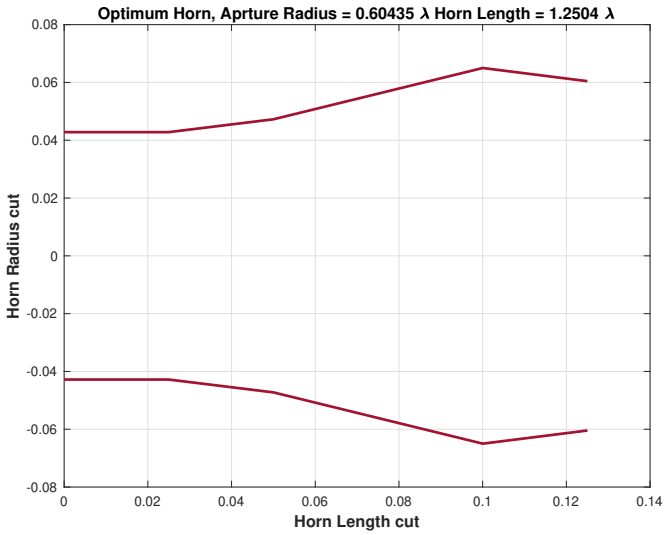

Figure 7.12: Optimized horn antenna profile at 3 GHz for aperture efficiency.

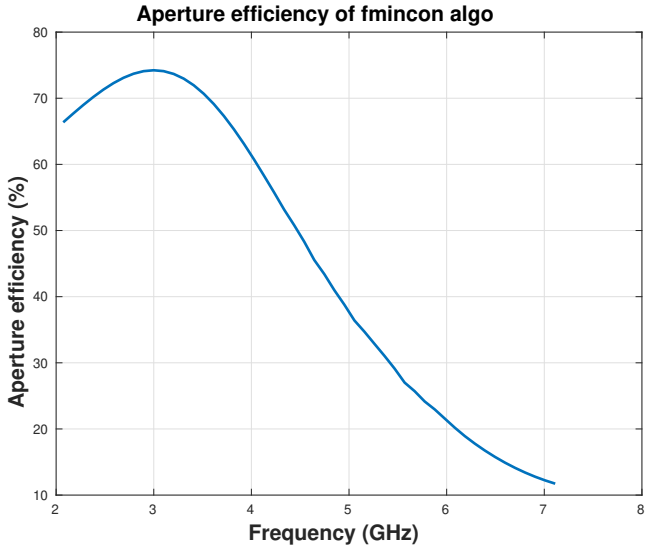

Figure 7.13: Aperture efficiency with frequency for the aperture efficiency optimized antenna profile.

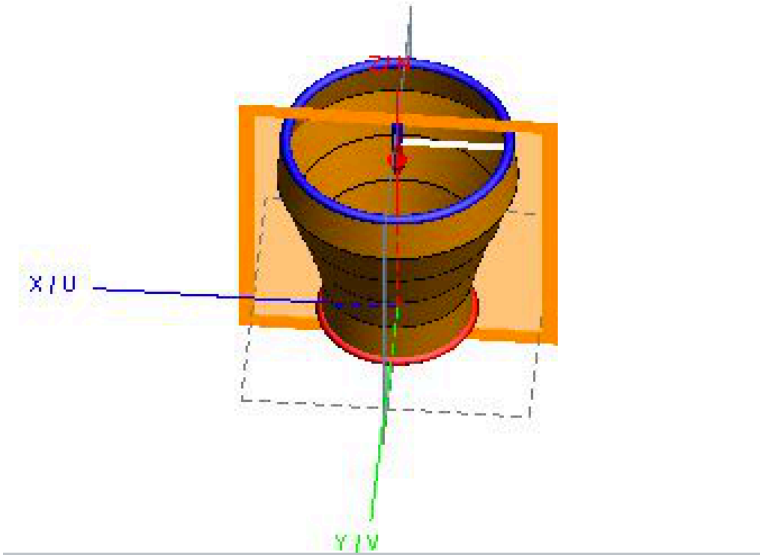

Figure 7.14: Horn profile simulated for frequencies 2.998 GHz in FEKO. The $fmincon$ optimized horn profile for aperture efficiency.

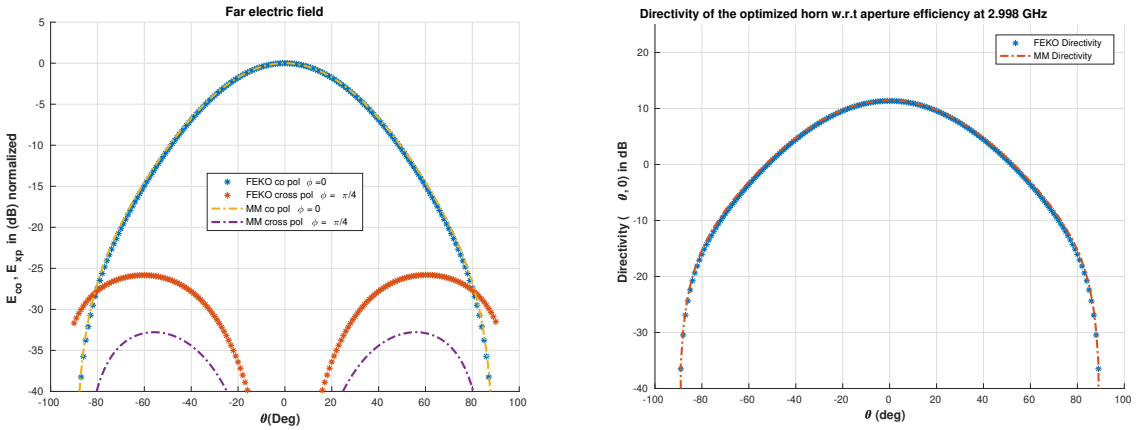

(a) Normalized E-field co- and cross-polar

(b) Directivity

Figure 7.15: Co- and cross-polarized radiation patterns and directivity of $fmincon$ optimized horn profile for aperture efficiency when excited with only the fundamental mode TE_{11}.

8

Conclusions and Recommendations

8.1. Conclusions

This thesis project has been formulated as support activity for the design of compact wide band single pixel feeds (WBSPF) for the SKA1 offset Greogrian dual reflector system. Due to the demanding requirements for the design of such feeds over a large operational bandwidth, high polarimetric purity of the transmitted field and feed compactness, existing software commercial tools require considerable computational time and resources. As the process of optimizing a feed with the current techniques is not feasible with the existing solvers, a new semi-analytical or numerical tool should be developed which can compute the transmitted fields of the feed efficiently. Therefore, the main objective was to build a solver which can find various performance characteristics of smooth walled conical horn antenna feeds efficiently.

The parameters in discussion are the S parameters, the near fields and the far fields. The first contender for the objective was a theoretical full-wave technique called the mode matching technique (MM). In this technique, the conical feed is approximated as a sequential cascaded combination of waveguides with constant cross section. Another contender for the same objective was the JWKB method (Jeffreys-Wentzel–Kramers–Brillouin), which takes into account the slow variations of the waveguide cross section. However, at turning points (discontinuities in the field equations at the evanescent-propagating transitions [30]) , the model doesn't predict the fields very accurately. Therefore, due to the rigorous requirements and robust numerical accuracy, the analytical mode matching technique (MM) was considered for the development.

Based on the mode matching technique, a novel hybrid technique was developed in this thesis. It has got two parts, and those are,

- Mode matching technique to solve the general scattering matrix (GSM) of the conical horn antenna when the far end of the horn is perfectly matched to free space. In a step by step approach, MM software was developed. At first, a two waveguide junction problem was formulated. The GSM was derived for the same problem using integrals which describe the nature of coupling between modes of the waveguides in the junction problem. It was found that only modes having similar azimuthal variations were coupled to one another of the same type (TE/TM). Analytical expressions for the coupling matrices were developed using Bessel function properties. After the development of the MM software to determine the GSM, a cascaded network of waveguides were studied using the same approach. A three waveguide/ and a five waveguide structure were studied. Cascaded MM software is different than the actual MM software because in the cascaded MM software the base is of a three waveguide model. An algorithm was used to iterate over this three waveguide problem to formulate the GSM of a multi waveguide cascade problem.

- The second part of the novel algorithm was the modelling of the aperture free space discontinuity. Among the different methods, using Rumsey's reaction concept, some numerical integrals on the K space were developed to address the problem of this type of discontinuity. These K space integral method assumes that at the discontinuity, higher order modes are excited. This solution existed for rectangular waveguides before and in this thesis it was developed for cylindrical waveguides. The results of the aperture admittance and the reflection coefficients for the mode TE_{11} were compared with Mishustin integrals and the results were very close to each other. The computation of the integrals are a little computationally expensive as they are numerical integrals on the complex plane.

As the reflection from free space-aperture discontinuity was formulated, a hybrid software was created which comprises of both MM and the K space integrals to find different properties of the conical horn antenna. This software first calculates the GSM of the cone and then it computes the aperture reflection coefficients using K space integrals and using both the information it computes the near and far fields of the conical horn antenna. In this software, at the base element of the cone, only the fundamental TE_{11} mode was excited. Therefore, at the aperture, going by the principles of coupling, only modes having the same azimuthal modes were excited. Analytical expressions were developed to compute such far fields (of modes type $TE_{1,n}$). The computation of single mode far field was very fast because there was no need to compute the Fourier transform of the near field in each and every angular far field direction numerically.

The results from the above algorithm were also extensively tested against the commercial software solvers from FEKO/CST MWS. As the nature of the coupling was well analyzed, the computation was very fast to determine the S parameters for a range of frequencies. In commercial tools, solvers like Method of Moments (MoM) and time domain solvers in CST MWS took hours to compute the S parameters, where as the MM software on MATLAB on a MacOS/8GB MEM/with SSD system only took 20 minutes to compute the S parameters over 35 frequency points (Less than a minute per frequency). In MM technique the coupling matrix is frequency independent and only geometry dependent. Therefore, the computation is faster as half of the computation is required to find the coupling between modes and that didn't have to be iterated over all frequency points.

In all commercial solvers, the horn structure is modelled with fine meshgrids. Especially for S parameters and near fields, the mesh has to be very fine as these quantities are sensitive to the geometry of the structure. Therefore, the computation time is non-uniform over the frequency axis. This is due to the fact that the meshing is done with respect to wavelength. At higher frequencies, the wavelengths are shorter, due to which the mesh becomes much finer leading to a higher computation time. There are some differences observed between the MM software results and the commercial tool results. The reason lies in the geometry.

In the developed solver, the geometry of the waveguides are purely cylindrical and due to which not all modes on one side of the waveguide is coupled to all the modes on the other side of the waveguide. However, in commercial tools it appears as if some modes do couple to some extent which were not predicted by the MM software. This is because in commercial tools, the geometry of the waveguides are not purely cylindrical and they comprise of triangular or tetrahedral mesh elements.

Convergence study was also done with increasing number of cylindrical waveguide elements and number of modes (including evanescent modes) on each side of the junction. It was found that the number of modes required to have a very good S parameter pattern was related to the number of propagating modes a certain waveguide can support at the frequency of observation. A conical structure was simulated both in CST and FEKO and the same model was approximated as a cascaded cylindrical waveguide sturcture in the developed software. The results converge to the results of FEKO/CST when the number of cylindrical waveguide elements was increased. Even 25 elements were sufficient in the MM technique to have closer values with FEKO/CST for a frequency band from 5 to 21 GHz.

Using the MM software, near field and far fields were obtained for a perfectly matched waveguide. The knowledge of GSM was used to calculate the near fields on a conical horn antenna as well which is perfectly matched. Using spacial Fourier transform on the field distribution, the far fields were obtained.

The results were analyzed and compared with FEKO models and they came out to be really close to each other. In FEKO the far end of the waveguide used an absorbing boundary condition for perfect matching.

Using the information of the reflection coefficients, the near- and far-fields of a open ended waveguide were studied and compared with FEKO simulations. The results were close to each other except for the near-fields where the results were a little different at the edges as FEKO doesn't ignore the diffraction fields. Near fields were little different but not far fields as far fields are forgiving because they are integral (average) quantities over the near field distribution.

The novel hybrid technique developed in this thesis is computationally very effective to compute the return loss, near field and far fields. The straight forward design of a smooth walled horn assumes a linearly increasing radius over the axis of propagation (in this case z). However, for practical reasons and requirements, the profile of the smooth walled horn can be different.

Therefore, after extensive testing and performance studies, the proposed novel algorithm was used for antenna design via optimization techniques. Different goal functions were created using the novel algorithm as mentioned in Chapter 6 for different requirements for the feeds of SKA 1 offset Gregorian dual reflector systems. The results are put in Chapter 7. The parameters which define the geometry of the horn were kept as design variables for the optimization routines. The variables are the radius of each cylindrical waveguide section, the length of each cylindrical waveguide section and the length of the complete horn antenna. This optimization results show that the developed novel algorithm (solver) serves its purposes and can be used in future to do numerical design of conical horn antennas via optimization techniques.

8.2. Recommendations for future

In the MM software, to calculate the inner cross product, iterations are used for each and every mode on both sides of the junction for a waveguide junction problem. This can't be avoided because the analyical expressions for one mode couple always use Bessel's functions (which are already integral/summation functions). For different mode combinations (different orders of Bessel functions), there is no other efficient way to calculate the inner cross product simultaneously except when parallel processes are used in the computer. These problems are called "embarrassingly parallel". More thoughts can be put forward to make it simultaneous without the use of parallel processes by defining Bessel's functions in a different way. This way, the computation time of S parameters per frequency can further be improved. By extension, it can considerably decrease the simulation time of the optimization routines as callbacks from the goal functions can be much faster.

For the far field computation involving the aperture-free space transition model (even for optimization), only the fundamental (TE_{11}) mode excitation was explored in detail because that is of most interest for the corresponding application. However, analytical methods can be formulated when more than one mode is excited at the base element of the conical waveguide. These patterns can be used to further optimize several parameters of the conical waveguide.

In the thesis, a step wise radius change is used to mimic a smooth walled horn and for that the MM software was developed. However, designing a tapered waveguide using methods like JWKB (Jeffreys-Wentzel–Kramers–Brillouin) approximation [30] can even improve the simulation time further for calculation of the near and far fields of the antenna. In these methods, a smoothly varying conical waveguide (not with steps of cylindrical waveguides) can be analyzed. Different smoothly varying horn profiles also can be analyzed using this technique. A WKB solver when used as goal function also can reduce the simulation time of the optimization routines. The procedure and derivation of the JWKB approximation is given for a conical horn antenna with linearly varying cross section in the appendix E.

A

Derivation of Normalization Constant/Inner Cross product analytical expressions

Normalization constant is a special case of the inner cross product. Normalization constant can be derived from the inner cross product by applying the potential functions for the same mode and the dimensions of only one waveguide. Let's see how the inner cross product is derived.

$$\bar{X} = \int\int_{A_R} \vec{\Phi}^R_{Em} \times \vec{\Phi}^P_{Hn} dS = \int\int_{A_R} \vec{\Phi}^R_{Em}.\vec{\Phi}^P_{En} dS = \int\int_{A_R} \vec{\Phi}^R_{Hm}.\vec{\Phi}^P_{Hn} dS \tag{A.1}$$

For TE/TE mode combinations

$\Rightarrow$

$$\bar{X} = \int\int_{A_R} \vec{\Phi}^R_{Hm}.\vec{\Phi}^P_{Hn} dS = \int\int_{A_R} \nabla\Phi_R.\nabla\Phi_p dS \tag{A.2}$$

$\Rightarrow$

$$\int\int_{A_R} \nabla\Phi_R.\nabla\Phi_p dS = \int\int_{AR} ((\nabla\Phi_R)_\rho(\nabla\Phi_P)_\rho + (\nabla\Phi_R)_\phi(\nabla\Phi_P)_\phi) dS \tag{A.3}$$

$\Rightarrow$

$$\int_0^R \int_0^{2\pi} \left[\beta_{\rho,(pm,pn)}\beta_{\rho(rm,rn)} J'_{pm}(\beta_{\rho,(pm,pn)}\rho) J'_{rm}(\beta_{\rho,(rm,rn)}\rho) \cos(pm\phi)\cos(rm\phi) + \frac{(pm)(rm)}{\rho^2} J_{pm}(\beta_{\rho,(pm,pn)}\rho) J_{rm}(\beta_{\rho,(rm,rn)}\rho) \sin(pm\phi)\sin(rm\phi) \right] \rho d\phi d\rho$$

Getting the terms dependent only on the azimuthal angle (ϕ), we have,

$$\int_0^R \Big[\beta_{\rho,(pm,pn)}\beta_{\rho(rm,rn)}J'_{pm}(\beta_{\rho,(pm,pn)}\rho)J'_{rm}(\beta_{\rho,(rm,rn)}\rho)\Big[\int_0^{2\pi}\cos(pm\phi)\cos(rm\phi)d\phi\Big]+ \frac{(pm)(rm)}{\rho^2}J_{pm}(\beta_{\rho,(pm,pn)}\rho)J_{rm}(\beta_{\rho,(rm,rn)}\rho)\Big[\int_0^{2\pi}\sin(pm\phi)\sin(rm\phi)d\phi\Big]\Big]\rho d\rho$$

For the condition $pm \neq rm$, the integrals $\int_0^{2\pi}\sin(pm\phi)\sin(rm\phi)d\phi$ and $\int_0^{2\pi}\cos(pm\phi)\cos(rm\phi)d\phi$ are 0. Therefore, there is no coupling between modes which have different azimuthal variation. When, the azimuthal variation is the same ($pm == rm$), then the integrals $\int_0^{2\pi}\sin(pm\phi)\sin(rm\phi)d\phi$ and $\int_0^{2\pi}\cos(pm\phi)\cos(rm\phi)d\phi$ are π, which reduces the expressions to,

when, $pm == rm$,

$$\pi\int_0^R \Big[\beta_{\rho,(pm,pn)}\beta_{\rho(pm,rn)}J'_{pm}(\beta_{\rho,(pm,pn)}\rho)J'_{pm}(\beta_{\rho,(pm,rn)}\rho)+\frac{(pm)^2}{\rho^2}J_{pm}(\beta_{\rho,(pm,pn)}\rho)J_{pm}(\beta_{\rho,(pm,rn)}\rho)\Big]\rho d\rho \tag{A.4}$$

The following relations of Bessel's function [2] are used to reduce the expression for the integral.

$$J'_\nu(Z)=\frac{J_{\nu-1}(Z)-J_{\nu+1}(Z)}{2} \tag{A.5}$$

and,

$$\frac{2\nu}{Z}J_\nu(Z)=J_{\nu-1}(Z)+J_{\nu+1}(Z) \tag{A.6}$$

Therefore, the integral in A.4 becomes,

$$\bar{X}=\frac{\pi\beta_{\rho,(pm,pn)}\beta_{\rho,(pm,rn)}}{2}\int_0^R\Big(J_{pm-1}(\beta_{\rho,(pm,pn)}\rho)J_{pm-1}(\beta_{\rho,(pm,rn)}\rho)+J_{pm+1}(\beta_{\rho,(pm,pn)}\rho)J_{pm+1}(\beta_{\rho,(pm,rn)}\rho)\Big)\rho d\rho \tag{A.7}$$

These integrals can be solved by the Lommel's integrals of the form (3.85) [2]. Similar expression can be formed for the combination of TM/TM as well. In all these above integrals the limit R is the radius of the smaller waveguide R.

TE/TM: TM on the smaller waveguide and TE in the larger waveguide

$$\bar{X}=\int\int_{A_R}(\nabla_t\Phi_R\times\nabla_t\Phi_P).\hat{z}dS \tag{A.8}$$

$$\bar{X}=\int\int_{A_R}\begin{pmatrix}\hat{\rho} & \hat{\phi} & \hat{z}\\ -\beta_{\rho(rm,rn)}J'_{rm}(\beta_{\rho(rm,rn)}\rho)\cos(rm\phi) & \frac{rm}{\rho}J_{rm}(\beta_{\rho(rm,rn)}\rho)\sin(rm\phi) & 0\\ \beta_{\rho(pm,pn)}J'_{pm}(\beta_{\rho(pm,pn)}\rho)\cos(pm\phi) & -\frac{pm}{\rho}J_{pm}(\beta_{\rho(pm,pn)}\rho)\sin(pm\phi) & 0\end{pmatrix}.\hat{z} \tag{A.9}$$

$\Rightarrow$

$$\bar{X} = \int\int_{A_R} \Big(- \beta_{\rho(pm,pn)} \frac{pm}{\rho} J'_{pm}(\beta_{\rho(pm,pn)}\rho) \cos(pm\phi) J_{rm}(\beta_{\rho(rm,rn)}\rho) \sin(rm\phi) + \beta_{\rho(rm,rn)} J'_{rm}(\beta_{\rho(rm,rn)}\rho) \cos(rm\phi) J_{pm}(\beta_{\rho(pm,pn)}\rho) \sin(pm\phi) \Big) dS$$

$$\bar{X} = I_1 - I_2 \tag{A.10}$$

The terms in this integral can be divided into two independent integrals (with ρ and ϕ)

$\Rightarrow$

$$I_1 = pm \int_0^{rr} \frac{1}{\rho} \frac{d(J_{rm}(\beta_{\rho(rm,rn)}\rho))}{d\rho} J_{pm}(\beta_{\rho(pm,pn)}\rho) \rho d\rho \int_0^{2\pi} \cos(rm\phi) \sin(pm\phi) d\phi = pm I_{11} I_{12} \tag{A.11}$$

Where $I_{11} = \int_0^{rr} \frac{d(J_{rm}(\beta_{\rho(rm,rn)}\rho))}{d\rho} J_{pm}(\beta_{\rho(pm,pn)}\rho) d\rho$ and $I_{12} = \int_0^{2\pi} \cos(rm\phi) \sin(pm\phi) d\phi$.

Similarly,

$$I_2 = rm \int_0^{rr} \frac{1}{\rho} \frac{d(J_{pm}(\beta_{\rho(pm,pn)}\rho))}{d\rho} J_{rm}(\beta_{\rho(rm,rn)}\rho) \rho d\rho \int_0^{2\pi} \cos(pm\phi) \sin(rm\phi) d\phi = rm I_{21} I_{22} \tag{A.12}$$

Where $I_{21} = \int_0^{rr} \frac{d(J_{pm}(\beta_{\rho(pm,pn)}\rho))}{d\rho} J_{rm}(\beta_{\rho(rm,rn)}\rho) d\rho$ and $I_{22} = \int_0^{2\pi} \cos(pm\phi) \sin(rm\phi) d\phi$

It is interesting to note that I_{12} and I_{22} are always 0 and therefore, the inner cross product is also 0. However, just for interest, let's calculate the other two integrals I_{11} and I_{21}.

$$I_{11} = \int_0^{rr} \frac{d(J_{rm}(\beta_{\rho(rm,rn)}\rho))}{d\rho} J_{pm}(\beta_{\rho(pm,pn)}\rho) d\rho \tag{A.13}$$

Integrating by parts, we have,

$$I_{11} = \Big[J_{rm}(\beta_{\rho(rm,rn)}\rho) J_{pm}(\beta_{\rho(pm,pn)}\rho) \Big]_0^{rr} - \int_0^{rr} \frac{d(J_{pm}(\beta_{\rho(pm,pn)}\rho))}{d\rho} J_{rm}(\beta_{\rho(rm,rn)}\rho) d\rho \tag{A.14}$$

As waveguide R has a TM mode, by equation (2.32), we know that $J_{rm}(\beta_{\rho(rm,rn)} rr) = 0$ and when $pm = rm \neq 0$, we know that Bessel functions at $\rho = 0$ are 0. Therefore, the first term in the above equation (A.14), $\Big[J_{rm}(\beta_{\rho(rm,rn)}\rho) J_{pm}(\beta_{\rho(pm,pn)}\rho) \Big]_0^{rr} = 0$. Furthermore, the second term of equation (A.14) interestingly is I_{21} which also we want to find out as a part of I_2. Therefore, equation (A.14) becomes,

$$I_{11} = -I_{21} \tag{A.15}$$

$\Rightarrow$

$$I_{11} + I_{21} = 0 \tag{A.16}$$

As we have the equation with the sum of the two terms we need to figure out, let's subtract these two integrals and find another equation with these two unknowns.

$$I_{11} - I_{21} = \int_0^{rr} \left(\frac{d(J_{rm}(\beta_{\rho(rm,rn)}\rho))}{d\rho} J_{pm}(\beta_{\rho(pm,pn)}\rho) + \frac{d(J_{pm}(\beta_{\rho(pm,pn)}\rho))}{d\rho} J_{rm}(\beta_{\rho(rm,rn)}\rho) \right) d\rho \tag{A.17}$$

$\Longrightarrow$

$$I_{11} - I_{21} = \int_0^{rr} \left(\frac{d(J_{rm}(\beta_{\rho(rm,rn)}\rho) J_{pm}(\beta_{\rho(pm,pn)}\rho))}{d\rho} \right) d\rho \tag{A.18}$$

$\Longrightarrow$

$$I_{11} - I_{21} = \left[J_{rm}(\beta_{\rho(rm,rn)}\rho) J_{pm}(\beta_{\rho(pm,pn)}\rho) \right]_0^{rr} = 0 \tag{A.19}$$

As the sum and difference of I_{11} and I_{21} both are 0, the values of I_{11} and I_{21} are 0. Therefore, I_1 and I_2 both are 0 and the inner cross product is 0.

B

Results of S parameters of higher order modes using Mode Matching Technique

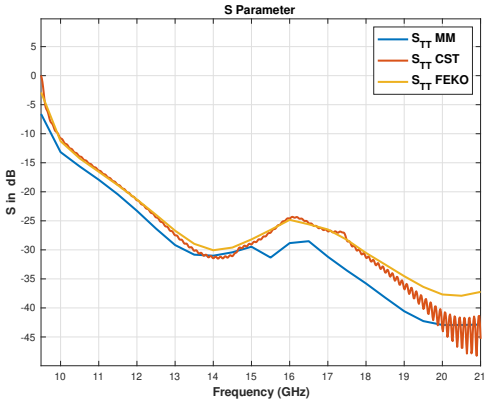

(a) S_{TT} of TE_{01}

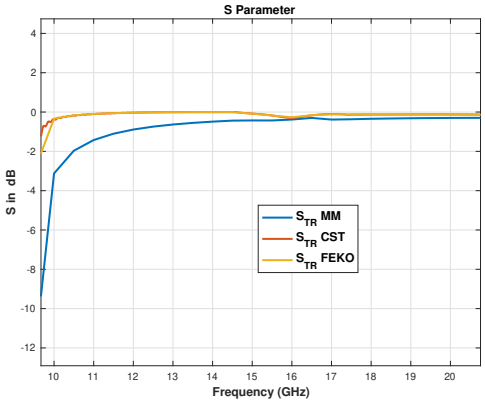

(b) S_{TR} of TE_{01}

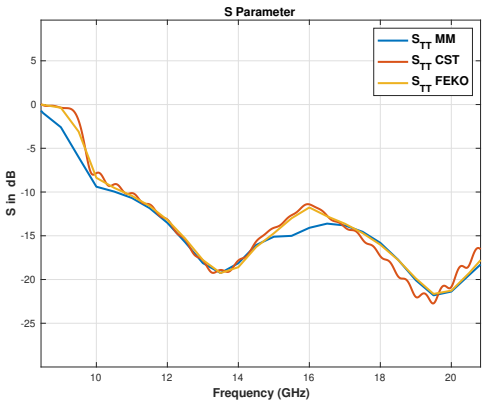

(c) S_{TT} of TM_{11}

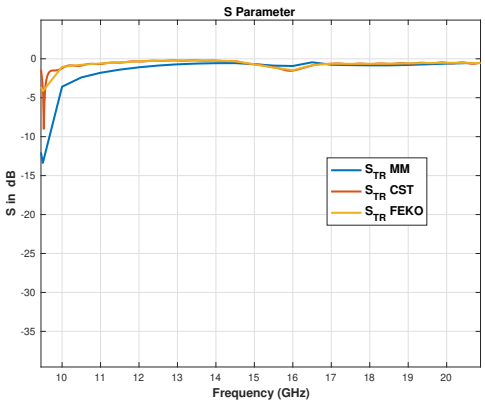

(d) S_{TR} of TM_{11}

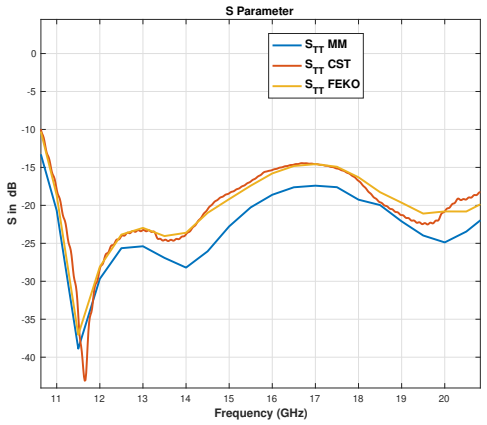

(e) S_{TT} of TE_{31}

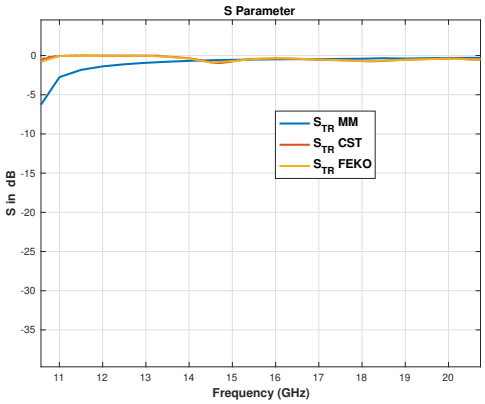

(f) S_{TR} of TE_{31}

Figure B.1: Reflection and Transmission coefficients of the 5 waveguide structure for different modes

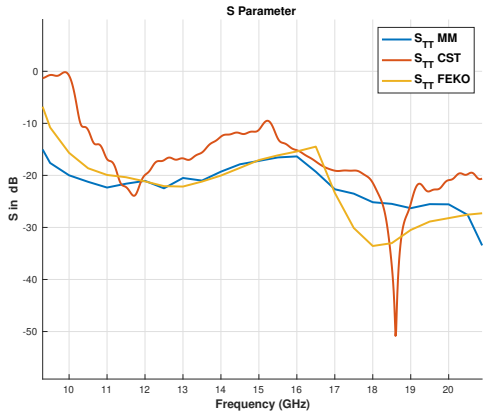

(a) S_{TT} of TE_{01}

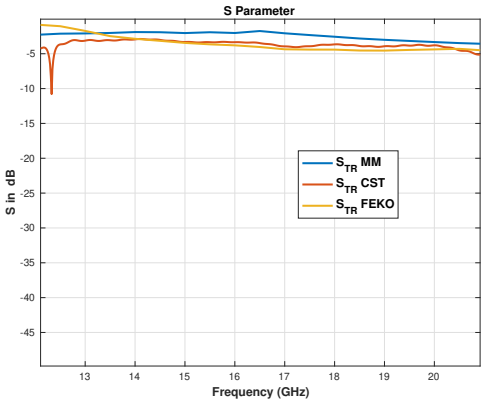

(b) S_{TR} of TE_{01}

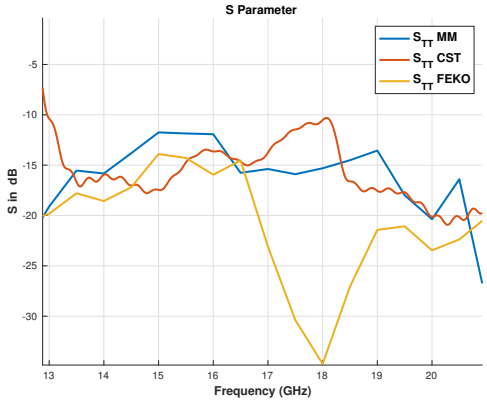

(c) S_{TT} of TM_{11}

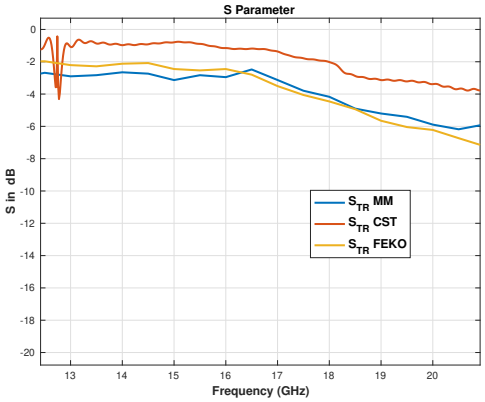

(d) S_{TR} of TM_{11}

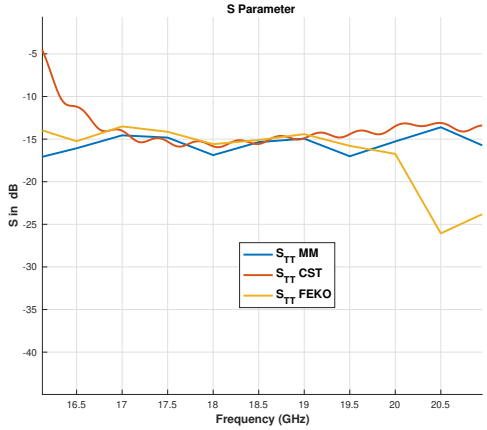

(e) S_{TT} of TM_{21}

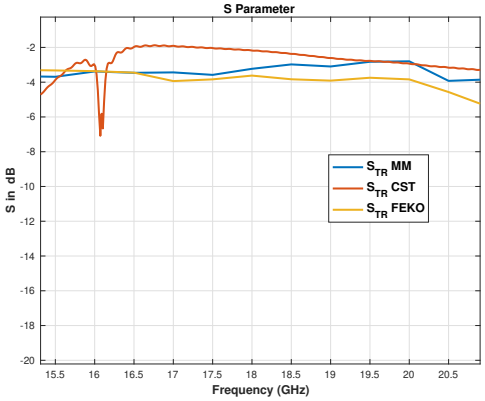

(f) S_{TR} of TM_{21}

Figure B.2: Reflection and Transmission coefficients of the Cone structure in 4.11. For MM, there are 30 cylindrical waveguides inside.

C

Spectrum function of the electric fields in a circular waveguide when excited with a mode of kind TE_{1n}

For the x component, the spectrum function looks like the following (Without the amplitude term)

$$ö_{1n}^{TE}(k_\Omega, \Theta) = \int_0^R \left(\left(\frac{1}{\rho} J_1(\beta_{\rho,(1,n)}\rho) - \beta_{\rho,(1,n)} J_1'(\beta_{\rho,(1,n)}\rho) \right) \left(\int_0^{2\pi} \sin\phi \cos\phi e^{k_\Omega \rho \cos(\phi-\Theta)} d\phi \right) \rho d\rho \right) \quad \text{(C.1)}$$

The following identities of Bessel functions are used to solve the above integral.

$$J_\nu'(Z) = \frac{J_{\nu-1}(Z) - J_{\nu+1}(Z)}{2} \quad \text{(C.2)}$$

and,

$$\frac{2\nu}{Z} J_\nu(Z) = J_{\nu-1}(Z) + J_{\nu+1}(Z) \quad \text{(C.3)}$$

Therefore C.1 looks like,

$$ö_{1n}^{TE}(k_\Omega, \Theta) = \int_0^R \left(\beta_{\rho,(1,n)} J_2(\beta_{\rho,(1,n)}\rho) \left(\int_0^{2\pi} \frac{1}{2} Imag(e^{j2\phi}) e^{k_\Omega \rho \cos(\phi-\Theta)} d\phi \right) \rho d\rho \right) \quad \text{(C.4)}$$

Using the following identity of Bessel integrals and as these work for any interval which spans over a period (2π), the above problem can be solved.

$$J_l(\beta) = \frac{1}{2\pi j^l} \int_0^{2\pi} e^{jl\phi} e^{j\beta\cos\phi} d\phi \quad \text{(C.5)}$$

The solution to C.4 then can be written as,

$$ö_{1n}^{TE}(k_\Omega, \Theta) = \int_0^R \left(\beta_{\rho,(1,n)} J_2(\beta_{\rho,(1,n)}\rho) Imag\left(e^{j2\Theta} \left(\int_0^{2\pi} \frac{1}{2} e^{j2(\phi-\Theta)} e^{k_\Omega \rho \cos(\phi-\Theta)} d\phi \right) \right) \rho d\rho \right) \quad \text{(C.6)}$$

Substituting $\zeta = \phi - \Theta$, we have,

$$ö_{1n}^{TE}(k_\Omega, \Theta) = \int_0^R \left(\beta_{\rho,(1,n)} J_2(\beta_{\rho,(1,n)}\rho) Imag\left(e^{j2\Theta} \left(\int_{-\Theta}^{2\pi-\Theta} \frac{1}{2} e^{j2\zeta} e^{k_\Omega \rho \cos(\zeta)} d\zeta \right) \right) \rho d\rho \right) \quad (C.7)$$

$\Rightarrow$

$$ö_{1n}^{TE}(k_\Omega, \Theta) = -\int_0^R \left(\beta_{\rho,(1,n)} J_2(\beta_{\rho,(1,n)}\rho) Imag\left(e^{j2\Theta} \pi J_2(k_\Omega \rho) \right) \rho d\rho \right) \quad (C.8)$$

$\Rightarrow$

$$ö_{1n}^{TE}(k_\Omega, \Theta) = -\int_0^R \left(\beta_{\rho,(1,n)} J_2(\beta_{\rho,(1,n)}\rho) Imag\left(e^{j2\Theta} \pi J_2(k_\Omega \rho) \right) \rho d\rho \right) \quad (C.9)$$

$\Rightarrow$

$$ö_{1n}^{TE}(k_\Omega, \Theta) = -\int_0^R \left(\beta_{\rho,(1,n)} J_2(\beta_{\rho,(1,n)}\rho) \sin(2\Theta) \pi J_2(k_\Omega \rho) \rho d\rho \right) \quad (C.10)$$

Therefore,

$$ö_{1n}^{TE}(k_\Omega, \Theta) = -\pi \beta_{\rho,(1,n)} \sin(2\Theta) \int_0^R J_2(\beta_{\rho,(1,n)}\rho) J_2(k_\Omega \rho) \rho d\rho \quad (C.11)$$

The integral can be solved by Lommel's integral of the kind (3.85) [2]. $\Rightarrow$

$$ö_{1n}^{TE}(k_\Omega, \Theta) = -\pi \beta_{\rho,(1,n)} \sin(2\Theta) I_{22}^{1,n}(k_\Omega) \quad (C.12)$$

For the y component, the spectrum function looks like the following (without amplitude term)

$$ü_{1n}^{TE}(k_\Omega, \Theta) = \int\int_{S_{ap}} \left[\left(\frac{1}{\rho} J_1(\beta_{\rho,(1,n)}\rho) \sin^2\phi + \beta_{\rho,(1,n)} J_1'(\beta_{\rho,(1,n)}\rho) \cos^2\phi \right) \right] e^{k_\Omega \rho \cos(\phi - \Theta)} \rho d\rho d\phi \quad (C.13)$$

Using trigonometric properties ($\sin^2\phi = \frac{1-\cos(2\phi)}{2}$ and $\cos^2\phi = \frac{1+\cos(2\phi)}{2}$)

$$ü_{1n}^{TE}(k_\Omega, \Theta) = \int\int_{S_{ap}} \frac{1}{2} \left(\frac{1}{\rho} J_1(\beta_{\rho,(1,n)}\rho) + \beta_{\rho,(1,n)} J_1'(\beta_{\rho,(1,n)}\rho) + \cos(2\phi)\left(-\frac{1}{\rho} J_1(\beta_{\rho,(1,n)}\rho) + \beta_{\rho,(1,n)} J_1'(\beta_{\rho,(1,n)}\rho) \right) \right) e^{k_\Omega \rho \cos(\phi - \Theta)} \rho d\rho d\phi$$

Using the Bessel function properties of C.2 and C.3,

$\Rightarrow$

$$\ddot{u}_{1n}^{TE}(k_\Omega,\Theta)=\int_0^R \frac{\beta_{\rho,(1,n)}}{4}\Big(\int_0^{2\pi}(2J_0(\beta_{\rho,(1,n)}\rho)-2J_2(\beta_{\rho,(1,n)}\rho)\cos(2\phi))e^{k_\Omega\rho\cos(\phi-\Theta)}d\phi\Big)\rho d\rho \quad (C.14)$$

$$\ddot{u}_{1n}^{TE}(k_\Omega,\Theta)=\int_0^R \frac{\beta_{\rho,(1,n)}}{2}\Big(J_0(\beta_{\rho,(1,n)}\rho)\int_{-\Theta}^{2\pi-\Theta} e^{j0\zeta}e^{k_\Omega\rho\cos(\zeta)}d\zeta - J_2(\beta_{\rho,(1,n)}\rho)Real\Big(e^{j2\Theta}\int_{-\Theta}^{2\pi-\Theta}e^{j2\zeta}e^{k_\Omega\rho\cos(\zeta)}d\zeta\Big)\Big)\rho d\rho$$

Using the identity of Bessel function in C.5, we have,

$$\ddot{u}_{1n}^{TE}(k_\Omega,\Theta)=\beta_{\rho,(1,n)}\pi\int_0^R\Big(J_0(\beta_{\rho,(1,n)}\rho)J_0(k_\Omega\rho)+J_2(\beta_{\rho,(1,n)}\rho)J_2(k_\Omega\rho)\cos(2\Theta)\Big)\rho d\rho \quad (C.15)$$

$\Longrightarrow$

$$\ddot{u}_{1n}^{TE}(k_\Omega,\Theta)=\beta_{\rho,(1,n)}\pi\int_0^R\Big(J_0(\beta_{\rho,(1,n)}\rho)J_0(k_\Omega\rho)+J_2(\beta_{\rho,(1,n)}\rho)J_2(k_\Omega\rho)\cos(2\Theta)\Big)\rho d\rho \quad (C.16)$$

$$\ddot{u}_{1n}^{TE}(k_\Omega,\Theta)=\pi\beta_{\rho,(1,n)}(I_{00}^{1,n}(k_\Omega)+\cos(2\Theta)I_{22}^{1,n}(k_\Omega)) \quad (C.17)$$

D

Time Complexity of different methods

Solver	Tool	Conf	RAM (GB)	Freq Points	CPU Time (hr)	Run Time (hr)	Memory Needed (GB)	Peak Memory (GB)	Parallel Processes
MoM	FEKO	2wg	256 Lin	35	105.751	2.65	5.361	2.5	40
MM	MATLAB	2wg	8 Mac	35	0.3	0.3			1
TD	CST	2wg	8 Win	1001	3	3		1.5	4 threads
MoM	FEKO	5wg	256 Lin	35	295.108	7.378	14.843	0.382	40
MM	MATLAB	5wg	128 Lin	35		0.6064			12
TD	CST	5wg	8 Win	1001	18			2.5	4 threads
MoM	FEKO	Cone	256 Lin	33	3557	89.661	88.705	2.234	40
MM	MATLAB	Cone	128 Lin	35		6.97			12

Table D.1: Time and resource comparison among different methods/solvers

Terms	Meaning
MoM	Method of Moments
MM	Mode Matching
TD	Time Domain
CPU	Central Processing Unit
Lin	Linux
Mac	Mac OS
Win	Windows PC
RAM	Random Access Memory
GB	Giga Byte

Table D.2: Meaning of terms in table D.1

E

JWKB approach to solve near and far fields of a conical horn antenna

From chapter 3 to 5, the parameters like the reflection coefficients, transmission coefficients, near-fields and the far-fields, of a conical horn antenna approximated as a cascaded combination of cylindrical waveguides are derived. In this appendix, another approach is discussed by virtue of which different parameters of a perfectly matched conical horn antenna can be determined without assuming it to be a cascaded structure of cylindrical waveguides. The approach is called as the JWKB approximation (Jeffreys-Wentzel-Kramers-Brillouin) [30]. The JWKB approximation was developed to solve the one dimensional time independent Schrödinger's equation [25] of quantum mechanics. With this approach, the conical horn antenna should have a slowly increasing cross section. Using this approach, near- and far-fields are determined in this chapter.

E.1. JWKB approximation for a slowly varying cross section of a conical waveguide

Using equation (2.8) again, we have,

$$\frac{\partial^2 h}{\partial z^2} + \beta_z^2(z)h = 0 \tag{E.1}$$

Solution to this equation was a phase term ($e^{-j\beta_z z}$) in chapter 2 as the term β_z was constant over the axis z for a cylindrical waveguide. However, as in this case, we assume a slowly varying profile, the propagation constant β_z now depends on z.

$$\beta_z(z) = -1j\sqrt{-(\beta^2 - \beta_\rho^2(z))} = -1j\sqrt{-(\beta^2 - \left(\frac{\chi_{m,n} \quad Or \quad \chi'_{m,n}}{r(z)}\right)^2)} \tag{E.2}$$

Where $\chi_{m,n}$ and $\chi'_{m,n}$ are used for TM and TE modes respectively. The $\chi_{m,n}$ is the n'th zero of the m'th order Bessel function of the first kind. $\chi'_{m,n}$ is the n'th zero of the derivative of the m'th order Bessel function of the first kind. The quantity $r(z)$ is the variation of the radius with respect to z.

If the term $\beta_z^2(z)$ is assumed to be a slowly varying function in this case. Therefore, a crude approximation that $\beta_z^2(z)$ is constant leads to a solution which look like the following.

$$h(z) = e^{j\eta(z)} \tag{E.3}$$

Therefore, the differential equation of E.1 can be rewritten as,

$$-(\eta')^2 + j\eta'' + \beta_z^2 = 0 \tag{E.4}$$

If η'' is very small, the above relation can become an approximation and that is,

$$\eta' = \pm\beta_z \tag{E.5}$$

$\Rightarrow$

$$\eta(z) = \pm\int \beta_z(z)dz \tag{E.6}$$

Therefore, the condition for validity is,

$$|\eta''| = \frac{1}{2}\left|\frac{(\beta_z^2)'}{\beta_z}\right| << |\beta_z^2| \tag{E.7}$$

Therefore, the validity condition can be simplified as,

$$|\beta_z'(z)| << \beta_z^2 \tag{E.8}$$

Furthermore, there is a relation between the flare angle and the wavelength that has to be satisfied [30].

$$\frac{R_s(2\theta_f)^2}{8} << \lambda \tag{E.9}$$

Where R_s, θ_f are defined in the figure E.1.

Substituting the approximation of equation (E.7) into equation (E.4), we have,

$$(\eta')^2 = \beta_z^2 \pm \frac{j}{2}\frac{(\beta_z^2)'}{\beta_z} \tag{E.10}$$

$\Rightarrow$

$$\eta' = \pm\beta_z + \frac{j}{4}\frac{(\beta_z^2)'}{\beta_z^2} \tag{E.11}$$

$$\eta(z) = \pm\int \beta_z(z)dz + \frac{j}{4}\ln\beta_z^2 \tag{E.12}$$

Using this in equation (6.3), we have,

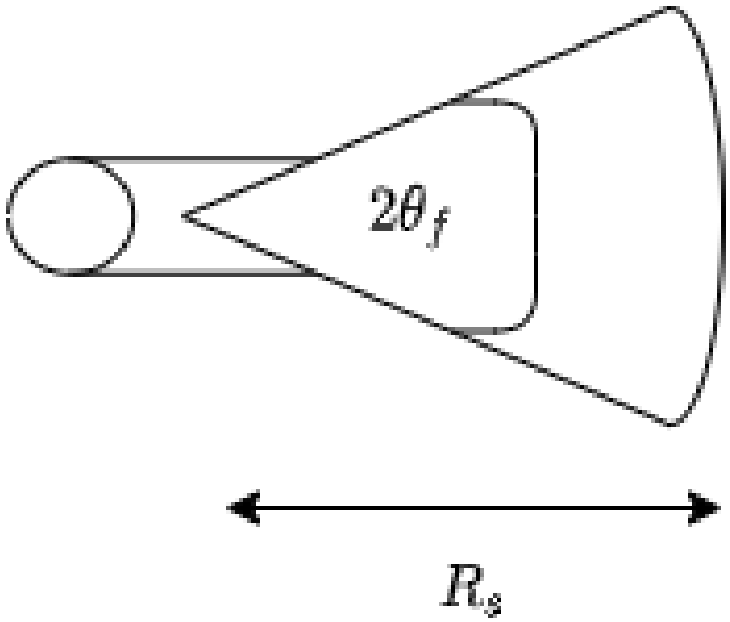

Figure E.1: Conical waveguide with slowly varying cross section

$$h(z) = \frac{1}{\sqrt{\beta_z}}\left[Ae^{j\int \beta_z(z)dz} + Be^{-j\int \beta_z(z)dz}\right] \tag{E.13}$$

The square root of propagation constant in the denominator of equation (E.13) suggests that the function $h(z)$ has a singularity at the places on z axis where a mode is excited. It is the point after which (towards the increasing size of the flare) a cylindrical waveguide mode becomes propagating and before which the cylindrical waveguide mode is evanescent. These points are also called as the turning points. There are several techniques to avoid that singularity by using connection formulae. However, in this thesis, as the aperture fields are of higher priority, there is no need to find the fields everywhere on the z axis. If at the far end of the antenna, there is another cylindrical waveguide connected in cascade, possible turning points near the aperture also can be avoided.

Therefore, using only one term from the equation (6.13), we have,

$$h(z) = \frac{B}{\sqrt{\beta_z}}e^{-j\int \beta_z(z)dz} \tag{E.14}$$

The negative exponential is chosen to satisfy the propagation condition. The integral above the exponential is done from the aperture till the point where a certain waveguide mode is excited on the z axis. Here, the aperture is considered as $z = 0$ and the point on z axis where a certain mode is excited is denoted as $z = d$. Therefore, the potential functions for TE/TM (mentioned in chapter 2) can be written as for the flared antenna case,

$$F_z/A_z(\rho, \phi, z) = A_{m,n}J_m(\beta_\rho \rho)C_2 \cos(m\phi)\frac{B}{\sqrt{\beta_z}}e^{-j\int \beta_z(z)dz} \tag{E.15}$$

The field equations mentioned in chapter 2 remain the same with the exponential term replaced with $h(z)$. In the case of TM electric field modes and TE magnetic field modes the derivatives with z are only carried out for the $h(z)$ term and not with the terms varying with ρ and ϕ to get simplified expressions.

The integral on the exponential function of $h(z)$ can be found analytically for the conical waveguide. The integral is defined as,

$$\int_0^{-d} \beta_z(z)dz = \int_0^{-d} \sqrt{(\beta^2 - \left(\frac{\chi_{m,n} \quad Or \quad \chi'_{m,n}}{r(z)}\right)^2)dz} \tag{E.16}$$

$\Rightarrow$

Where, $r(z) = r_{top} + z\tan\theta_f$. r_{top} is the top radius of the cone. Therefore,

$$\int_0^{-d} \beta_z(z)dz = \int_0^{-d} \sqrt{(\beta^2 - \left(\frac{\chi_{m,n} \quad Or \quad \chi'_{m,n}}{r_{top} + z\tan\theta_f}\right)^2)dz} \tag{E.17}$$

Substituting $r_{top} + z\tan\theta_f$ as u, we have,

$$\int_{r_{top}}^{r_{top} - d\tan\theta_f} \sqrt{(\beta^2 - \left(\frac{\chi_{m,n} \quad Or \quad \chi'_{m,n}}{u}\right)^2)}\frac{du}{\tan\theta_f} \tag{E.18}$$

$\Rightarrow$

$$\beta\int_{r_{top}}^{r_{top} - d\tan\theta_f} \sqrt{(1 - \left(\frac{\chi_{m,n} \quad Or \quad \chi'_{m,n}}{\beta u}\right)^2)}\frac{du}{\tan\theta_f} \tag{E.19}$$

Again substituting $\Psi = \arccos(\frac{\chi_{m,n} \quad Or \quad \chi'_{m,n}}{\beta u})$, we have,

$$\beta\int_{\Psi_1}^{\Psi_2} \tan^2\Psi\frac{d\Psi}{\tan\theta_f} \tag{E.20}$$

Where,

$$\Psi_1 = arccos\frac{\chi_{m,n} \quad Or \quad \chi'_{m,n}}{\beta r_{top}} \tag{E.21}$$

$$\Psi_2 = \arccos\frac{\chi_{m,n} \quad Or \quad \chi'_{m,n}}{\beta(r_{top} - d\tan\theta_f)} \tag{E.22}$$

Therefore, the integral can be found as,

$$\beta\int_{\Psi_1}^{\Psi_2} \tan^2\Psi\frac{d\Psi}{\tan\theta_f} = \frac{\beta}{\tan\theta_f}[\tan\Psi - \Psi]_{\Psi_1}^{\Psi_2} = \frac{\beta}{\tan\theta_f}[(\tan\Psi_2 - \Psi_2) - (\tan\Psi_1 - \Psi_1)] \tag{E.23}$$

Bibliography

[1] Volum E 94, Num B Er, June 15, and V H Rumsey. P H YS I CAL R'EVI EW Reaction Concept in Electromagnetic Theory. Technical report.

[2] M Abramowitz. *Handbook of Mathematical Functions with Formulas, Graphs and Mathematical Tables*. National Bureau of Standards. Applied Mathematics Series, 55 edition, 1972.

[3] Constantine A Balanis. *Advanced engineering electromagnetics*. J. Wiley & Sons, 2012.

[4] Theunis Steyn Beukman and P Meyer. Modal-Based Design Techniques for Circular Quadruple-Ridged Flared Horn Antennas. Technical report, 2015. URL `https://scholar.sun.ac.za`.

[5] Frank Bowman. *Introduction to Bessel functions*. Dover, 2018.

[6] M C Buizey and S N Sumaddur. Input Admittance of a Circular Waveguide Aperture Covered by a Dielectric Slab. Technical report.

[7] M C Buizey, S N Sumaddur, and Calvin T Swift. E " ELECTROMAGNETIC PROPERTIES OF A CIRCULAR APERTURE IN A DIELECTRIC-COVERED OR UNCOVERED GROUND PLANE. Technical report. URL `https://ntrs.nasa.gov/search.jsp?R=19680026065`.

[8] German Cortes-Medellin. Non-planar quasi-self-complementary ultra-wideband feed antenna. *IEEE Transactions on Antennas and Propagation*, 59(6 PART 1):1935–1944, 6 2011. ISSN 0018926X. doi: 10.1109/TAP.2011.2122226.

[9] Bin Dong, Jian Yang, Jens Dahlstrom, Jonas Flygare, Miroslav Pantaleev, and Bhushan Billade. Optimization and Realization of Quadruple-Ridge Flared Horn with New Spline-Defined Profiles as a High-Efficiency Feed from 4.6 GHz to 24 GHz. *IEEE Transactions on Antennas and Propagation*, 67(1):585–590, 1 2019. ISSN 0018926X. doi: 10.1109/TAP.2018.2874673.

[10] Okan K. Ersoy. *Diffraction, fourier optics, and imaging*. Wiley-Interscience, 2007. ISBN 0471238163.

[11] Rohit Gawande and Richard Bradley. Towards an ultra wideband low noise active sinuous feed for next generation radio telescopes. *IEEE Transactions on Antennas and Propagation*, 59(6 PART 1):1945–1953, 6 2011. ISSN 0018926X. doi: 10.1109/TAP.2011.2122238.

[12] Alexander K. Hartmann and Heiko. Rieger. *Optimization algorithms in physics*. Wiley-VCH, 2002. ISBN 3527403078.

[13] D J Hoppe. Modal analysis applied to circular, rectangular, and coaxial waveguides. *The Telecommunications and Data Acquisition Report; p. p 89-96*, 1988.

[14] PER-SIMON KLLDAL. Factorization of the Feed Efficiency of Paraboloids and Cassegrain Antennas. *EEE Transactions on Antennas and Propagation*, 33(8):903–908, 1985. doi: 10.1109/TAP.1985.1143689.

[15] Harold Levine and Julian Schwinger. PH YSICAL REVI EW On the Theory of Diffraction by an Ayerture in an Infinite Plane Screen. II. Technical report, 1949.

[16] Arthur C. Ludwig. The Definition of Cross Polarization. *IEEE Transactions on Antennas and Propagation*, 21(1):116–119, 1973. doi: 10.1109/TAP.1973.1140406.

[17] Robert H. MacPhie and Ke Li Wu. A Plane Wave Expansion of Spherical Wave Functions for Modal Analysis of Guided Wave Structures and Scatterers. *IEEE Transactions on Antennas and Propagation*, 51(10 II):2801–2805, 10 2003. ISSN 0018926X. doi: 10.1109/TAP.2003.818009.

[18] Darragh Mccarthy, Neil Trappe, and A Murphy. *Investigation of Horn Optimisation, Simulation and Measurement Techniques, with Application to Integrating Cavity Based Pixel Design*. PhD thesis, 2014.

[19] B A Mishustin. RADIATION FROM THE APERTURE OF A CIRCULAR WAVEGUIDE WITH AN INFINITE FLANGE. Technical Report 6, 1965.

[20] Mauro Mongiardo, Peter Russer, Roberto Sorrentino, and Cristiano Tomassoni. Spherical Mode Expansions for Flange-mounted Waveguide Apertures. Technical report.

[21] Agostino Monorchio, Raj Mittra, and Giuliano Manara. Generalized Scattering Matrix Technique. *Encyclopedia of RF and Microwave Engineering*, 2005. doi: 10.1002/0471654507.eme145.

[22] Abderrahem Moumen. *Analysis and synthesis of compact feeds for large multiple-beam reflector antennas*. PhD thesis, TU Delft, 2001.

[23] A.p. Orfanidis, G.a. Kyriacou, and J.n. Sahalos. A mode-matching technique for the study of circular and coaxial waveguide discontinuities based on closed-form coupling integrals. *IEEE Transactions on Microwave Theory and Techniques*, 48(5):880–883, 2000. doi: 10.1109/22.841894.

[24] Miroslav Pantaleev. ADVANCED INSTRUMENTATION PROGRAM WIDE BAND SINGLE PIXEL FEEDS. Technical report. URL www.skatelescope.org.

[25] Roger Penrose. *The road to reality: A complete guide to the laws of the universe*. Random house, 2006.

[26] J M Reiter and F Arndt. ANALYSIS OF CIRCULAR WAVEGUIDE ANTENNAS INCLUDING TIIE OUTER WALL GEOMETRY WIT11 A SPIIERICAGWAVE FORMULATION OF THE BOUNDARY CONTOUR-MODE-MATCHING METIIOD. Technical report, .

[27] J M Reiter and F Arndt. Full-Wave Analysis of Circular Waveguide Horn Antennas Including the Outer Wall Geometry with an Hybrid MM/BCMM Method. Technical report, .

[28] Jorge A Ruiz-Cruz, Jose R Montejo-Garai, and Jesus M Rebollar. Computer Aided Design of Waveguide Devices by Mode-Matching Methods. In Vitaliy Zhurbenko, editor, *Passive Microwave Components and Antennas*, chapter 6. IntechOpen, Rijeka, 2010. doi: 10.5772/9403. URL https://doi.org/10.5772/9403.

[29] Marvin G. Schorr and Fred J. Beck. Electromagnetic field of the conical horn. *Journal of Applied Physics*, 21(8):795–801, 1950. ISSN 00218979. doi: 10.1063/1.1699761.

[30] J W Silvestro and R E Collin. Aperture impedance of flared horns Indexing terms: Antennas (aperture), Antennas (horns and feeds). Technical report.

[31] Tak Sum Chu and T Itoh. Generalized Scattering Matrix Method for Analysis of Cascaded and Offset Microstrip Step Discontinuities. *IEEE Transactions on Microwave Theory and Techniques*, 34(2):280–284, 2 1986. ISSN 1557-9670. doi: 10.1109/TMTT.1986.1133323.

[32] Neil Trappe, J. Anthony Murphy, Stafford Withington, and Willem Jellema. Gaussian beam mode analysis of standing waves between two coupled corrugated horns. *IEEE Transactions on Antennas and Propagation*, 53(5):1755–1761, 5 2005. ISSN 0018926X. doi: 10.1109/TAP.2005.846453.

[33] J.d. Wade and R.h. Macphie. Scattering at Circular-to-Rectangular Waveguide Junctions. *IEEE Transactions on Microwave Theory and Techniques*, 34(11):1085–1091, 1986. doi: 10.1109/tmtt.1986.1133503.

[34] Jack Welch, Don Backer, Leo Blitz, Douglas Bock, Geoffrey C Bower, Calvin Cheng, Steve Croft, Matt Dexter, Greg Engargiola, Ed Fields, James Forster, Colby Gutierrez-Kraybill, Carl Heiles, Tamara Helfer, Susanne Jorgensen, Garrett Keating, John Lugten, Dave Macmahon, Oren Milgrome, Douglas Thornton, Lynn Urry, Joeri Van Leeuwen, Dan Werthimer, Peter H Williams, Melvin Wright, Jill Tarter, Robert Ackermann, Shannon Atkinson, Peter Backus, William Barott, Tucker Bradford, Michael Davis, Dave Deboer, John Dreher, Gerry Harp, Jane Jordan, Tom Kilsdonk, Tom Pierson, Karen Randall, John Ross, Seth Shostak, Matt Fleming, Chris Cork, Artyom Vitouchkine, Niklas Wadefalk, and Sander Weinreb. The Allen Telescope Array: The First Widefield, Panchromatic, Snapshot Radio Camera for Radio Astronomy and SETI. Technical report.

[35] Jian Yang, Miroslav Pantaleev, Per Simon Kildal, and Leif Helldner. Design of compact dual-polarized 1.2-10 GHz eleven feed for decade bandwidth radio telescopes. *IEEE Transactions on Antennas and Propagation*, 60(5):2210–2218, 2012. ISSN 0018926X. doi: 10.1109/TAP.2012.2189732.

[36] Jian Yang, Jonas Flygare, Miroslav Pantaleev, and Bhushan Billade. Development of quadruple-ridge flared horn with spline-defined profile for band B of the Wide Band Single Pixel Feed (WBSPF) advanced instrumentation programme for SKA. In *2016 IEEE Antennas and Propagation Society International Symposium, APSURSI 2016 - Proceedings*, pages 1345–1346. Institute of Electrical and Electronics Engineers Inc., 10 2016. ISBN 9781509028863. doi: 10.1109/APS.2016.7696380.